creative commons
COMMONS DEED

저작자표시-비영리-변경금지 2.0 대한민국

이용자는 아래의 조건을 따르는 경우에 한하여 자유롭게

- 이 저작물을 복제, 배포, 전송, 전시, 공연 및 방송할 수 있습니다.

다음과 같은 조건을 따라야 합니다:

저작자표시. 귀하는 원저작자를 표시하여야 합니다.

비영리. 귀하는 이 저작물을 영리 목적으로 이용할 수 없습니다.

변경금지. 귀하는 이 저작물을 개작, 변형 또는 가공할 수 없습니다.

- 귀하는, 이 저작물의 재이용이나 배포의 경우, 이 저작물에 적용된 이용허락조건을 명확하게 나타내어야 합니다.
- 저작권자로부터 별도의 허가를 받으면 이러한 조건들은 적용되지 않습니다.

저작권법에 따른 이용자의 권리는 위의 내용에 의하여 영향을 받지 않습니다.

이것은 이용허락규약(Legal Code)을 이해하기 쉽게 요약한 것입니다.

Disclaimer

dCollection

Ph. D DISSERTATION

Development of novel surface plasmon-based metal coated fiber-facets and their applications

독창적 플라즈몬 기반 금속 코팅 광섬유 단면의 개발과 그 응용

By

HYUNTAI KIM

AUGUST 2016

DEPARTMENT OF ELECTRICAL AND

COMPUTER ENGINEERING

COLLEGE OF ENGINEERING

SEOUL NATIONAL UNIVERSITY

Development of novel surface plasmon-based metal coated fiber-facets and their applications

독창적 플라즈몬 기반 금속 코팅 광섬유 단면의 개발과 그 응용

지도 교수 정 윤 찬

이 논문을 공학박사 학위논문으로 제출함
2016 년 8월

서울대학교 대학원
전기컴퓨터 공학부
김 현 태

김현태의 공학박사 학위논문을 인준함
2016 년 8월

위 원 장 _____ (인)

부위원장 _____ (인)

위 원 _____ (인)

위 원 _____ (인)

위 원 _____ (인)

Abstract

Development of novel surface plasmon-based metal coated fiber-facets and their applications

HYUNTAI KIM
DEPARTMENT OF ELECTRICAL AND
COMPUTER ENGINEERING
COLLEGE OF ENGINEERING
SEOUL NATIONAL UNIVERSITY

In this dissertation, novel surface plasmon (SP)-based, metal coated fiber-facet structures are proposed and demonstrated. Various novel effects caused by SP are achieved by these fiber-optic-plasmonic hybridized schemes in a reliable and compact fiber-optics based platform.

The first part of the dissertation introduces metallic nano-slit based fiber-facet structures. First, a novel trench-assisted circular metal nano-slit (TA-CMNS) structure implementable on a fiber platform for the generation of a low-noise cylindrical surface plasmon (CSP) hotspot is introduced. The nearby trenches are designed based on the multi-pole cancellation method in order to separate a converging CSP signal from co-propagating NCDL at the hotspot location. The plasmonic and optical characteristics of the structure are verified through full-vectorial numerical analyses. The

optimized TA-CMNS could generate low-noise plasmonic hotspots with substantial high performance characteristics.

Then, wavelength-dependent characteristics via nano-slit structures are discussed. A fiber-optical-plasmonic hybrid, metal coated fiber with a grating-assisted nano-slit (MCF-GANS) structure for wavelength dependent, off-axis directional beaming (WODB) in a simple and compact format is proposed and demonstrated. The device is designed based on the results of numerical analysis, and it is experimentally demonstrated. In addition, the fiberized plasmonic Fresnel zone plate (FPFZP) is proposed. The proposed FPFZP can efficiently generate a radially polarized focused light (RPFL) on the free space, where the focal length is tunable by controlling the wavelength. The focal length shift due to the wavelength of the FPFZP model is analyzed via numerical calculations. In addition, the trapping characteristics of the FPFZP are analyzed. The FPFZP structure is also fabricated and its characteristics are demonstrated. Good agreement between experimental and numerical results is obtained.

In the second part of the dissertation, a novel fiber mode to SP mode coupling configuration - angled fiber-facet coupling method - is presented and its applications are also introduced. The novel coupling configuration enables alignment-free, high-efficiency, unidirectional propagation, and small spot SP generation. The metal coated, angled fiber-facet (MCAFF) structure is verified by means of numerical simulations and experiments.

Two applications based on MCAFF are introduced. One is an

improved version of MCF-GANS, in which an MCAFF base is used to substitute for the nano-slit base. This change will increase the coupling efficiency by eliminating the anti-propagating SP. The grating structure on the top of the MCAFF decouples the SP mode into a free-space, optical radiation mode in different directions, depending on the wavelength of the input optical radiation. Therefore, a novel SP-based WODB functionality is realized in a simple, compact, and all-fiberized format. The other is a versatile fiber-based SP transmitter-receiver. The device consists of two MCAFF schemes. Numerical simulations have verified that the proposed device is capable of sensing various plasmonic effects induced at the metal-dielectric interface.

A structured metal coated fiber-facet scheme will be very useful for various plasmonic applications, which could be achieved in a compact, flexible, and cost-effective optical fiber-based format. In particular, the proposed MCAFF scheme (fiber-to-SP coupling scheme) has great potential to be an excellent, alternative SP generation method that can provide high efficiency, unidirectionality, and full compatibility with fiber-based optical sources. It is expected that the dissertation will broaden the fiber-optic and plasmonic research fields, which are invariably seeking novel opportunities for combining the extraordinary characteristics of plasmonics and the outstanding flexibility of fiber-optics.

Keywords : Fiber-optics, plasmonics, fiber-facet, surface plasmon coupling, nano-photonics, prism coupling
Student Number : 2011-30226

Contents

List of Figures

List of Tables

Chapter 1

Introduction

1.1 Overview on fiber-optics

Optical fiber is a flexible, transparent cylindrical dielectric string-like waveguide, which is capable to transmit light through itself. The first idea to guide light in dielectrics was demonstrated in 1870s. It was demonstrated that light followed the path of water jet flowing out of a container. During the 1950s, a device named fiberscope was developed, which transmits image following the first practical all-glass fiber. However, these glass fibers showed severe loss. To overcome the propagation loss, attempt to surround the glass with lower index cladding was designed, which resemble to the shape of latest optical fiber [1]. Since then, fiber-optics has been extensively studied and applied in numerous fields such as sensing, spectroscopy, imaging, nonlinear optics, and so on [2-4].

The development of the rare earth doped fiber boosted the fiber-optics. The usage of rare earth materials – such as erbium, ytterbium, and thulium – as a dopant inside the fiber, fiber amplifiers and fiber lasers were developed based on the light amplification by stimulated emission of radiation (LASER) theory [5]. Optical fiber amplifier based on erbium-doped fiber, which amplifies telecommunication

signal, was demonstrated in 1986 [6]. An optical fiber amplifier is a device which amplifies fiber-optic modes directly, without the need of converting it to an electrical signal. Nowadays this is widely known as erbium doped fiber amplifier (EDFA). Since then, fiber-optic communication systems have been deployed and have revolutionized the network systems [7].

The fiber-lasers have been extensively studied and applied in numerous fields these days due to its various advantages such as flexibility, reliability, high power, pulse operation, cost-efficiency and compactness. In the military field, the high-power fiber laser, which is capable to reach kW regime [8], is weaponized. Also, pulsed lasers are utilized in various medical applications [9]. In addition, fiber laser based machining and molding technology have emerged in industrial fields [10].

1.1.1 Principles of optical fiber

An optical fiber is a dielectric waveguide that transmits light along its axis. A typical optical fiber is consist of core, cladding, and jacket. The material for fiber core and cladding is generally fused silica. A structure of typical fiber is shown in Fig. 1.1.1.

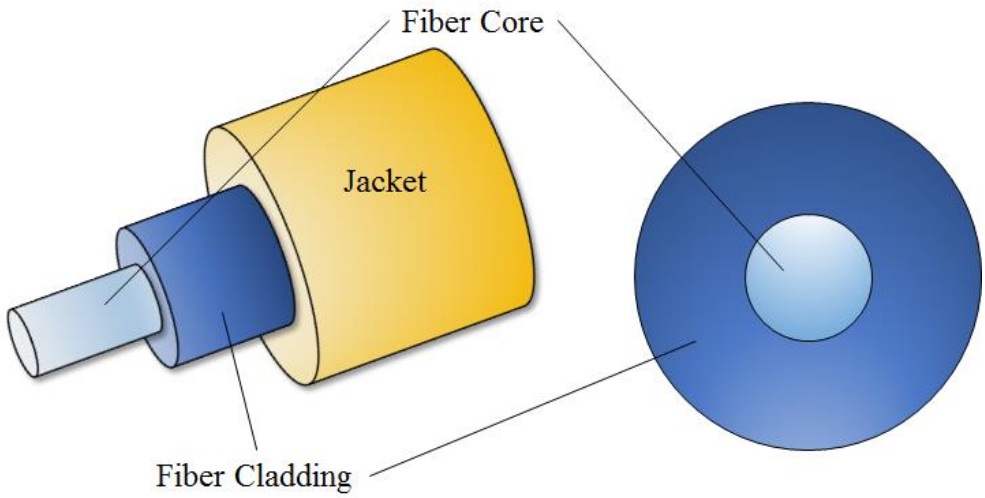

Fig. 1.1.1. Structure of optical fiber.

Various types of fibers exists for their purpose such as follows: Graded index fibers are developed to compensate the difference of the propagation constant on different modes. Multi-core fibers are used transmit several signals. Double-cladded fiber are frequently used in fiber-laser systems to absorb large pump power in the inner cladding, which works as another core. Photonic crystal fiber based on the properties of photonic crystal are used for nonlinear effects. Such fibers are depicted in Fig. 1.1.2.

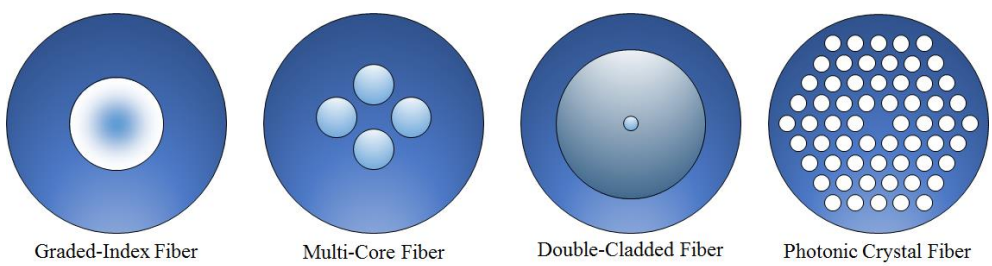

Fig. 1.1.2. Various types of optical fiber.

Optical fiber guide light without loss by the phenomenon of total internal reflection. By the total internal reflection between light can

propagate inside the core without leaking to the cladding. To satisfy the total internal reflection condition, the refractive index of the inner side, i.e. fiber core, must be higher than that of the outer side, the cladding. Also, the incident angle of guided light must be larger than a certain level called critical angle. Thus, to couple light into a fiber, there is limitation on angle of acceptance. To indicate the angle of acceptance, a parameter named numerical aperture (NA) is widely used. NA is defined as a sine of the maximum angle of an incident ray, expressed as follow:

$$NA = \sqrt{n_{core}^{\ 2} - n_{clad}^{\ 2}}, \qquad (1.1.1)$$

where n_{core} and n_{clad} is the refractive index of the core and cladding,

1.1.2 Mode characteristics of optical fiber

An optical fiber contains an eigen mode. This optical path is called fiber mode. Each modes have different field distribution, propagation constant, polarization, etc. The mode of the optical fiber can be solved by Maxwell's equation or using numerical analysis. In general, the number of mode is increased when the core is larger, the NA is higher, and the wavelength is shorter. In conventional step-index fiber, a parameter called $V\text{-}number$ indicates the number of existing modes. The normalized frequency $V\text{-}number$ is defined as follow:

$$V = \frac{2\pi a}{\lambda} NA = \frac{2\pi a}{\lambda} \sqrt{n_{core}^{\ 2} - n_{clad}^{\ 2}}, \qquad (1.1.2)$$

where λ is the wavelength of the light in free space, a is the radius of fiber core, and NA is the numerical aperture. For $V\text{-}numbers$

below 2.405, a fiber has only one mode, the fundamental mode. From 2.405 to 3.832, fiber supports also the cylindrical mode. Note that these cutoff values are the zeros of the Bessel function *J*. When the *V−number* increases, the number of existing mode also increases, approximately following the equation:

$$M \approx \frac{V^2}{2} \qquad (1.1.3)$$

The fundamental mode, also known as HE_{11} mode exists on every fiber. Its field distribution is similar to a Gaussian profile, and the electric field is linearly polarized. The next modes are cylindrical vector modes, and it has degenerate modes also known as TE_{01}, TM_{01}, HE_{21} mode. These modes are capable of maintaining their orbital angular momenta while propagating in the fiber. Each mode profiles and the polarization is shown in Fig. 1.1.3.

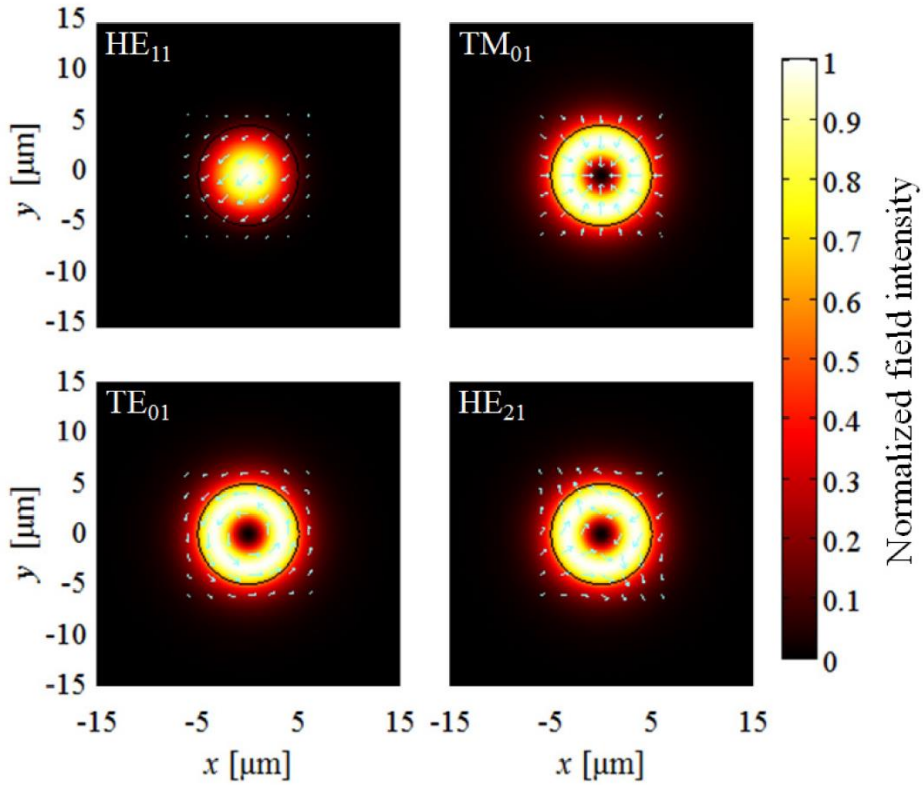

Fig. 1.1.3. The field intensity distributions of (a) the fundamental mode and (b)－(d) the cylindrical vector modes of a typical step indexed core fiber. The arrowed lines denote the directions of the electric field vectors.

1.2 Overview on plasmonics

Surface plasmon (SP) is a collective oscillation of electron propagating at the interface between metal and dielectric [11]. The existence of this phenomenon was early predicted on 1957, based on Maxwell equations [12]. After decades, SP has been discovered experimentally by extraordinary transmission phenomenon [13], which could not be explained in the classical electromagnetic theories.

After then, SP was highlighted to the researchers due to the fact that it gives not only a breakthrough to overcome the diffraction limits on conventional optics [14], but also other fascinating physical characteristics.

Thanks to the recent progress on nano-photonics, plasmonics has been extensively studied for decades. The plasmonics dedicated nano-scaled waveguide [15], SP resonance sensors for biomedical purpose [16, 17], next-generation optical data storage [18], photovoltaic devices such as plasmonic solar cells [19], and so on.

1.2.1 Principles of surface plasmon

In physics, plasmon can be interpreted as an oscillation of quantum particles. And SPs are collective oscillation of electrons which belongs to quantum particles. SPs can be classified in two types, one is propagating SP, and the other is localized SP (LSP). Propagating SPs, also known as SP polaritons (SPPs), are TM polarized electromagnetic wave bounded in the dielectric-metal surface, also shown in Fig. 1.2.1(a). And the LSP is the result of the SP confinement in a sub-wavelength structure [20]. The electric fields near the surface are greatly enhanced, such as shown in Fig. 1.2.1(b).

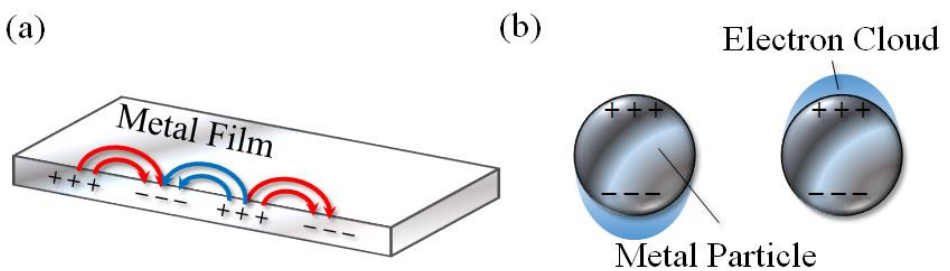

Fig. 1.2.1. SPs (a) at a flat gold-air interface (propagating SP) and (b) in a gold nanoparticle (LSP).

SP can be derived from Maxwell equation, and the wavenumber is derived as following equation [11]:

$$k_{SP} = k_0 \sqrt{\frac{\varepsilon_d \varepsilon_m}{\varepsilon_d + \varepsilon_m}}, \qquad (1.2.1)$$

where k_{SP} is the wavenumber of SP, k_0 is that of the free-space light, and ε_d and ε_m is the permittivity of the dielectric and metal, respectively.

1.2.2 Excitation of surface plasmon

In general, the wavenumber of the free-space light is smaller than that of the SP. Thus, additional phase-matching methods are required for SP generation.

Dedicated coupling methods have to be utilized to generate SPs because their wavenumbers are invariably larger than that of free-space light. Commonly used SP-coupling methods are nano-aperture schemes, prism coupling schemes, and grating-assisted schemes.

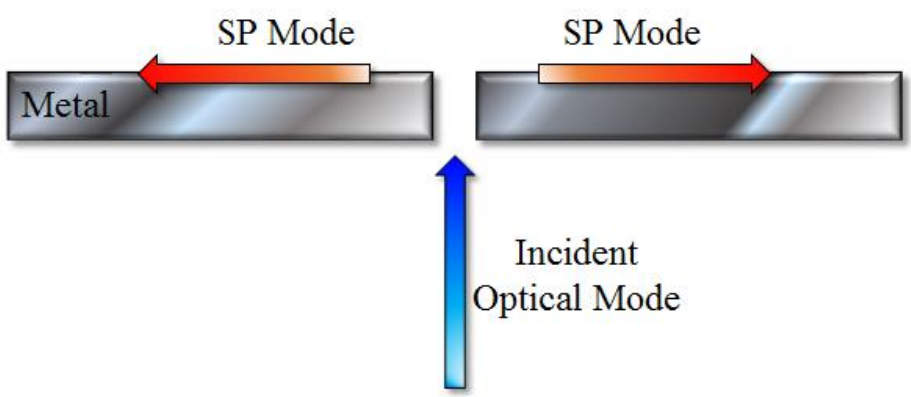

Fig. 1.2.2. Nano-slit SP coupling schematic.

Nano-slit structure is one of the common structure to couple free-space light to SP. The subwavelength structure assists high concentration of electromagnetic waves and from the intense hotspot, SPs are generated of the assist of one the nano-slit. The nano-slit structure is widely used due to its convenience on fabrication, however the structure also generates unwanted non-confined diffraction light (NCDL). The nano-slit coupling schematic is shown in Fig. 1.2.2.

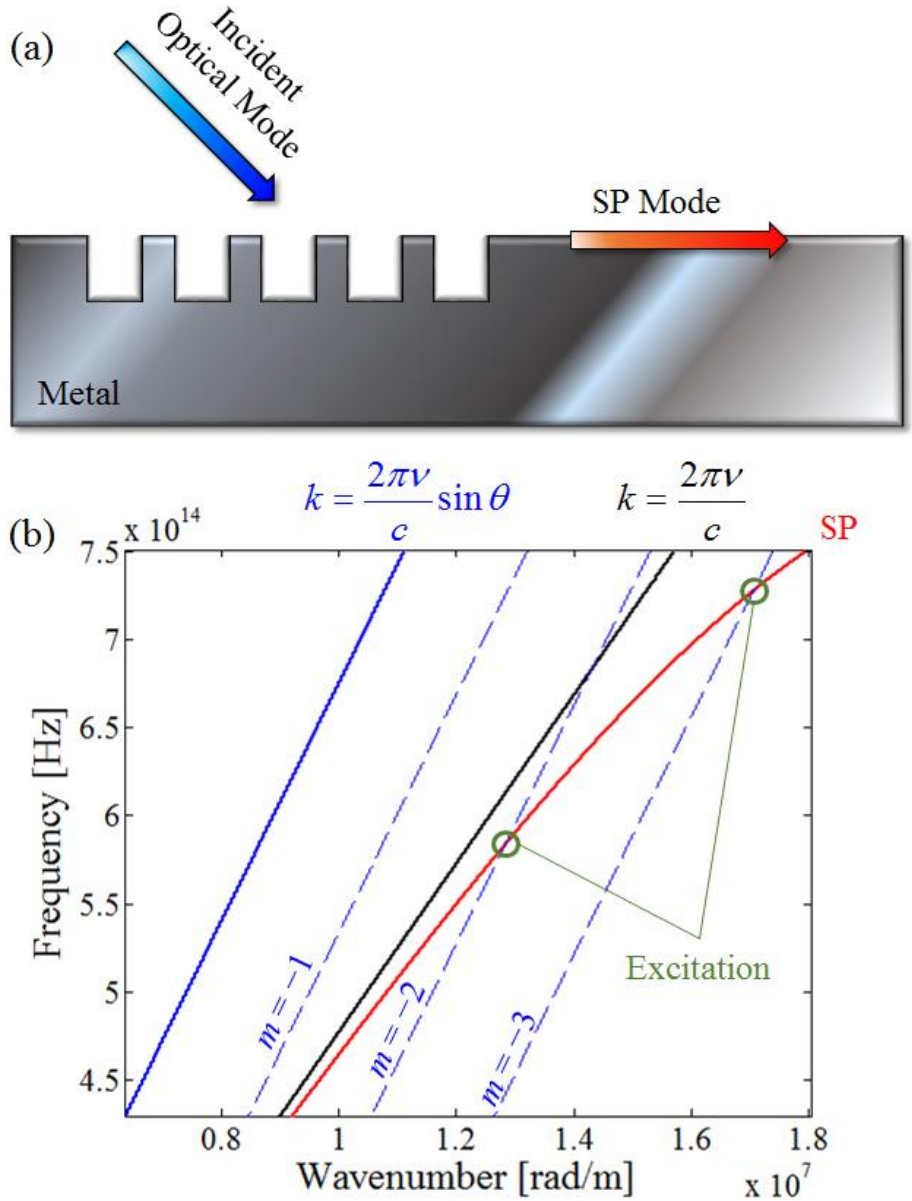

Fig. 1.2.3. (a) Schematic of grating coupling method. (b) Phase-matching condition of the grating coupling.

Periodic structures, such as nano-scaled gratings, could provide additional wavenumbers from the special structure. These additional momentums can provide SP coupling. Figure 1.2.3(a) shows the schematic of the grating coupling. The phase-matching condition for

the SP excitation is shown in following equation.

$$k_{SP} = k_0 \sin\theta \pm m\frac{2\pi}{\Lambda} \qquad (1.2.2)$$

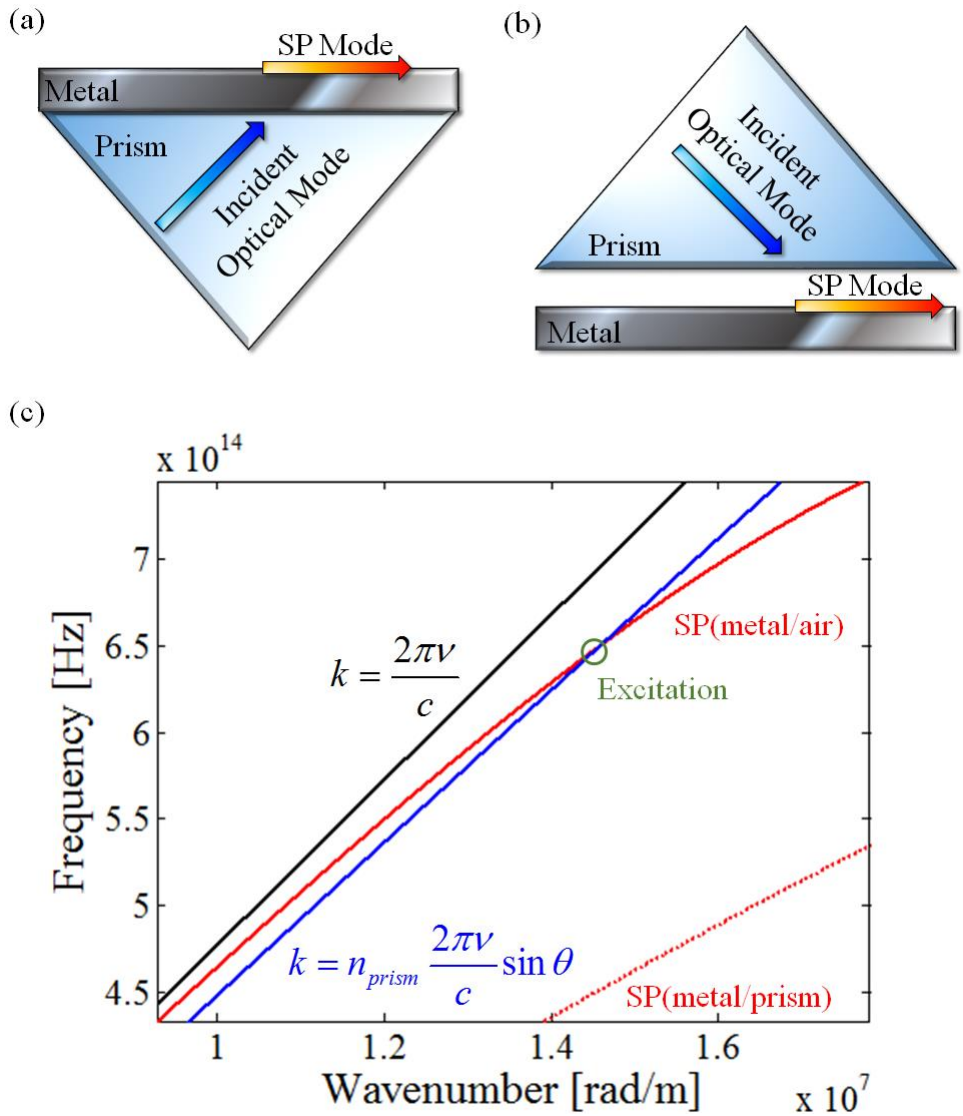

Fig. 1.2.4. Schematic of prism coupling method – (a) Kretschmann's configuration and (b) Otto's configuration. (c) Phase-matching condition of the prism coupling.

The prism coupling technique is one of the most frequently used methods to generate SPs, which is normally based on an oblique

incidence towards a dielectric-metal interface where the real part of the dielectric material should be higher than that of the metal. The prism coupling has two configuration, one is Kretschmann's configuration [21] and the other is Otto's configuration [22]. The left figure indicates the Kretschmann's configuration, where a thin metal layer is attached in the prism surface. Figure 1.2.4(b) shows the Otto's configuration, where the prism and the metal layer is separated. The phase-matching condition for the SP excitation is shown in Fig. 1.2.4(c) and the following equation.

$$k_{SP} = n_{prism} k_0 \sin\theta \qquad (1.2.2)$$

Note that the grating structure and the prism can also extract the SP to free-space light. Following the time reversal symmetry, the SP can also decoupled as the same procedure.

1.3 Motivation of this dissertation

As described in the previous section, fiber-optics and plasmonics both have fascinating characteristic. Fiber based platform provides flexible, compact, and cost-efficient platform. In addition, allows full-accessibility on fiber based sources, which are capable to control polarization, power, pulse, and wavelength. To apply state-of-the-art plasmonic techniques on base of versatile fiber-optic infrastructures, a metal coated fiber-facet structure is suggested. One may reduce numbers of additional optical device by applying metal coated fiber-facets, such as shown in Fig. 1.3.1.

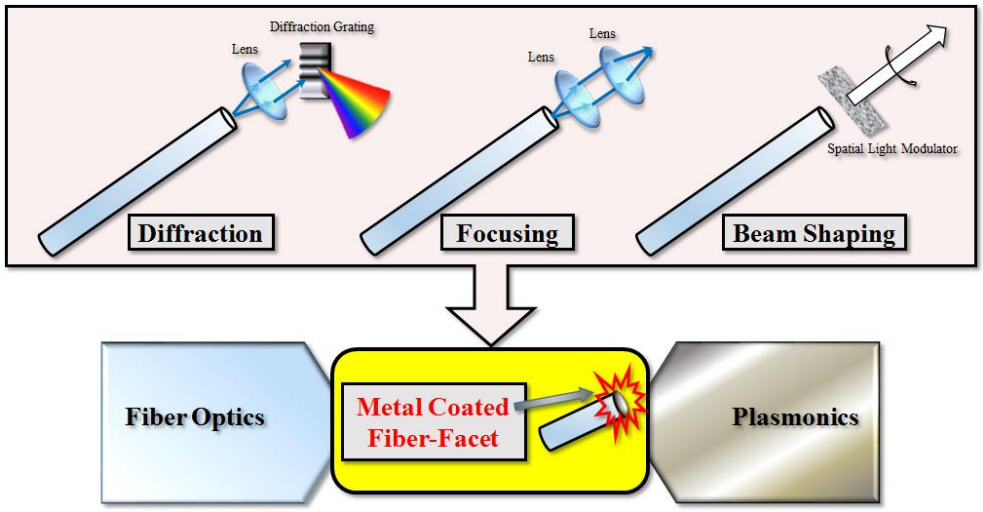

Fig. 1.3.1. Diagram of the usage of metal coated fiber-facet structure.

In fact, several metal coated fiber-facet structures were studied [23]. Surface-enhanced Raman spectroscopy (SERS) based on structured metallic fiber-facet were achieved [24-27]. Also, cone shaped fiber tip coated with metal is used for near field optical microscope (NSOM) [28, 29]. In addition, another application is beam shaping. By applying nano-slit apertures and patterning the surface, one can control the beam shape [30-32]. However, utilizing the wavelength-tunable characteristics of fiber sources via the metal coated fiber-facet were hardly studied. In addition, generating optical hotspots were also scarcely studied.

One challenging issue of the metal coated fiber-facet structure is the SP generation method. Most of the metal coated fiber-facet generates SPs by nano-slit coupling method. Nano-slit coupling method suffers from low efficiency due to the NCDL, and SPs propagating to the opposite side. Therefore, an alternative fiber to SP coupling method is required.

The motivation of this dissertation is to propose novel metal coated fiber-facet structures. Especially, based on wavelength tunability of the fiberized source, various plasmonic wavelength-dependent characteristics will be introduced. Also, generation of optical hotspot will be another issue. In addition, a new alignment free, high efficiency fiber-optical mode to SP coupling method and its applications will be presented.

1.4 Scope and organization

The dissertation is focused on two issues. First is nano-slit based applications, and the other is introduction and application of angled fiber-facet configuration.

In Chapter 2, three nano-slit based structures are proposed. First is trench assisted circular nano-slit, which is to generate noiseless plasmonic hotspot. Chapter 2.1.1 present brief theoretical descriptions on the proposed multi-pole cancellation method applicable to CMNSs and discuss how the quasi-pole oscillations via trench structures suppress NCDL noises. In Chapter 2.1.2, two types of trench structures utilizing the proposed method are designed, first is a rectangular-trench (RT) structure and the other is an asymmetric-parabolic-trench (APT) structure. While the former is considered for the sake of the simplicity of fabrication, the latter presents the further optimized cancelling performance of the quasi-pole oscillations. In Chapter 2.1.3, numerically analyze of the optical and plasmonic characteristics of the proposed structures is performed, and the results are compared with that of a conventional

CMNS having no trench structure. It will show that the proposed structures are capable of generating CSP hotspots with much enhanced SNRs. In addition, the tolerance of the device fabrication is discussed, considering the currently available nano-scale processing technology.

Chapter 2.2 shows the second structure, a grating assisted metallic nano-slit structure which is for wavelength-dependent beaming. Chapter 2.2.1 analyze the directional functionality of the proposed metal coated fiber-facet with grating assisted nano-slit (MCF-GANS) with both numerical and analytic calculations. Chapter 2.2.2 discuss how was the device realized and finally demonstrate its unique WODB performance through the device in-house fabricated via a focused ion beam (FIB) method [33, 34] on a metal coated single-mode fiber.

In Chapter 2.3, the third structure, a metallic Fresnel zone plate, is discussed. The structure is proposed to generate radially focus light with a tunable focal length.

In Chapter 3, first the novel fiber-optic-plasmonic coupling configuration - angled fiber-facet coupling is proposed, which is motivated from the Kretschmann' s configuration. Numerical and experimental demonstration of the configuration will be shown, and two applications will be introduced. One is grating assisted angled fiber-facet structure, which is improved from the grating assisted nano-slit structure shown in Chapter 2.2. Chapter 3.2 investigates and discusses, through rigorous numerical simulations, the WODB functionality of the proposed scheme when a periodically corrugated

structure is implemented on the top of the metal layer.

In Chapter 3.3, V-shaped configuration is introduced which is capable for sensing and for fiber-optic-plasmonic-fiber-optic two steps of convert. The property of the model is shown through numerical simulations.

Chapter 2

Metallic nano-slit based fiber-facet structures

One of the common method to excite SP is nano-slit coupling method. When the light pass a sub-wavelength metallic nano-slit, extraordinary transmission occurs and portion of the optical mode couples into SP mode. This method is relatively simple to fabricate, and widely used. In this Chapter, applications based on nano-slit structures are discussed.

2.1 Trench-assisted circular metallic nano-slit for low-noise plasmonic hotspot generation

In particular, SPs can be focused onto a sub-wavelength hotspot, which can overcome the diffraction limit of light [11, 14, 20, 35, 36]. Plasmonic focusing is useful for a variety of novel applications, such as lithography [37], imaging [38], high harmonic generation [39], sensing [40], etc. To date, a number of structural configurations have been suggested for plasmonic focusing, exploiting the extraordinary characteristics of the focused SPs, which include nanoparticles [41], circular nano-slits [42-46], bowtie structures [47], metal tips [48, 49], etc. Among them circular metallic nano-slit (CMNS) structures patterned on a thin metal film are of great interest because of their high capability of generating focused cylindrical SPs (CSPs), i.e.,

plasmonic hotspots, via relatively simple fabrication methods. In recent years, a variety of studies on the CMNSs have been investigated in the direction of intensifying the hotspot, utilizing various structures as well as differentiating the polarization state of incident light. For example, Kim et al. proposed a novel scheme utilizing a modified circular slit with linearly polarized light, which could significantly improve the CSP intensity and control the focal position [43]. Steele et al. experimentally demonstrated an efficient way to focus SPs via using a multi-ring structure [44]. Lerman et al. utilized radially polarized light as incident light to a CMNS, scaling up the energy of the hotspot, which could eventually lead to much higher efficiency than when linearly polarized light was used [46]. In addition, Chen et al. combined the previous two techniques, thereby applying radially polarized light to a multi-ring structure for further enhancements [45].

While such a variety of structures and schemes were extensively investigated for intensifying the plasmonic hotspots, the impact of the disturbance of non-confined diffracted light (NCDL) that normally accompanies CSPs has little been discussed to an extensive level [50, 51]. In fact, in most cases of CMNSs the disturbance of NCDL is hardly avoidable [52, 53], which inevitably results in a severe increment of background noise against the CSP signal [16, 17, 35, 54], thereby degrading the signal-to-noise ratio (SNR) of the CSP and enlarging its "effective" spot size. Suppressing the background noise of a plasmonic hotspot has little been studied although merely in a limited one-dimensional slit regime, the reduction of unwanted NCDL has been investigated by some of the

authors [36]. For this, trench-assisted (TA) slit structures were proposed by means of a multi-pole cancellation method (MPCM) [55]. In fact, a trench structure adjacent to the slit aperture forms a collective quasi-pole at the edge of the trench via SPs. The detoured plasmonic path due to the existence of the trench gives rise to a phase deviation to the quasi-pole oscillation against the primary NCDL that is directly generated from the slit aperture. Thus, a large fraction of the primary NCDL can be cancelled out by the secondary radiation from the quasi-pole oscillation if the phase of the secondary radiation is out of phase regarding that of the primary NCDL [36, 55-57].

Here, MPCM is extended to a full-vectorial model applicable to the design of CMNSs with enhanced noise-cancelling characteristics. Based on the method, novel trench-assisted circular metal nano-slit (TA-CMNS) structures implementable on a fiber platform is proposed. In particular, the fiber platform format allows for much simplified procedures to excite CSPs because a radially polarized optical mode can readily be excited or generated through an optical fiber [58]. Thus, this integrated scheme can offer a great merit of localizing and intensifying the resultant plasmonic hotspot in a compact and efficient form.

Hence, in the following this section firstly present brief theoretical descriptions on the proposed MPCM applicable to CMNSs and discuss how the quasi-pole oscillations via trench structures suppress NCDL noises. Secondly, two types of trench structure designs utilizing the proposed method, a rectangular-trench (RT) structure and an asymmetric-parabolic-trench (APT) structure, are proposed. While the former is considered for the sake of the

simplicity of fabrication, the latter presents the optimized cancelling performance of the quasi-pole oscillations. Then, numerically analyze of the optical and plasmonic characteristics of the proposed structures are performed, and the results are compared with that of a conventional CMNS having no trench structure, with which shows that the proposed structures are capable of generating CSP hotspots with much enhanced SNRs. Also, the tolerance of the device fabrication, considering the currently available nano-scale processing technology will be discussed.

2.1.1 Modelling

In general, a CMNS can produce a single plasmonic hotspot at its center via the inward-propagating CSP excited from a concentric annular slit structure formed on the metal surface. Different from straight, one-dimensional nano-slits, the CSP signal formed at the center of the CMNS can be much intensified because of the focusing effect. Furthermore, its efficiency can be maximized if radially polarized light is used as an excitation beam [45, 46]. Here, one can think of using an optical fiber as a device platform for a CMNS because radially polarized optical mode (e.g., TM_{01} mode) can readily be excited or generated through its core [58]. This is of great interest from a viewpoint of practicality because the plasmonic function can be realized in an all-fiber format, which will allow for great flexibility and simplicity compared to other conventional bulk-type CMNSs.

Thus, a full-vectorial model on a CMNS patterned on an optical

fiber end will be first considered. The schematic of the proposed CMNS structure is shown in Fig. 2.1.1, including its cross-sectional view and the fiber-optical field intensity pattern across the diameter of the fiber. It is assume that the fiber is a standard step-index fiber (SIF), which has a core diameter of 8 μm, and a numerical aperture of 0.1. It is also assumed that the metal is gold, the material parameters of which, i.e., the refractive index and extinction coefficient, are given by n = 0.16918 and k = 3.8816, respectively [59]. The input wavelength of the light is set to λ = 700 nm. The width of the slit opening and the thickness of the metal coating are set to 87.5 nm and 500 nm, respectively, which are typical values for metallic nano-slits. The annular slit is assumed to be concentric with the fiber core. In particular, to maximize the light incidence on the CMNS, the inner and outer radii of the annular slit are scaled to their center line to match with the peak intensity location of the TM_{01} mode of the SIF, as depicted in Fig.2.1.1. In addition, it is worth noting that this metallic structure can readily be fabricated via the conventional e-beam [60] or FIB technology [33, 34].

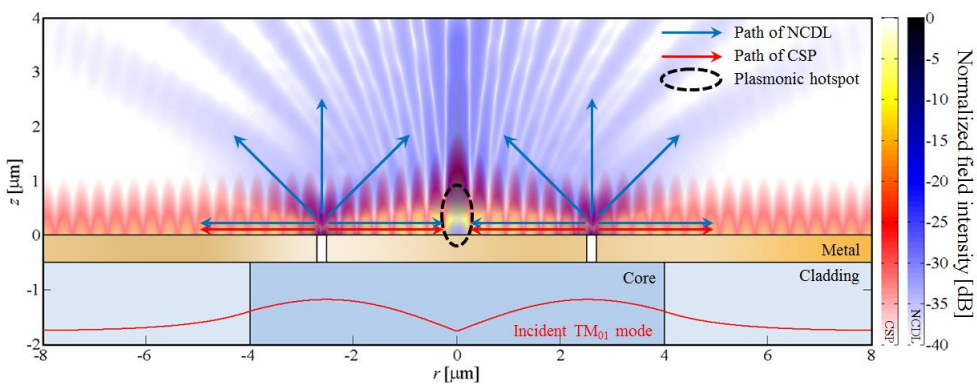

Fig. 2.1.1. Field intensity patterns (NCDL + CSP) obtained from a

simple CMNS when the TM_{01} mode of the SIF is incident.

First of all, a simple conventional CMNS structure having no trench structure is analyzed by utilizing the numerical model based on a full-vectorial finite element method (FEM: COMSOL Multiphysics®). It is worth noting that the separation of the CSP and NCDL fields from the total field is obtained by utilizing the overlap integral method based on the orthogonality principle of the mode field [61]. The CSP (depicted in graded red/yellow) and NCDL (depicted in graded blue) field intensity patterns are shown in Fig. 2.1.1. One can see that while a plasmonic hotspot is formed at the center of the metal surface, the NCDL propagating through free space is also focused at the same location because all the inward-going NCDL components are inherently in phase because of the circular symmetry of the CMNS. In particular, the horizontally propagating NCDL components are hardly distinguishable with the CSP hotspot signal, so that the SNR (defined as the ratio of the CSP intensity to the NCDL intensity) of the device is inevitably degraded [50, 55]. In particular, as shown graphically in Fig. 2.1.1, the CSP components are significantly overlapped with the NCDL components at the center of the metal surface. Here, the peak and mean SNRs are defined within the main lobe of the CSP hotspot because those parameters can primarily represent the performance of the device. The region of the main lobe is defined as the area where $\Delta z \leq 540$ nm and $\Delta r \leq 260$ nm, based on the attenuation length of the CSP in the z direction and the distance between two first zeroes in the r direction, respectively. In

the given condition, the calculated peak and mean SNRs are given by 22.74 and 14.70 dB, respectively, which are by no means ideal for many applications that invariably demand high SNRs, implying that there is room for significant enhancements.

2.1.2 Design principle

With the conventional CMNS as discussed in the previous section, CSP hotspots are inherently overlapped with the NCDL components to a significant level. In particular, the NCDL components propagating horizontally just above the metal surface severely result in degrading the SNR of the hotspot. Therefore, to improve the SNR, the impact of the primary NCDL, which is generated virtually from the slit center, should be suppressed. To achieve that, TA structures nearby the CMNS edges are used for cancelling out the unwanted primary NCDL component via exciting secondary NCDL from the TA structures as the following. The proposed TA structure and its operation principle are illustrated in Fig. 2.1.2. The main strategy of introducing the TA structure is to eliminate the significant portion of the primary NCDL (blue line) originated from the slit center using the secondary NCDL (red line) excited from the edge of the TA structure lying alongside the slit, which eventually leads to destructive interference with the primary NCDL [48, 51], as depicted in Fig. 2.1.2(b). It should be noted that the trench structure can be devised to have a sharp edge where charges are strongly induced due to its geometrical merit [41], so that it can be another "quasi-pole source" for generating the

secondary NCDL [62, 63].

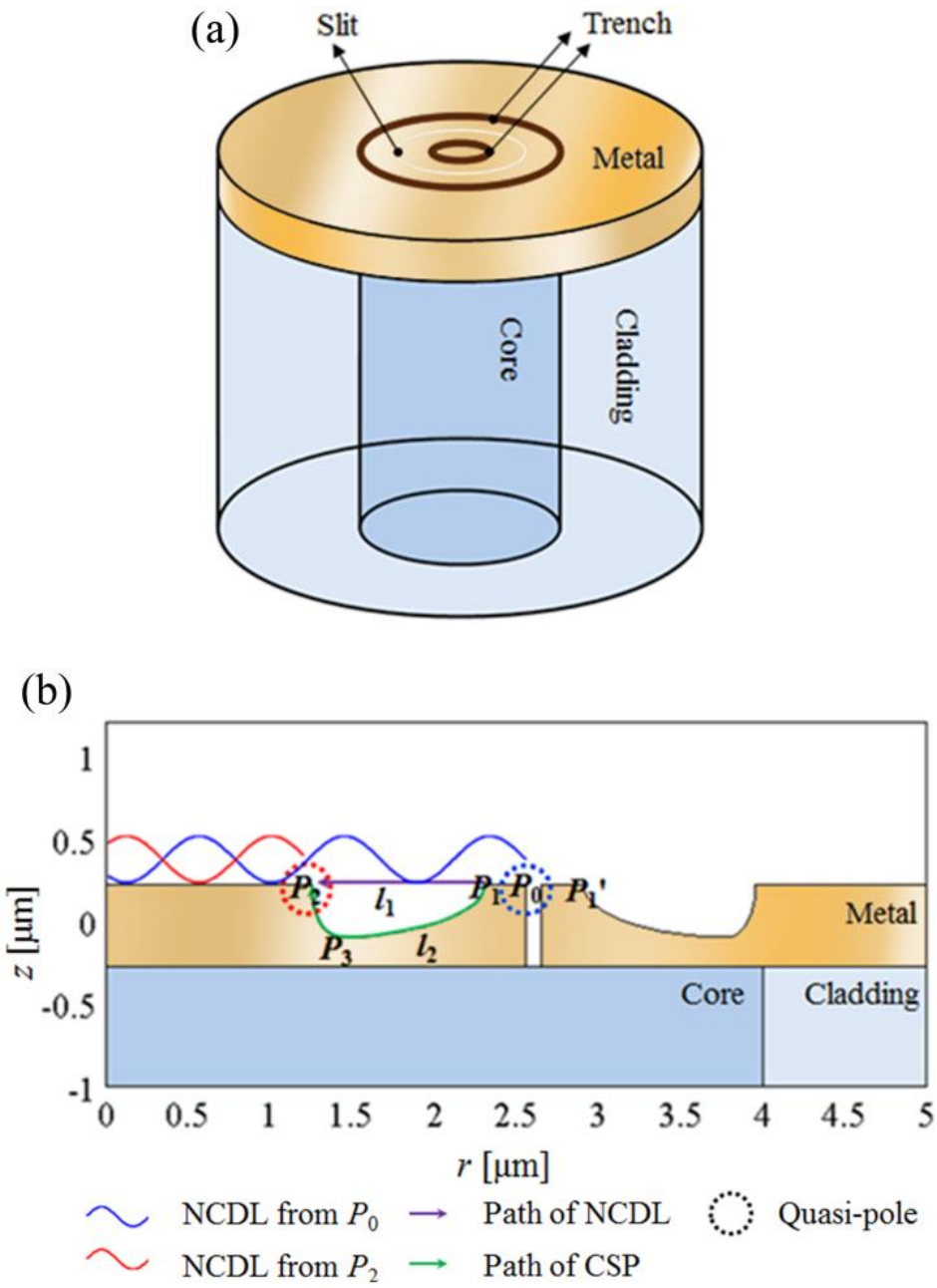

Fig. 2.1.2. (a) The proposed CMNS structure. (b) Cross-section of the TA-CMNS in the radial direction and its operation principle

In order to induce destructive interference between the primary and secondary NCDL components, it is not too difficult to understand

that the phase retardation between the primary NCDL along path l_1 and the CSP along path l_2 for the travel from P_0 to P_2 should be an odd integral multiple of π because the phase of the secondary NCDL is mainly determined by that of the CSP traveling from P_0 to P_2 along path l_2. The principle can be formulated by the following equation:

$$k_{CSP} l_2 - k l_1 = (2n-1)\pi , \qquad (2.1.1)$$

where k and k_{csp} denote the wavenumbers of the NCDL and the CSP, respectively, and n an integer number. In fact, the geometry, including the positions of P_1, P_2, and P_3 of the trench, determines the phase retardation between the CSP and the primary NCDL, which has yet to be determined through appropriate optimization. It is worth noting that the NCDL radiation from P_1 via the CSP is nearly in phase with the primary NCDL radiation from P_0 because, in general, the distance between P_0 and P_1 is substantially short, even with considering the material dispersion of the metal. Thus, it is too hard to expect a destructive interference effect from it. Subsequently, it is required to minimize the accumulation of charges at P_1, simply letting the most CSP pass to P_2, thereby maximizing the NCDL cancellation by means of the charges accumulated at P_2. Thus, the cavity structure formed between the two inner edges of the trenches (P_1 and P_1') should satisfy the resonance condition in order that the CSP transmission through the cavity is maximized. The resonance condition is fulfilled when the cavity satisfies the following relation [64]:

$$\mathrm{Re}(k_{CSP})d + \varphi_{Trench} = 2n\pi , \qquad (2.1.2)$$

where Re denotes the real part of the argument, d the distance between P_1 and P_1' , φ_{Trench} the phase shift caused by the reflection at the trench wall, and n an integer number.

2.1.3 Numerical results

In particular, two different types of trench structures are proposed: One is a rectangular trench (RT) and the other is an asymmetric parabolic trench (APT). While the former is the simplest form to realize the NCDL cancellation via the MPCM, it is found that an asymmetric apodization of the RT into an APT can eventually improve the overall SNR performance because too abrupt a transition of the geometry at P_1 can induce an unnecessarily large amount of charge accumulation there [65].

Now, the general procedure to determine the key parameters for the trench structure, i.e., P_1, P_2, and P_3 shown in Fig. 2.1.2(b) based on the MPCM will be discussed. First, the width of the trench is set to 1050 nm, considering the material loss as well as the fabrication resolution. Then, the geometry of the trench is determined such that the CSP and the primary NCDL at P_2 are fully out of phase, i.e., they satisfy the MPCM condition given in Eq. (2.1.1). In order to minimize the device dimension, the phase retardation between the CSP and the primary NCDL at P_2 is given by π. For an RT-CMNS, once the width of the trench ($P_2 - P_1$) is fixed, the depth of P_3 is the only parameter to be determined by the MPCM condition because of its symmetry. In contrast, for an APT-CMNS both the horizontal and vertical positions of P_3 (where the two asymmetric parabolas are joined)

should be determined at the same time by the MPCM condition while the other general procedures are similar to those for an RT-CMNS. Finally, the detailed geometry of the trench, including the absolute position of P_1, is fine-tuned in order that it eventually offers the highest SNR via Eq. (2.1.2).

The evolution of the mean SNR at the center of the CMNS is shown in Fig. 2.1.3(a) and 2.1.3(b) for the RT-CMNS and APT-CMNS regimes, respectively. It is worth noting that for the APT-CMNS, both the positions P_1 and P_3 are considered for optimization while for the RT-CMNS the position P_1 is only considered for optimization because of the symmetry. One can see that all the parameters can be fine-tuned through iterations to maximize the SNR at the hotspot location. The parameters of the optimized trenches are summarized in Table 2.1.1. Hereinafter, the optimized trenches will be used in analyzing their detailed characteristics.

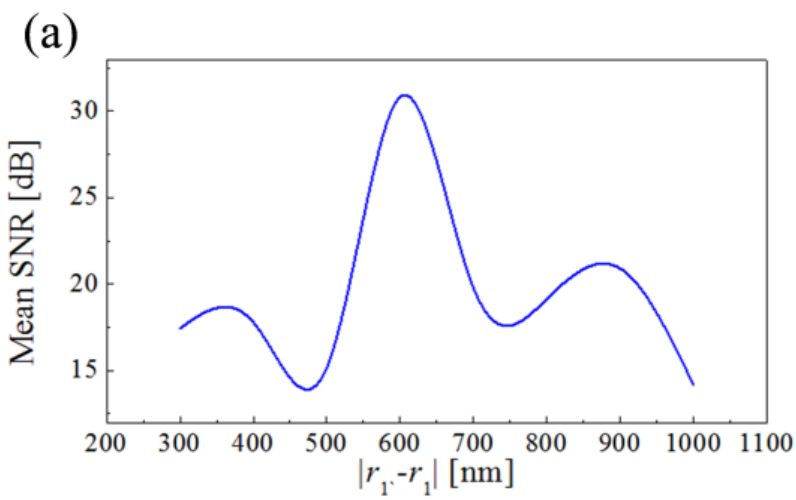

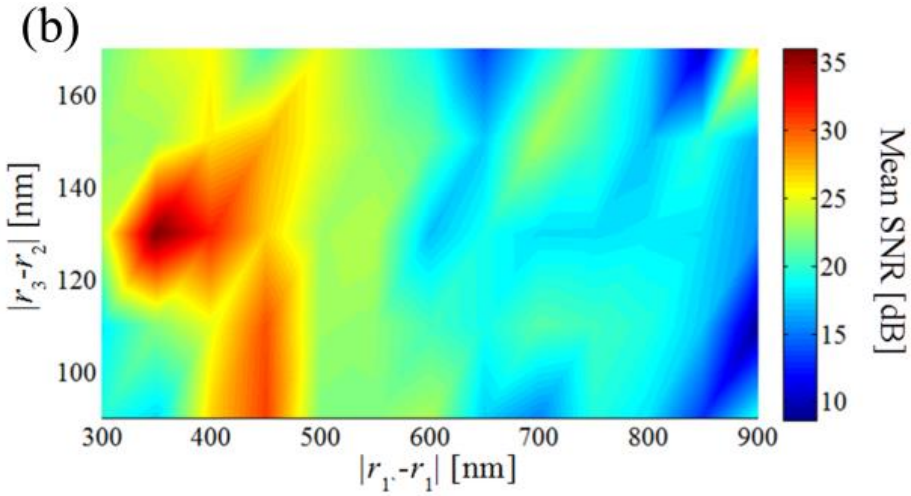

Fig. 2.1.3. (a) Mean SNR of an RT−CMNS structure with respect to the distance between trenches. (b) Mean SNR of an APT−CMNS with respect to the two−dimensional trench geometry.

Table 2.1.1. Design parameters of optimized trench structures

	RT−CMNS	APT−CMNS
Trench width ($\|r_1-r_2\|$)	1.05 μm	1.05 μm
Trench depth ($\|z_1-z_3\|$)	161 nm	296 nm
Distance between trenches ($\|r_1-r_1\|$)	600 nm	353 nm
Apex point ($\|r_1-r_3\|$)	−	920 nm

Figure 2.1.4 shows the field intensity distributions of the total field, the CSP component, and the NCDL component for both the optimized RT and APT structures. One can see a general trend that the CSP field forms a hotspot at the center of the device as shown in Fig. 2.1.4(b). However, in terms of the NCDL suppression characteristics, there are clear differences among the conventional CMNS and the TA−CMNSs. With the TA−CMNSs the NCDL noises

are substantially reduced down in the central region of the device. In particular, it is worth noting that the NCDL noise is nearly completely cancelled out at the center of the device for the APT-CMNS. It is also worth noting that although the maximum CSP intensity at the center is slightly reduced by 5.54 dB for TA-CMNSs in comparison with the conventional CMNS because of the additional loss incurred by the trench structure, the gain in terms of SNR is substantially higher than the intensity reduction level, which is to be quantified in the following through Fig. 2.1.5 and Table 2.1.1. Such a linear loss can readily be compensated by means of increasing the input power.

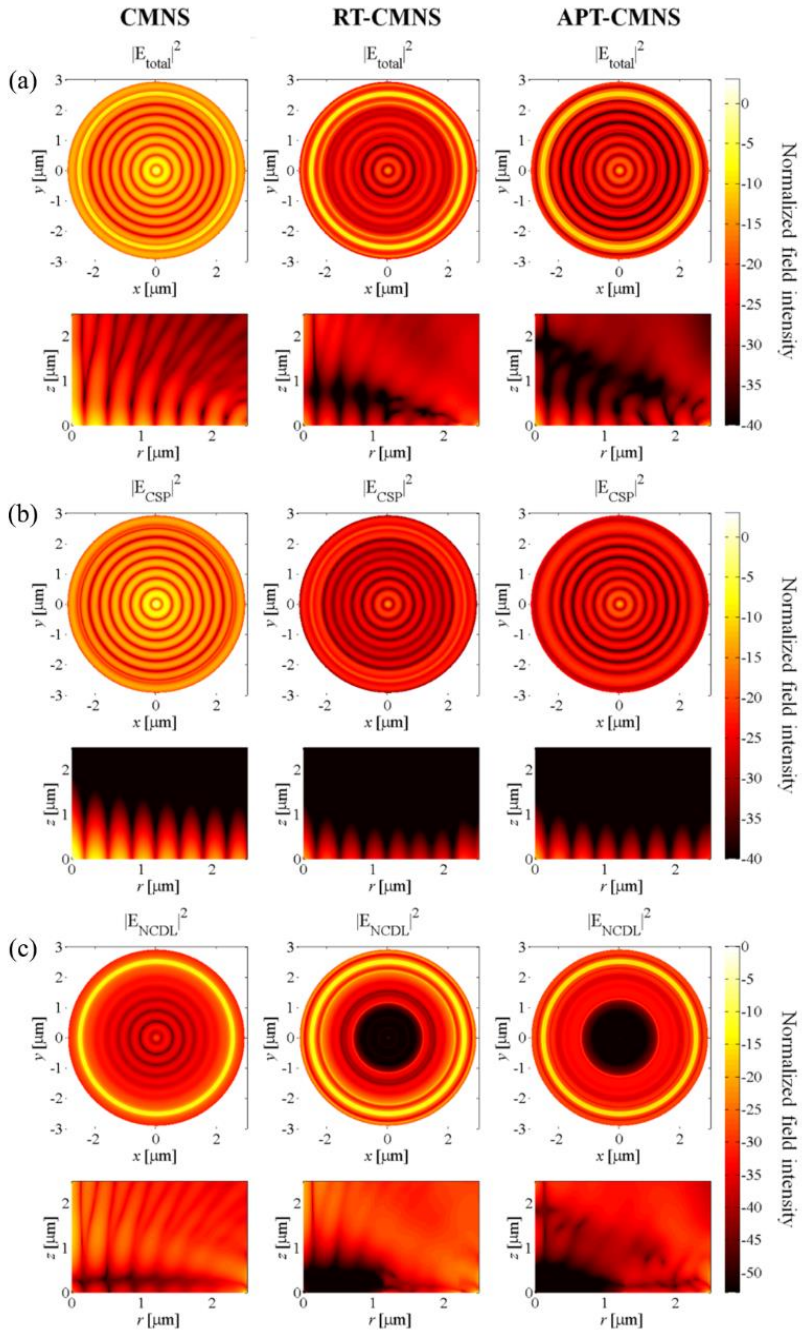

Fig. 2.1.4. Top and cross-sectional side views of (a) $|E_{total}|^2$, (b) $|E_{CSP}|^2$, and (c) $|E_{NCDL}|^2$ for each structure as specified.

Fig. 2.1.5 shows the spatial variations of the SNRs of the three CMNSs: Fig. 2.1.5(a) and 2.1.5(b) for the SNR variations in the

horizontal direction on the device surface and in the vertical direction at the center of the device, respectively, and Fig. 2.1.5(c) for the SNR distribution of each CMNS in the horizontal and vertical directions. It is worth noting that the SNR near the device surface in the central region is most important because the region is where the CSP is most intensive, thereby interacting with ambient material most effectively. In particular, if the APT-CMNS is employed instead of the conventional CMNS, one can expect 11.89 or 16.44 dB improvement in terms of the mean or peak SNR in the central part of the device, respectively, which is substantial. Considering the dimension of the hotspot formed at the center of the device, which is as small as 520 nm, the peak SNR of 50.71 dB highlights a dramatic performance of the APT-CMNS. Table 2.1.2 summarizes the SNR characteristics for the individual CMNSs.

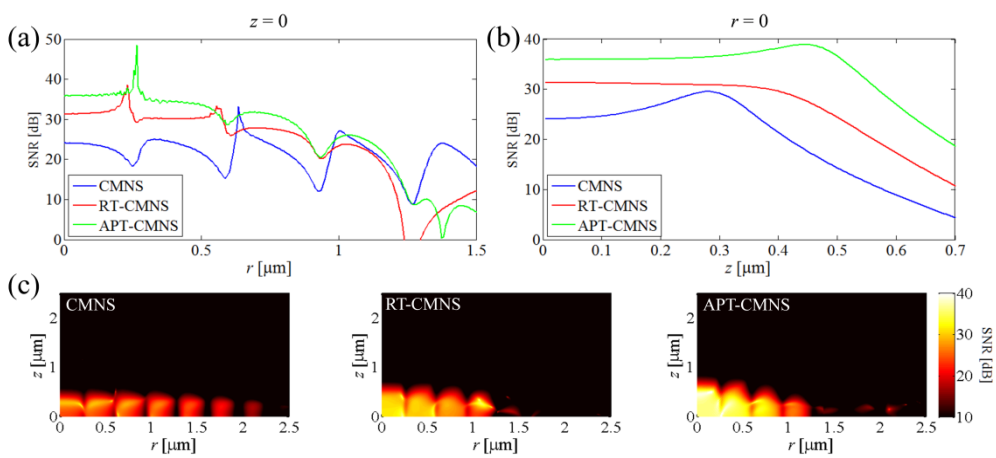

Fig. 2.1.5. SNR characteristics of the three CMNSs as specified: (a) SNR in the radial direction at z = 0 (on the metal surface), (b) SNR in the vertical direction at r = 0 (on the fiber axis). (c) SNR distribution in the r and z directions for each structure.

Table 2.1.2. SNR within the main lobe of the CSP hotspot

	CMNS	RT-CMNS	APT-CMNS
Peak SNR	34.27 dB	38.58 dB	50.71 dB
Mean SNR	24.14 dB	31.11 dB	36.03 dB

As numerically demonstrated above, one can substantially improve the overall SNR of a CMNS by fabricating a sophisticatedly designed trench structure nearby the slit opening. However, one may doubt whether the improvement can be maintained when the trench is not fabricated exactly to the design parameters. In fact, this can be an issue if the design parameters allow for too small tolerance. Thus, this matter will be further discussed. In general, the current e-beam lithography technology can routinely allow for a depth resolution of ~5 nm or better [60], so that one can consider that the tolerance of the depth control over the proposed TA-CMNSs is in line with that resolution. In addition, because the lateral dimension of the trench structure is much larger than its vertical dimension (depth), and also the lateral resolution of FIB milling process is substantially higher than its longitudinal resolution, one may reserve the discussion of the tolerance of the width control of the trench structure until the longitudinal tolerance issue is clarified.

Here, the change of the SNR caused by the inaccurate control of the depth of the trench is estimated. Considering the typical depth resolution of the FIB process, the depth of the trench is modified by ±5 nm, which is, in fact, the maximum value for the depth uncertainty [34]. Even with considering the tolerance range, the results proved that the TA structures still show improved SNR performance in

comparison with the conventional CMNS: The RT structure allows for at least 28.46 dB in terms of the mean SNR and 34.52 dB in terms of the peak SNR. The APT structure allows for at least 34.83 dB in terms of the mean SNR and 44.70 dB in terms of the peak SNR. These results further confirm that that the improved performance of the TA-CMNS is completely feasible with the current e-beam technology.

2.2 Metal coated fiber-facet with grating assisted nano-slit for wavelength-dependent off-axis beaming

Wavelength-dependent directional beaming (WDB) has been an important technology for various applications where the spatial separation of different spectral components are needed [66-72]. For WDB, diffraction gratings that are periodically varying optical structures are often utilized [3, 73-76]. This is true even for fiber-optic systems which also require accessing a wide range of spectral bands. For example, diffraction gratings have widely been used for pulse shaping, chirped pulse amplification, sensing, laser scanning, multi-wavelength generation, etc. However, the use of diffraction gratings in bulk types requires a number of free-space coupling devices as well as demanding relatively large space to implement them. Consequently, such systems can result in unnecessarily complex forms and high costs, which significantly undermine the intrinsic advantages of fiber-optic platforms, i.e., compactness, flexibility, and cost-effectiveness [2-4, 30, 77]. To overcome such drawbacks incurred by the use of conventional bulk-type diffraction gratings in fiber-optic systems, one can instead think of

implementing SP techniques.

SP can mediate between optical modes with a unique diffraction characteristic across a micro-nano-scaled, fine dielectric-metallic structure. For example, off-axis directional beaming from a sub-wavelength aperture has been achieved in a micro-scaled geometry utilizing periodic dielectric-metallic gratings implemented to a metal nano-slit structure. It is worth noting that this off-axis beaming exhibits highly wavelength-dependent characteristics [72, 78, 79]. Hence, SP-based, wavelength-dependent off-axis directional beaming (WODB) can be realized in fiber-optic platforms.

In this Chapter, a nano-machined metal coated fiber-facet as a simple and compact WODB device is propose and demonstrate. By coating the end facet of an optical fiber with silver and nano-machining it into a slit combined with asymmetric, periodic grooves that are in nano-scales, broadband, unidirectional WODB functionality in an all-fiberized format is obtained. It is worth noting that unlike a simple addition of an optical fiber-facet and a free-space diffraction grating, the WODB mechanism of this scheme is based on the excitation of SPs in the metal-dielectric interface. Note that differ to dielectric gratings [80], the metallic structure allows unidirectional diffraction, and also act as a polarizer.

2.2.1 Modeling and numerical analysis

Figure 2.2.1(a) emphasizes the significance of the WODB functionality achieved by the proposed fiber-optic-plasmonic hybrid structure, in which one can readily expect that the proposed scheme

is compact and align-free, resulting in an ultimately cost-effective solution for WODB based on a fiber-optic platform. In addition, the schematic of the proposed metal coated fiber-facet with groove-assisted nano-slit structure is shown in Fig. 2.2.1(b).

The schematic of the proposed MCF-GANS structure is shown in Fig. 2.2.1(a) and Fig. 2.2.1(b). In addition, Fig. 2.2.1(c) emphasize the significance of the WDB functionality achieved by the proposed fiber-optical-plasmonic hybrid structure, in which one can readily expect that the proposed scheme is compact and align-free, resulting in an ultimately cost-effective solution for WDB from an fiber-optic device.

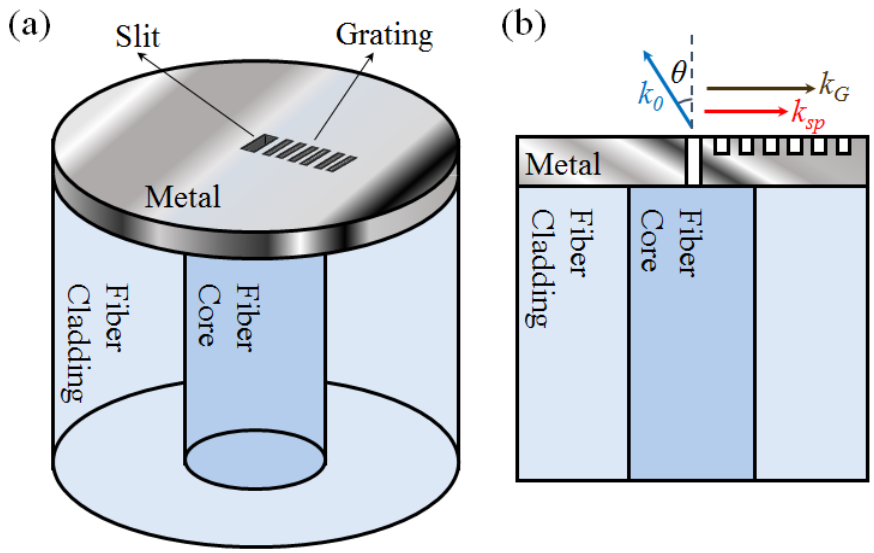

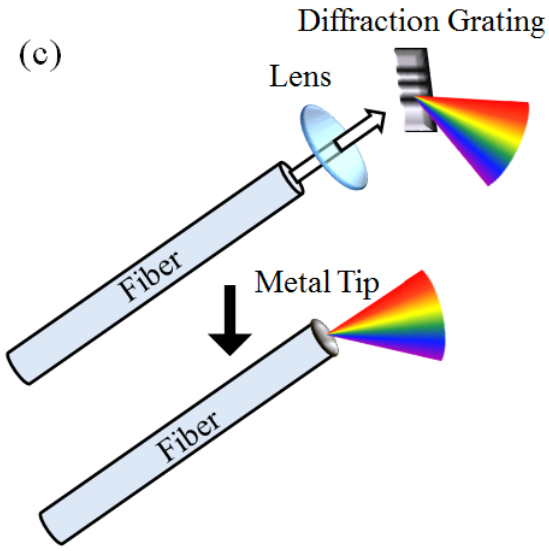

Fig. 2.2.1. (a) The cross-section and (b) the side view of the proposed fiber end. (c) Operation schematic of conventional WDB and proposed WDB.

The diffraction of light through the groove-assisted nano-slit via SP occurs as follows: Initially the fiber-optic mode passing through the metal nano-slit is converted into SP at the metal surface, and then the SP is coupled to free-space light under the influence of the corrugated grooves [81]. Compared to some other previous demonstration

In general, the wavelength dependent diffraction is determined by the phase-matching condition among the wavenumbers in the dielectric and metallic media and the grating vector, as given by the following equation [78]:

$$k_{SP} = k_0 \sqrt{\frac{\varepsilon_d \varepsilon_m}{\varepsilon_d + \varepsilon_m}}, \frac{\partial^2 \Omega}{\partial u^2} \quad k_G = \frac{2\pi}{\Lambda} \text{ , and } k_{SP} \pm m k_G = k_0 \sin\theta \quad (m=0,\ 1,\ 2,\ \ldots) \tag{2.2.1}$$

where k_0 the wavenumber in free space, k_{SP} the wavenumber of the SP mode, k_G the reciprocal lattice vector by the grating of the period of Λ, ε_d the permittivity of the dielectric, ε_m the permittivity of the metal, and θ the angle of the diffracted wave in free space. In fact, it is possible to determine a desired spectral range of WODB operation via adjusting the aforementioned variables. In particular, the grating period is tuned for the visible light operation, setting the grating period to 550 nm. Thus, exploiting the dispersion relation of the SP (k_{SP}) via the momentum matching condition with k_G, one can obtain a unique WODB performance that cannot be obtained from conventional free-space diffraction gratings.

To analyze the MCF-GANS structure, firstly numerical simulations based on the finite element method (FEM: COMSOL Multiphysics®) and analytical calculations are performed. Silver is selected as the coating material, which is good enough to demonstrate the target WODB performance and is also advantageous from the viewpoint of the cost-effectiveness. The material parameters of silver, i.e., its refractive index and extinction coefficient, are given in detail in Ref. [82]. The thickness of the metal coating is set to 200 nm. The rectangular MNS is formed in 10 μm by 300 nm. Next to the MNS, six periodic rectangular grooves are engraved in, having an opening of 10 μm by 275 nm with a depth of 50 nm. The spacing between them is 275 nm, leading to Λ = 550 nm. The fiber is assumed as a standard single-mode step-index fiber (SMF), which has a core diameter of 8.2 μm, and a numerical aperture of 0.14. These parameters were selected to operate in the visible light region.

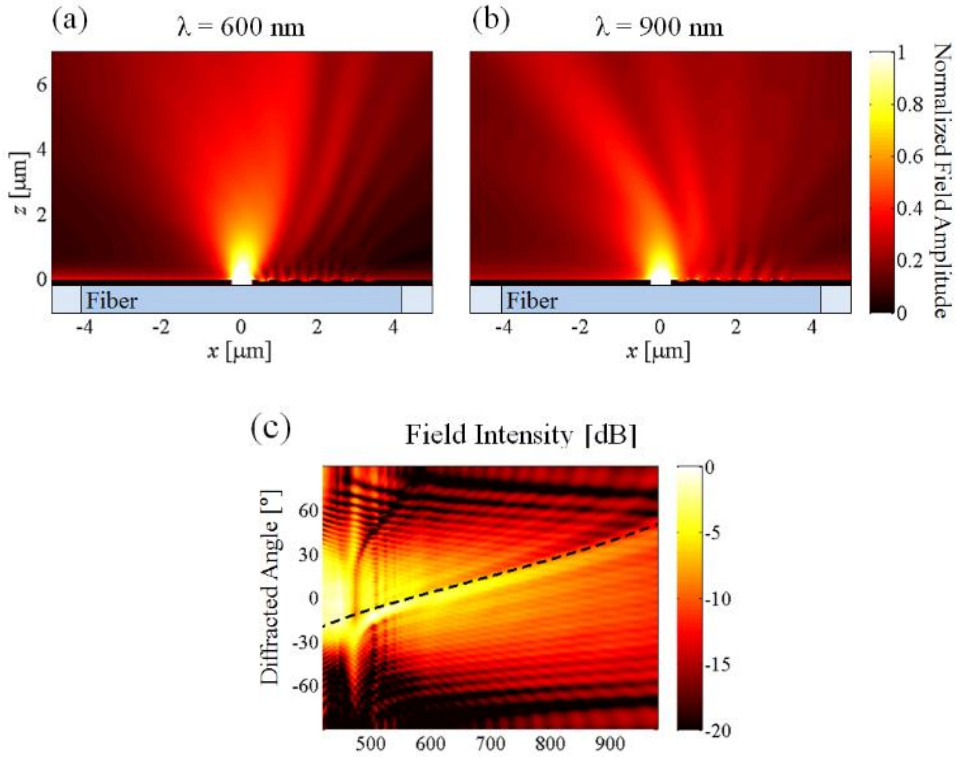

Fig. 2.2.2. Field pattern above the fiber-facet when the wave of the incident light is (a) 600 nm and (b) 900 nm. (c) Numerical (colormap) and analytical (black dash) results of the overall WODB.

The field amplitude patterns obtained by the FEM numerical method are shown in Fig. 2.2.2(a) and Fig. 2.2.2(b) when the free space wavelength of the incident light is given by 600 nm and 900 nm, respectively. Comparing the two results, one can clearly see that the primary beaming angle is substantially different depending on wavelength whilst the incident fiber modes are all in fundamental modes. The overall WODB as a function of wavelength is shown in Fig. 2.2.2(c). The brightest field intensity distribution running from the left-bottom corner to the right-top corner denotes the primary beaming angle of radiation from the end of the MCF-GANS. In

particular, the black dashed line in Fig. 2.2.2(c) indicates the result obtained by using the analytic method based on Eq. (2.2.1), which is, in fact, given by the first-order phase-matching angle for each wavelength. One can see that both results are in good agreement. The result also highlights a good linearity in terms of the WODB angle. In the given condition, one can expect a WODB angle ranging from –15.7° to 49.2° for radiation tuned from 505 nm to 975 nm, leading to a WODB sensitivity of 0.132°/nm.

One can also observe unique phenomena due to SP characteristic. In Fig. 2.2.2(b), the trajectory of the diffracted light does not follow a straight line like an Airy beam [30], which is due to the plasmonic effect introduced by the dielectric-metal interface. This phenomena can be understood as interactions of the secondary radiations generated by the individual charge oscillations at the edges of the rectangular grooves whose phases are delayed by the propagation of the SP across the air-metal groove interface. Also at the left side of Fig. 2.2.2(c), one can observe that at low wavelength (~400 nm), the light spreads to every direction. At this wavelength regime, the slit is large enough to transmit light without generating any SPs, therefore most of the light is diffracted without being affected by the grating.

2.2.2 Experiment results

The MCF-GANS is demonstrated. To coat the fiber-facet with metal, electron-beam evaporation system was used. Silver was selected as the coating material. After coating the fiber-facet with silver, FIB

milling process to fabricate the MCF-GANS [33, 34] was applied to fabricate the same structure calculated from the numerical simulation. Fig. 2.2.3(a) and 2.2.3(b) show the facet images of the processed silver-coated fiber-facet.

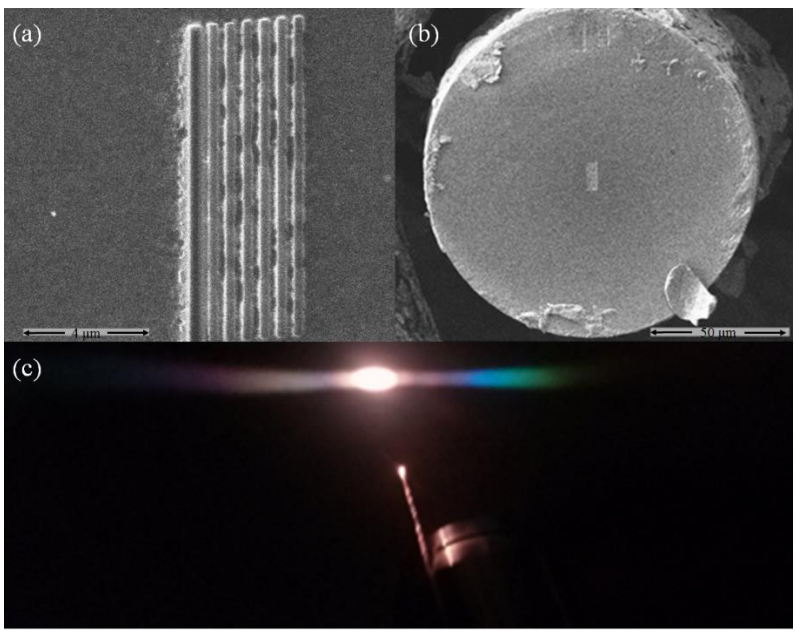

Fig. 2.2.3. (a), (b) The FIB image of the fiber. (c) CCD image.

To conclude, a MCF-GANS implemented on a fiber platform for WDB has been proposed and demonstrated. The model was designed with numerical simulations and its property was shown, then the proposed scheme was demonstrated. Due to the high-accuracy FIB process, the fabricated fiber end exhibited a good WDB characteristic, as expected from the numerical modeling. The output beam pattern of the MCF-GANS showed a rainbow-like pattern when a SC source was launched. From these results, it is clearly shown that the light is diffracted by the periodic grating and shows WDB behavior, and one can properly design a MCF-GANS showing desired performance.

As WDB with high fidelity can widely be used for a variety of applications, especially for fiber-optics, the proposed MCF-GANS is expected to overcome a limitation the usage of conventional diffraction gratings by reducing the required device and space. It is expected that the proposed scheme will be useful for various applications where WDB is required.

2.3. Fiberized plasmonic Fresnel zone plate

Radially polarized focused light (RPFL) has been extensively studied for its fascinating features, which are useful for various applications [40, 83-87]. For instance, RPFL has a relatively small spot size than the linear polarized hotspots, so RPFL has been utilized on various applications such as micro-machining [86], sensing [40], etc. Moreover, the RPFL has a is known to have an advance on optical trapping due to its cylindrical symmetric optical force [87, 88].

Applying RPFL in these applications, there are two significant challenging factors to consider. One is the power of the focused light, and the other is the fine control of its focal position. In terms of power, high intensity CW is required for trapping, and high temporal peak power is required for machining. In the other hand, fine control of the focal point of RPFL is essentially of great interest in various nano-scaled applications. The traditional method for controlling the focal point is to simply move the whole focusing system or the objective itself. Obviously, this will cause relatively large inaccuracy and uncertainty to the system.

Here, the goal of this section is to generate a focal point

controllable high-power RPFL. To satisfy these two issues, I introduce a plasmonic Fresnel lens implemented in a fiber platform, fiberized plasmonic Fresnel zone plate (FPFZP). As discussed in Chapter 1, fiber-optics has an advantage on high output power, both on CW and pulse operations. Moreover, it has other fascinating advantages such as compactness, cost effectiveness, and high accessibility for other optic devices. Especially, readily prepared CV beam sources can be integrated in the fiber [89].

Circular metal nano-slit based on SP has recently been used as a tool of generating RPFL [90-92]. Two fundamental features of the extraordinary transmission (EOT) [13] supports the radial focusing. First, the SP is only formed on polarization which is perpendicular to the nano-slit, so the subwavelength nano-slit polarizes the transmitted light. Therefore, circular metal nano-slit will only transmit radially polarized light. Also, the additional structures – such as gratings, additional materials, or multi slits – diffracts the transmitted light [11]. For these reason, well-arranged multiple circular metal nano-slits, also known as plasmonic lens, has an advantage on generating RPFL. It is known that the plasmonic lens has higher chromatic aberration, which means the focal length varies in terms of wavelength, than the conventional lens [93, 94]. Some researches regard this phenomena as a defect and attempts to reduce the aberration. For example, Venugopalan et al. uses an elaborated slit-grating structure [93], and Wan et al. combines a conventional Fresnel plate [94]. However, in terms of controlling the focal point, it can rather be a controllable characteristic. By the high chromatic

aberration of the plasmonic lens, tuning the wavelength is able to be the means on controlling the focal length.

Consequently, a metal Fresnel plate implemented is an all-fiber format is capable to provide wavelength-dependent position-controllable RPFL, in a high-power regime. In particular, the fiber platform format also allows simple control of wavelength. Thus, this integrated scheme can offer a great merit of localizing and intensifying the resultant RPFL in a compact and efficient form.

2.3.1 Modeling

It is shown in Chapter 2.2 that the proposed structure is able to control the beaming path by tuning the wavelength in the previous section. Conceptually a change of wavelength ($d\lambda$) leads to a change of angle ($d\theta$). By the fact, the idea can be extended from angle to position. If a properly designed structure which has a cylindrical symmetric geometry, a circular nano-slit for example, the diffracted light can be focused in one spot. Thanks to the nature of SP, the focused light will have a radial polarization. Furthermore, as the wavelength varies, the position of the focal point will also vary. In other words, change of wavelength ($d\lambda$) will lead to a change of a focal length (df). In particular, a Fresnel metal plate implemented on a fiber-facet is proposed to generate a wavelength-dependent position tunable RPFL. It is notable that a full-vectorial RPFL in the free-space is generated by the FPFZP.

The schematic of the proposed FPFZP structure is shown in Fig. 2.3.1, including its cross-sectional view and the fiber-optical field

intensity pattern across the diameter of the fiber. As depicted in Fig. 2.3.1(b), the strategy of the chapter is to generate an RPFL and control the position of the hotspot by tuning the wavelength of the incident light.

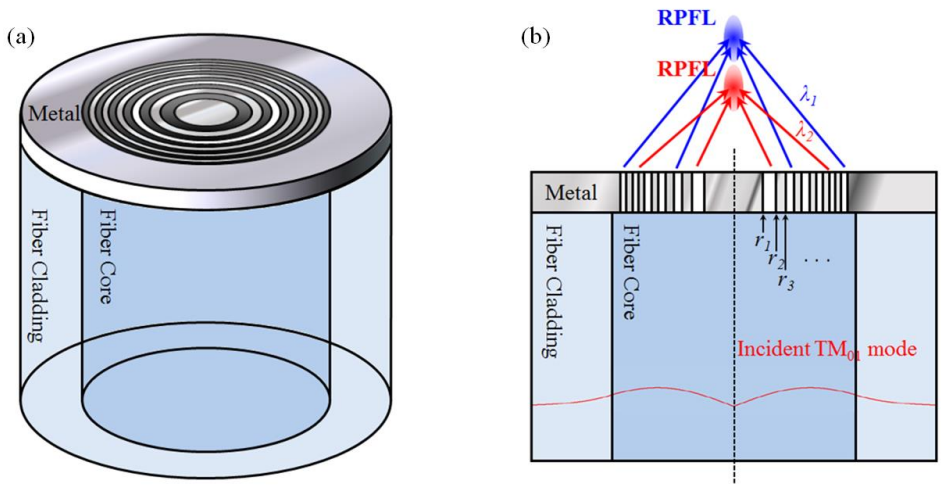

Fig. 2.3.1. (a) The structure and (b) The cross-section and its operation concept of the FPFZP.

Numerical simulations (FEM: COMSOL Multiphysics®) and analytical calculations are performed to analyze the FPFZP structure. The fiber is assumed as a standard multi-mode step-index fiber (MMF), which has a core diameter of 50 μm, and a numerical aperture of 0.14. For numerical analysis, the input light was set to the TM_{01} mode of the MMF. The metal is assumed as silver. The material parameters, i.e., the refractive index and extinction coefficient, of the silver are given in Ref. [82]. The thickness of the metal coating is set to 500 nm. The center of the Fresnel plate is assumed to be concentric with the center of the fiber core. In addition, it is worth noting that this metallic structure can readily be fabricated

via the conventional e-beam [60] or FIB technology [33, 34]. The pattern of the Fresnel is shown in Eq. (2.3.1).

$$r_n = \sqrt{n\lambda_0 f + \frac{n^2\lambda_0^2}{4}}, \text{ (n = 1, 2, ...)} \qquad (2.3.1)$$

2.3.2 Focal length tunability

Refer to Eq. 2.3.1, note that one can design the operation wavelength and the focal point. Two designs are shown in this section, while one is for operation on infrared (IR) regime, and the other is for operation on visible regime. These patterns were demonstrated to verify the structure is applicable on various focal length and wavelength regimes. The first pattern is matched on focal lengths of f = 20 μm at free space wavelength of each λ_0 = 550 nm, and the second is matched on f = 10 μm and λ_0 = 1015 nm. The later wavelength is selected for a typical Yb doped fiber laser [8]. r_n is the nth radius of the Fresnel plate, whether closed or opened. 6 slits are engraved at the core region, where n = 12 in Eq. 2.3.1.

Figure 2.3.2 shows the field intensity pattern of the FPFZP on IR regime, while the incident wavelength is 900 nm, 1015 nm, 1050 nm respectively. It is shown at the picture that the FPFZP generates RPFL clearly above the fiber-facet, and the position of the focal point decreases while the wavelength increases. It is notable that one can observe beams are diffracted and concentrated at the focal point, and passes away from the field pattern, which corresponds with the previous section. From the properties, the output beam of the FPFZP can be regarded as a Bessel beam. It is already know that a Fresnel

zone plate could generate a Bessel beam, and the radially polarized hotspot occurs in the waist of the beam [95].

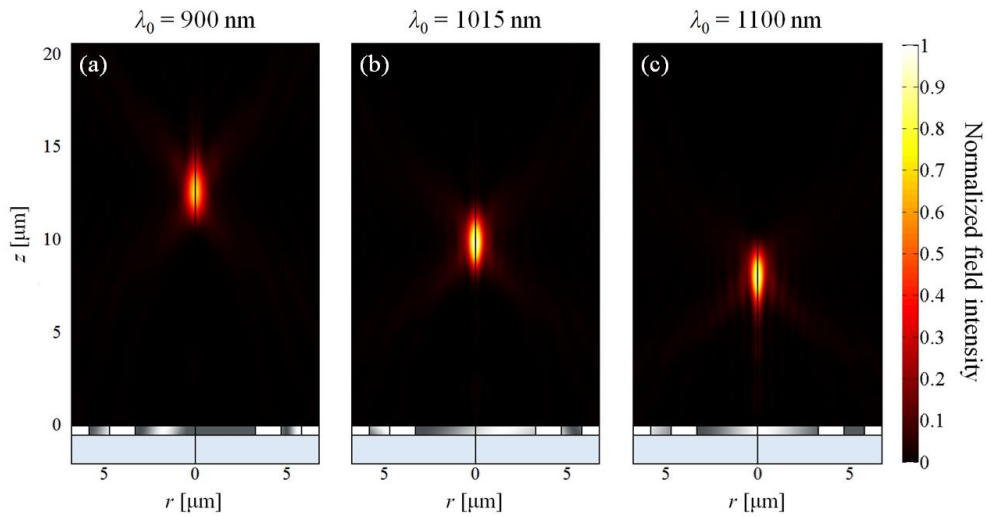

Fig. 2.3.2. The field pattern of the FPFZP structure on wavelength at (a) 900 nm, (b) 1015 nm and (c) 1100 nm.

Figure 2.3.3(a) and 2.3.3(b) shows the calculated optical field intensity at $r = 0$ of the FPFZP where its operation regime is each IR and visible regime respectively. From the figure, a bright area starting from left-top side to right-bottom side exists. In other word, increase of wavelength will lead to decrease of focal length.

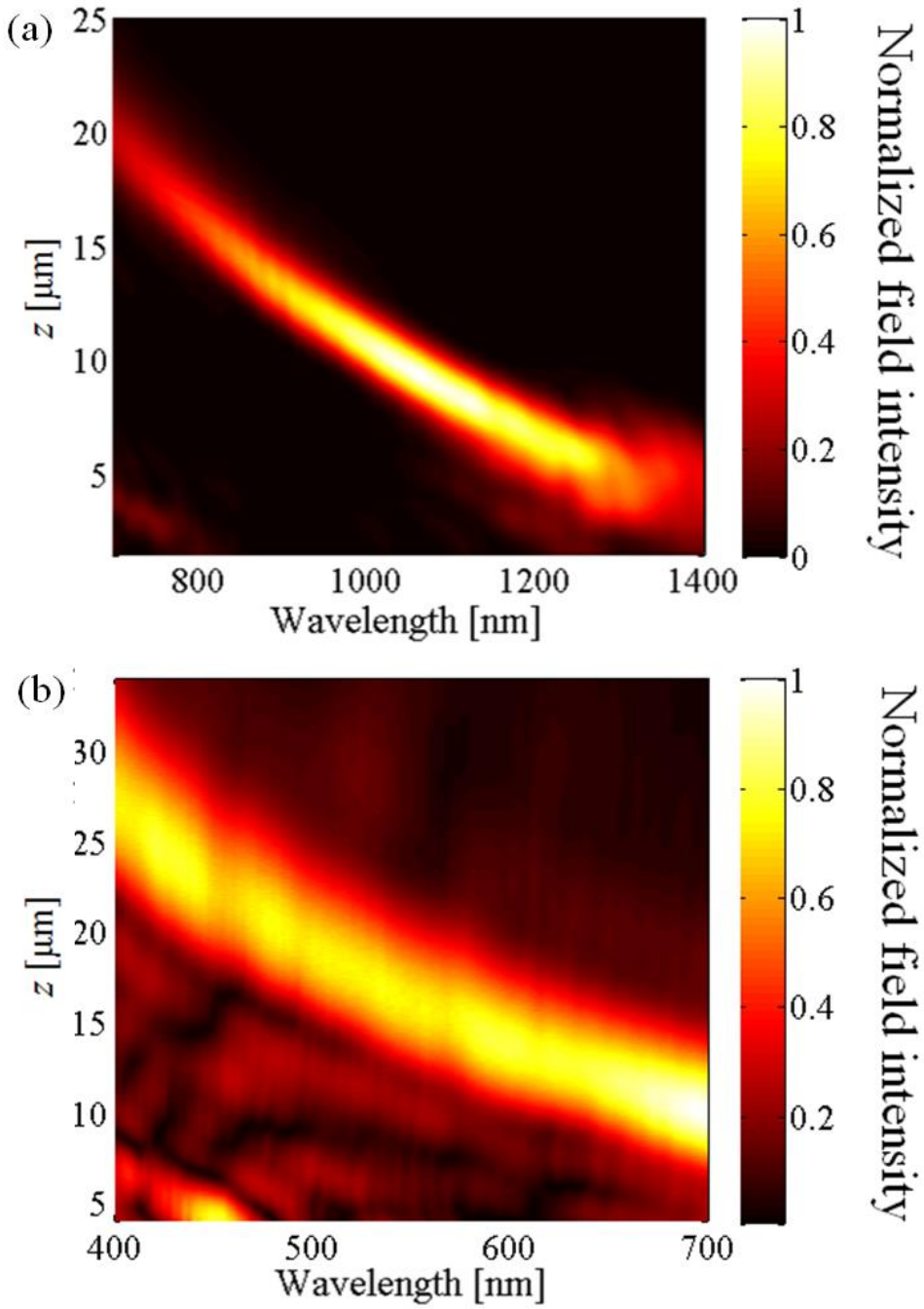

Fig. 2.3.3. The numerical results of the field intensity in following the z axis, where $r = 0$ in terms of wavelength for (a) IR and (b) visible regime.

As shown above, one can generate an RPFL and tune the position

of it. One can control the focal length without affecting the operation area. Furthermore, the fiber platform enables a high power CW laser or a pulse laser input, the FPFZP could generate a coherent focal point with high power intensity [8].

2.3.3 Trapping capability

As the focal length of the FPFZP is tunable, if the RPFL has a possibility to trap a particle, tunable trapping position with FPFZP can be achieved. It is well known that the RPFL has an advance on trapping nanoparticles [87, 88]. In this section, the FPFZP on IR regime is applied for further calculations. To verify the capability of the trapping performance of the FPFZP, two optical forces, the scattering force and the gradient force, are calculated. If the particle is relatively smaller than the wavelength, the scattering force and the gradient force of the dielectric nanoparticle at the free space can be derived as the following equation:

$$F_G = \frac{\varepsilon_0 \alpha n_m^2}{4} \nabla I \ , \quad F_s = \frac{n_m^5 k_0^4}{6\pi} \alpha^2 \vec{P} \ , \qquad (2.3.2)$$

while F_G and F_S denotes the optical gradient force and the optical scattering force, respectively, and ε_0 is the permittivity of the vacuum, I is the field intensity, n_m is the refractive index of the particle, k_0 is the wavenumber at free space, $\vec{P}$ is the poynting vector. α is the polarizability of the particle, and the value is shown in Eq. (2.3.3).

$$\alpha = 4\pi a^3 \frac{n_m^2 - 1}{n_m^2 + 2} \qquad (2.3.3)$$

while *a* is the radius of the particle. The material of the nanoparticle is assumed as silicon dioxide (SiO_2). The radius of the nanoparticle is set to 50 nm, and the refractive index followed Ref. [96]. From the numerical results, the optical force were derived. The input power assumed as 100 mW, which is not a difficult power to be obtained on a fiber laser [8].

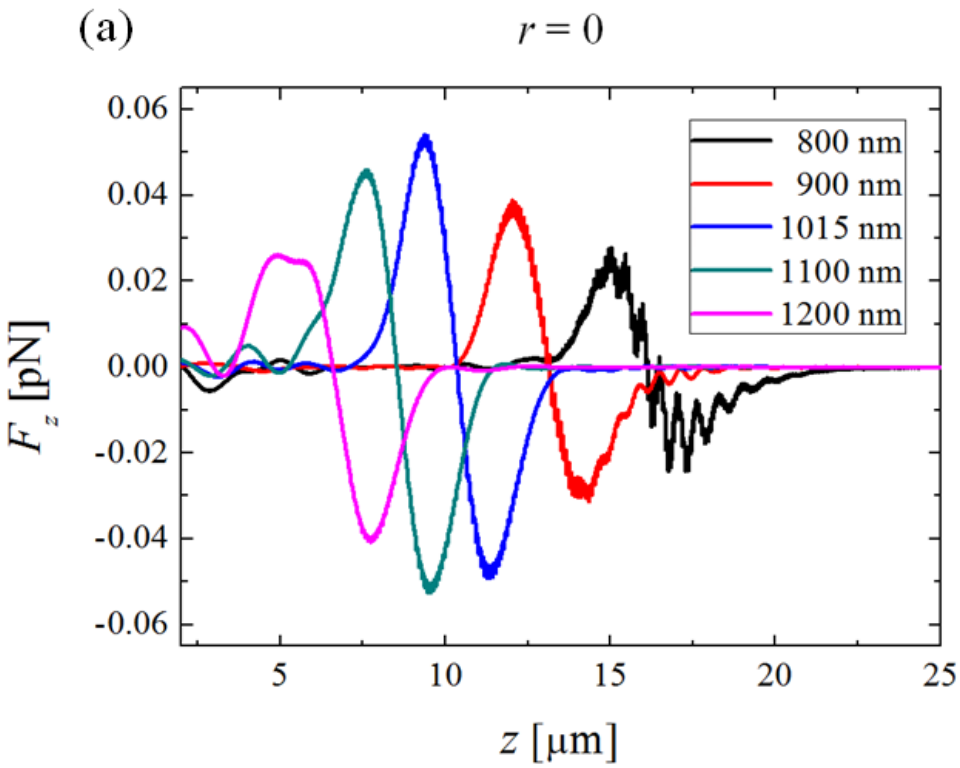

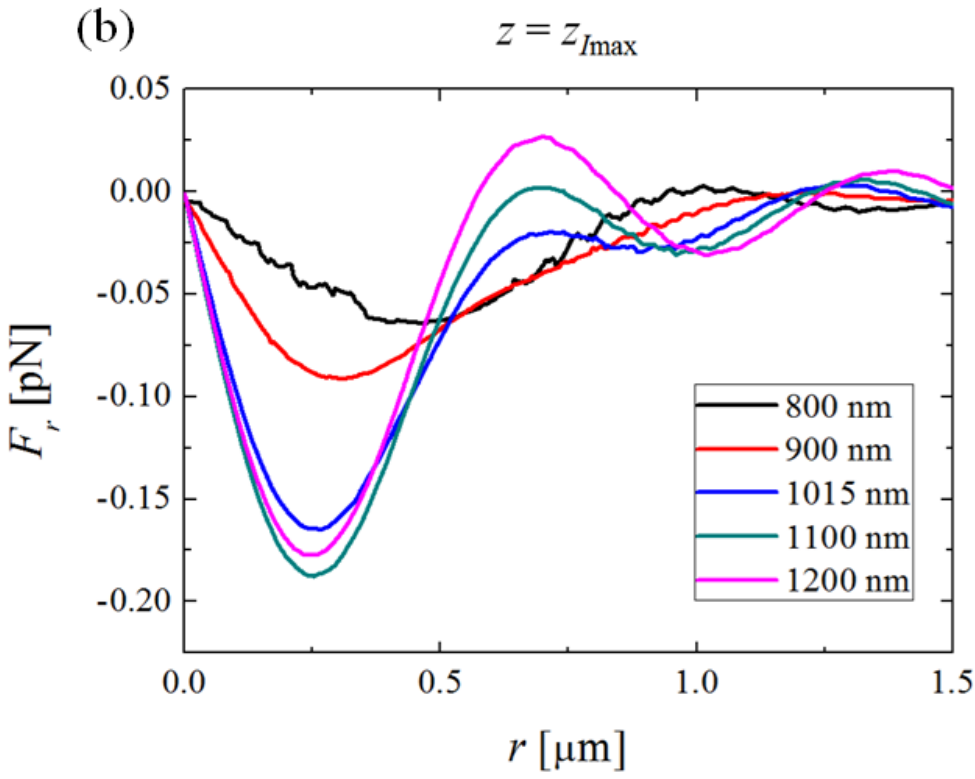

Fig. 2.3.4. (a) The optical force in the vertical direction at r = 0 (on the fiber axis) and (b) the optical force in the radial direction at z = z_{Imax} (on the center of RPFL) when 1015 nm input light is illuminated.

The calculated optical forces at wavelength 800 nm to 1200 nm are shown at Fig. 2.3.4. F_z at the center of the fiber axis where r = 0 is shown in Fig. 2.3.4(a), while F_r at the focal point where the intensity of the RPFL is highest, is shown in Fig 2.3.4(b). It is clear that the optical power leads toward the RPFL, which is proper for trapping. Also one can see that the z direction stable position varies in terms of wavelength. It is notable that F_r is slightly larger than F_z, and this could be caused by that the width of the r direction of the RPFL is shorter than that of the z direction.

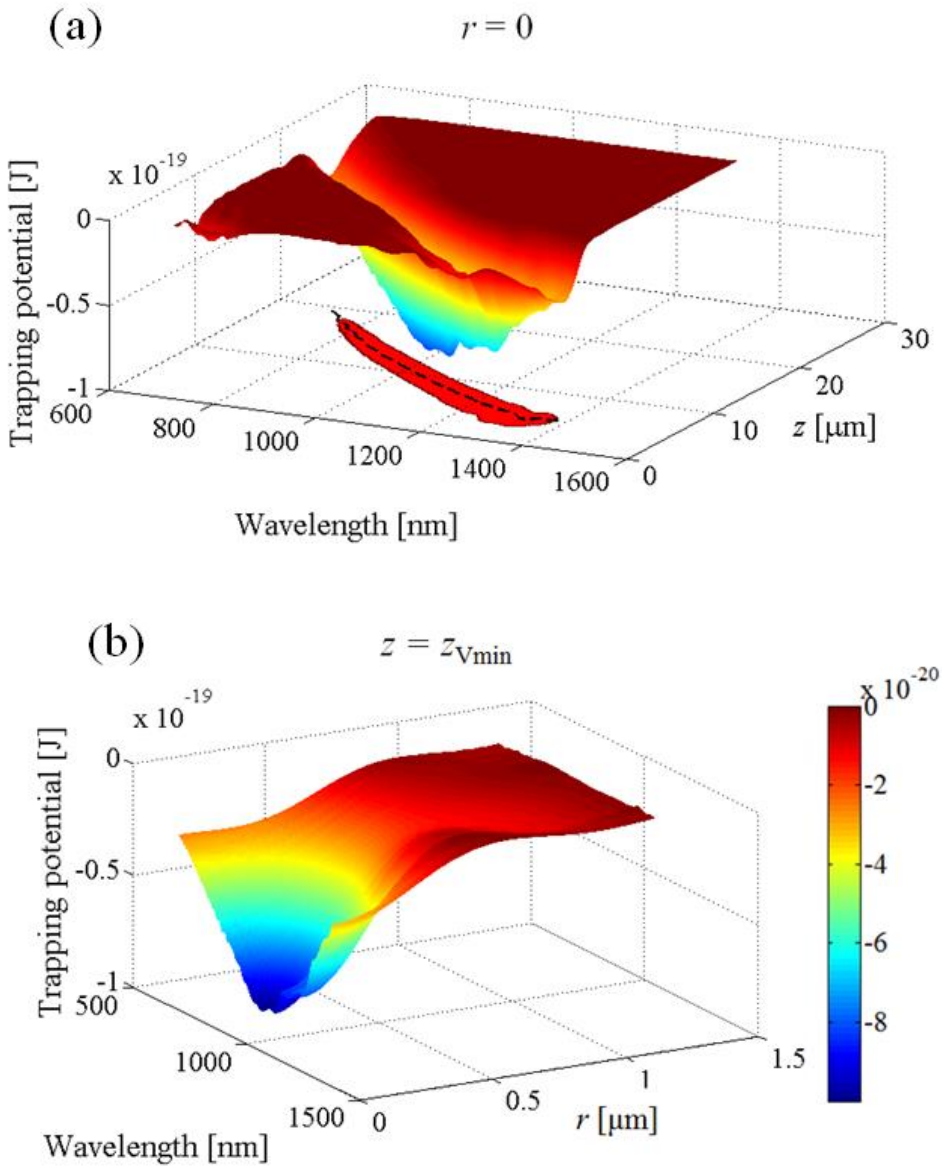

Fig. 2.3.5. (a) The optical potential energy in the vertical direction at r = 0 (on the fiber axis) in terms of wavelength. The black dashed line shows where the potential is minimum, and the region which has a deeper potential than the 7 $k_B T$. (b) The optical potential energy in the radial direction at $z = z_{Vmin}$ (black dashed line depicted in Fig. 2.3.4(a)) in terms of wavelength.

From the calculated optical force, the optical trapping potential

energy was derived. Figure 2.3.5(a) shows the trapping potential following the fiber axis in terms of wavelength. The black dashed line shows where the potential is minimum. At that z position where the potential energy is minimum, the potential following the r axis is derived. Figure 2.3.5(b) shows the optical potential energy in the vertical direction at $z = z_{Vmin}$, which is the black line depicted in Fig. 2.3.5(a), in terms of wavelength.

One can see that the potential well exists both in r and z direction. As the optical gradient force is dominant than the scattering force when the particle is small enough, the potential pattern shows similar trend with the negative of the optical force, and the minimum potential position are nearly equal to the focal point.

To check the validity of the optical trapping, three conditions must be satisfied [87, 88, 97]. First, the gradient field to scattering field ratio $R_{GS} = F_{G\_z} / F_{S\_z}$, which is known as stability criterion, must be greater than 1. The mean and max criterion in the FWHM region of the RPFL beam spot was calculated. In the calculated region from 700 nm to 1400 nm, the stability criterion always exceeds 1. In practical wavelengths, the R_{GS} of max force and mean force at wavelength 1015 nm is 15.40, 18.77 respectively. Second qualification is that the optical force must be higher than the gravity force. In the case of the suggested particle, the gradient force is 1.350×10^{-17} N. In the calculated region from 700 nm to 1400 nm, the weakest force in the FWHM region of the RPFL beam spot was 5.181×10^{-15} for F_z and 1.096×10^{-14} for F_r, which is more than 2 orders higher than the gravity force. Refer to Fig. 2.3.4, it is clear

that the gradient force (~10^{-5} pN) is negligible. Finally, the potential well must be deep enough to store the particle energy, which is known as $k_B T$ where k_B is the Boltzmann constant and T is the degree. It is known that a potential higher than 7 $k_B T$ (= 2.899 × 10^{-20} J) is enough to trap the particle [97]. The region which has a deeper potential than the 7 $k_B T$ value is depicted in Fig. 2.3.5(a), filled red at the bottom. From these conditions, the model is enough to trap a particle in 100 mW, and could efficiently trap the particle on higher power.

As numerically demonstrated above, the generated RPFL is capable to trap a nanoparticle, and control the position of the particle by only modifying the wavelength of the input light. The proposed FPFZP fiber could tune the trapped position without any external force exerted to the system. Also, utilizing a sweeping source, it is expected to oscillate the trapped particle.

2.3.4 Experimental results

To examine the performance of FPFZP, the device has been demonstrated. To coat the fiber-facet with metal, electron-beam evaporation system was used. Silver was selected as the coating material. After coating the fiber-facet with silver, a FIB milling process was applied to fabricate the FPFZP. The same structure calculated from the numerical simulation was fabricated as in the previous section. Fig. 2.3.6 show the facet images of the processed FPFZP.

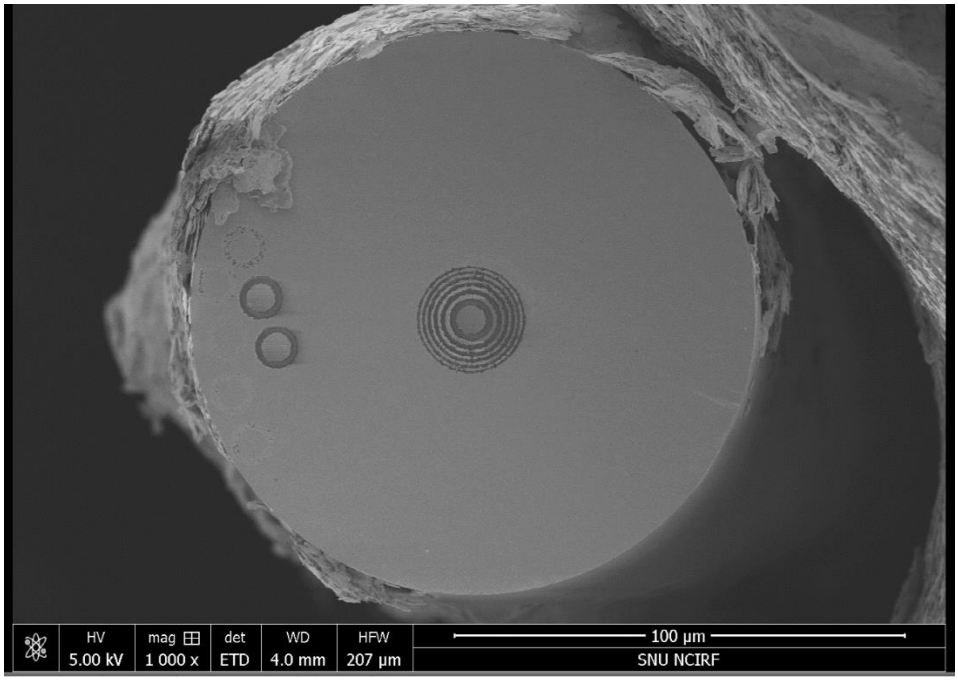

Fig. 2.3.6. The SEM image of the FPFZP.

Then, three colors of light were launched into the fiber. The wavelength of each colors were 473.4 nm for blue, 527.1 nm for green, and 611.9 nm for red. The focal length is retrieved using a setup connected to a microscope as depicted in Fig. 2.3.7(a). Controlling the distance of the microscope, each CMOS images from different focal length are taken.

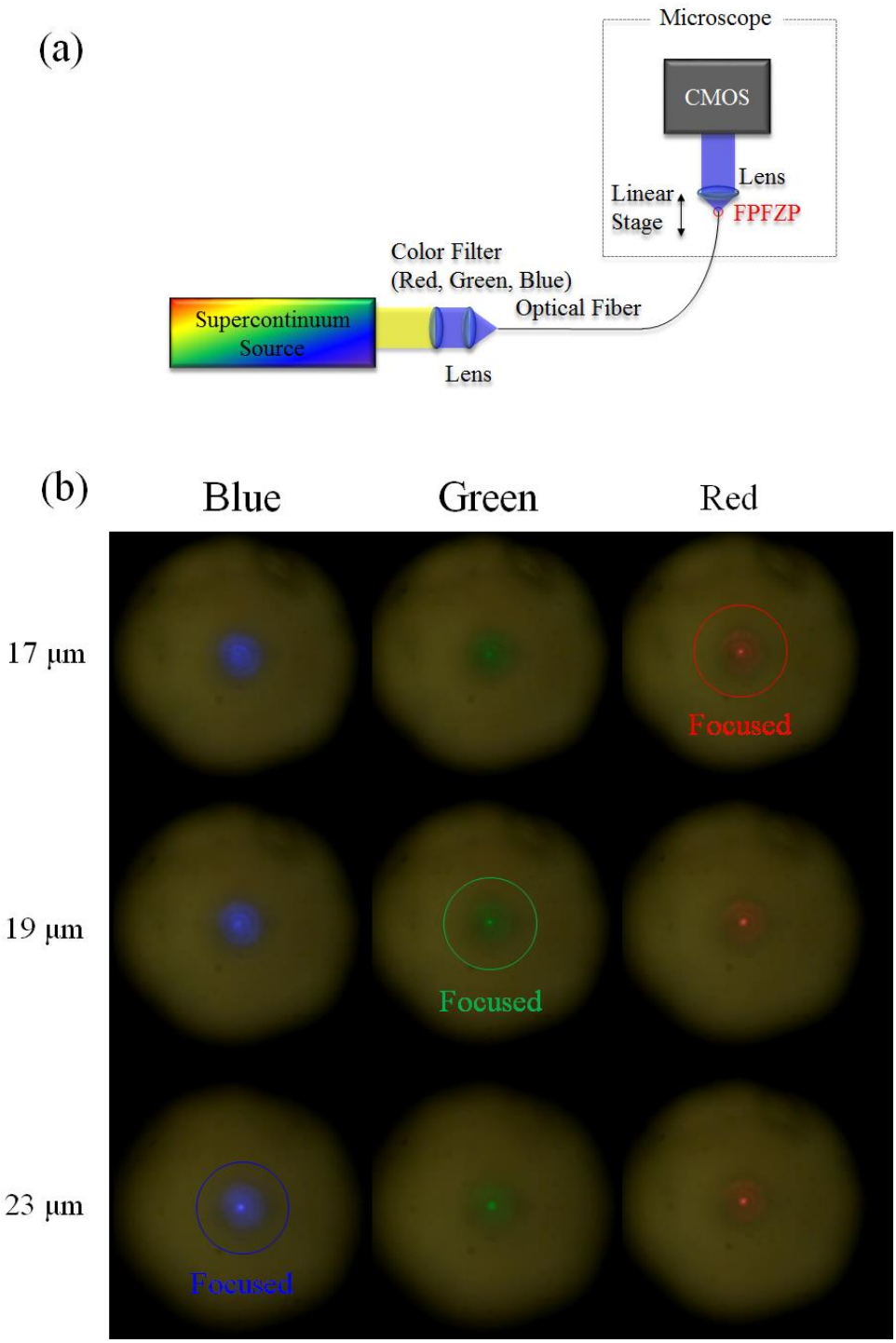

Fig. 2.3.7. (a) Schematic of the experiment setup. (b) The CMOS images for three colors in terms of distance.

As the operation range was matched to the visible range, one can

see the light is tightly focused. The focal length was ~23 μm for blue, ~19 μm for green and ~17 μm for red. As the FPFZP was designed for focal length of 20 μm in 550 nm, the focal lengths were fit in the operation regime. The result showed that longer wavelength had shorter focal length. One can observe that the focal point differs for each wavelengths. Also, the focal distance considerably matches with that of the numerical results, compare to Fig. 2.3.3(b).

Chapter 3

Metal coated Angled fiber-facet

In this chapter, a novel fiber-optic mode to SP mode conversion scheme is introduced. In general, dedicated coupling methods have to be utilized to generate SPs because their wavenumbers are invariably larger than that of free-space light. A handful of commonly used SP-coupling methods are exemplified by prism coupling schemes, nano-aperture schemes, and grating-assisted schemes, such as introduced in Chapter 1. However, these conventional SP-coupling techniques show a significant trade-off and limitation amongst various aspects, including compactness, flexibility, efficacy in unidirectional coupling, controllability in SP spot size, efficiency in optical to SP conversion, etc. Not compromising with such aforementioned aspects, a metal coated angled fiber-facet coupling configuration is proposed. The design uses a thin metal layer coated on the surface of an angled fiber-facet. It is shown through both numerical simulations and experimental demonstrations that the proposed configuration can be used as an efficient SP-coupling method for optical-SP hybrid devices with substantially enhanced properties, compared to those based on the conventional techniques. Also, additional applications using this configuration are proposed.

3.1 Metal coated angled fiber-facet coupling scheme

3.1.1 Numerical modeling

In general, fiber-facet-based devices for SP generation adopt subwavelength-scaled apertures or nano-slit structures. Topics on Chapter 2 was also based on nano-slits for SP generation. However, in this case the fiber-to-SP mode coupling efficiency is significantly lowered by three factors: First is the excitation of non-confined diffracted light and second is the generation of unwanted SPs propagating in the opposite direction that invariably fails to see the target grating structure on one side, and third is the reflected component which cannot pass the slit, as depicted in Fig. 3.1.1(a). For monochromatic applications, it may be possible to exploit an additional grating structure in order to redirect the anti-propagating SPs [98], which cannot be an ultimate solution because some devices normally require broadband functionality. However, the numerical results showed that the amount of reflection was dominant. For slit structures, 90~95 % of reflection was observed, which means the intensity far from the slit failed to pass through the slit. For planar structures, additional grating beneath the slit or oblique incidence reduce the reflection, however these are difficult on fiberized scheme.

Consequently, replacing the Kretschmann's configuration [21] to an angled fiber-facet, which is schematically depicted in Fig. 3.1.1(b), this issue will be resolved.

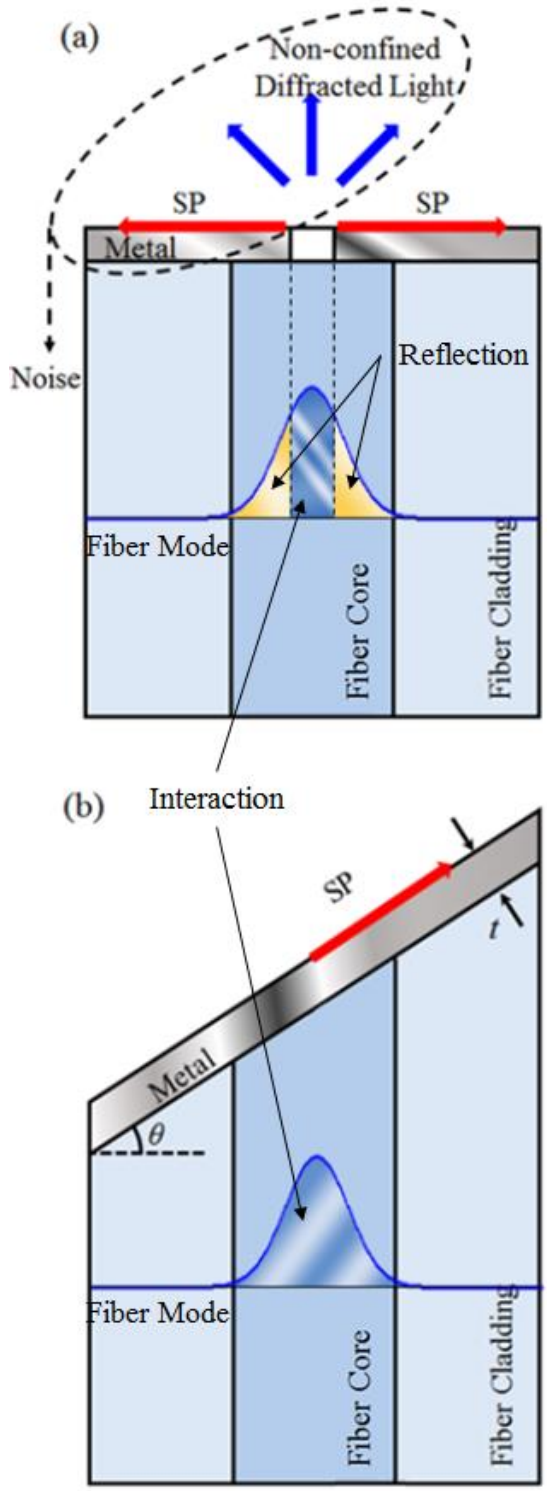

Fig. 3.1.1. Fiber-SP-mode coupling schemes: (a) Nano-slit coupling scheme and (b) MCFF scheme.

The prism coupling technique based on the Kretschmann's configuration is one of the most frequently used methods to generate SPs [21, 99], which is normally based on an oblique incidence towards a dielectric–metal interface where the real part of the dielectric material should be higher than that of the metal. Note that if the fiber has an angled termination, the angled fiber–facet itself can play exactly the same role as a prism. Without loss of generality, this MCAFF can generate SPs along the metal surface when the following phase–matching condition is satisfied:

$$k_{SP0} = n_{eff} k_0 \sin\theta, k_{SP0} = k_0 \sqrt{\frac{\varepsilon_d \varepsilon_m}{\varepsilon_d + \varepsilon_m}}, \qquad (3.1.1)$$

where k_0 denotes the wavenumber of the radiation in free space, k_{SP0} the wavenumber of the SP; ε_d and ε_m denote the electric permittivities of the dielectric and the metal, respectively, n_{eff} the effective refractive index of the fiber mode, and θ the incidence angle of the fiber mode to the fiber–metal interface or simply the angle of the fiber–facet relative to the fiber axis.

Whilst the proposed scheme relies, in principle, on the well–known Kretschmann's configuration, one distinct aspect is the fact that the incident wave is given not by a free–space beam or a plane wave, but by a fiber mode that is localized within the core of the fiber and its vicinity area. This makes a very important point because the "localized" fiber mode can generate LSPs as well as normal SPs that are determined only by the air–metal interface [11, 20, 100]. If the metal layer is thin, the influence by LSPs as insulator–metal–

insulator (IMI: dielectric–metal–air) SPs becomes further significant. Consequently, the conventional approaches based on the rigorously coupled wave analysis (RCWA) that takes account of only normal SPs may result in inaccurate outcomes for the proposed scheme. Hence, choosing to perform a full numerical calculation based on the finite element method (FEM via COMSOL Multiphysics®) will eventually lead to a more rigorous analysis on the proposed scheme, including the influence and effect by LSPs.

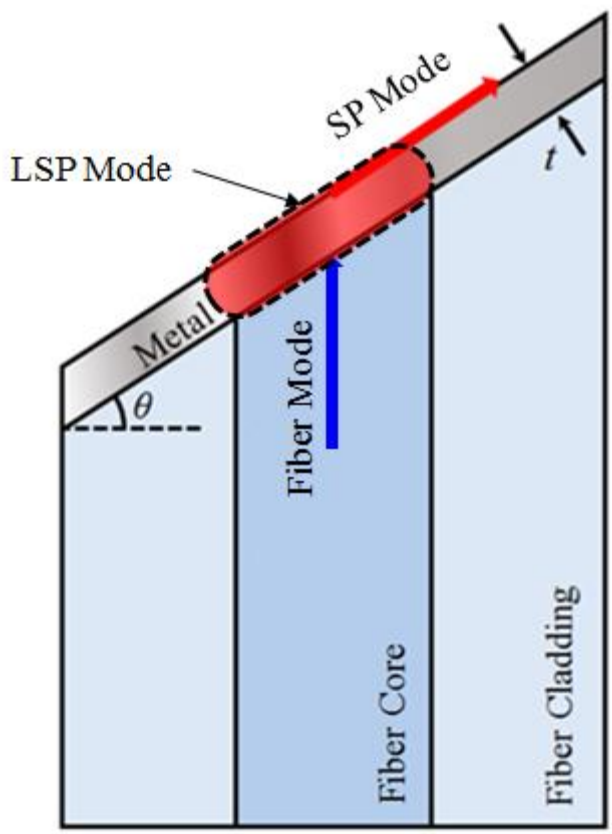

Fig. 3.1.2. LSP mode excitation for the case of thin metal.

For the metal coating material silver is considered from the viewpoint of the simplicity and cost–effectiveness to demonstrate

the functionality of the proposed WODB in the visible to near-infrared range as was demonstrated in the previous section. (Note that gold or any other good conductors can also be utilized instead, depending on the purpose of the target application.) The material parameters of silver, i.e., its refractive index and extinction coefficient, are given in detail in Ref. [82]. The fiber is assumed as a step-index fiber with a core diameter of 3 μm and a numerical aperture of 0.1, which provides 391.88 nm single mode cutoff frequency. This design allows single-mode operation in the visible range (400 to 700 nm).

Initially, the thickness of the metal layer to coat upon the fiber-facet and its angle relative to the fiber axis, i.e., θ, must be determined in order that the device is suitable for broadband SP coupling. Note that in the conventional Kretschmann's configuration with a prism, the thickness of the metal layer is normally given by 30 to 50 nm [21, 99], and the incidence angle is externally determined and fine-tuned by free-space launching, depending on the wavelength of the incident beam. In contrast, the proposed scheme relies on the full fiber-optic scheme, such that the incidence condition is pre-determined by the angle of the fiber-facet for any spectral radiation through it. Thus, it is very important to choose a right value for the fiber-facet angle because it primarily defines the spectral range of SP coupling.

In Fig. 3.1.3(a) it is shown that how the fiber mode is coupled into SPs, in which the thickness of the metal layer, the fiber-facet angle, and the wavelength of the input radiation are given by 20 nm,

45° , and 600 nm, respectively, as a typical example. The incident fiber mode is assumed to be an x-polarized LP_{01} mode, which is of a proper polarization to excite SPs on the metal surface in the given geometry [i.e., insulator-metal-insulator (IMI) structure] without loss of generality. One can see that when the x-polarized LP_{01} mode is obliquely incident onto the IMI structure, a fraction of it is immediately reflected to the side of the optical fiber and the rest of it is coupled into SPs. These SPs propagate parallel to the IMI structure, undergoing gradual attenuation. Note that there are two main mechanisms for the attenuation: One is due to the ohmic loss by the metal layer itself, and the other is due to the decoupling of the propagating SPs back into the dielectric, i.e., into the side of the optical fiber. For example, in the right-top-corner of the cladding region of the optical fiber indicated by a round-rectangle in a dashed-line in Fig. 3.1.3(a), the optical radiation to the right side is mainly due to the latter effect. This is significantly distinguished from the direct reflection of the incident radiation occurring in the core region, because the incident optical radiation in the cladding region is negligible. This decoupling of the propagating SPs can be avoided if the thickness of the metal layer increases; however, in this case the ohmic loss turns up more significantly.

Thus, the optical-to-SP coupling efficiency is calculated by varying the thickness of the metal layer and the angle of the fiber-facet for the spectral range from 400 to 700 nm, and the results are shown in Fig. 3.1.3(b). The *overall optical-to-SP coupling efficiency* is defined as the averaged out coupling efficiency over the spectral

range from 400 and 700 nm within the core region. For applications which directly use only the coupled SP, this factor may be the figure of merit. As shown in Fig. 3.1.3(b), the *overall optical-to-SP coupling efficiency* increases to a significant level as the thickness of the metal layer decreases down below 30 nm, which also slightly varies with the angle of the fiber-facet around 45° via Eq. (3.1.1). Such efficiency levels are significantly high, compared to conventional nano-slit-based devices [101], even with the fact that it is the value averaged out for the spectral range from 400 to 700 nm. In this stage, subtle optimization of the fiber-facet angle is unnecessary because it is followed by a periodically corrugated structure on the top of the metal layer for WODB functionality, which will slightly alter the effective phase-matching condition of the optical-to-SP coupling.

In conventional Kretschmann's configurations, the use of a thin metal layer of below 30 nm is not often used because it can hit a backward SP-to-optical decoupling issue when SPs propagate a significantly extended distance, as discussed earlier. However, in the case for applications right above the core region, it will not be a critical issue. Therefore, for those cases, it is able to consider that the thickness of the metal layer below 30 nm. This will be further confirmed and verified in the following section. Notwithstanding, the use of too thin a metal layer of below the skin depth of the metal, which is in the range of approximately 10 to 15 nm for silver for optical radiation in the visible to the near infrared range, must be avoided because it can cause direct tunneling of the optical fiber mode

into free space. Consequently, the thickness of the metal layer of 20 nm will be appropriate for applications which use the localize SP modes, which is thick enough to prevent the direct tunneling. Moreover, this thickness is fully compatible with the currently available electron-beam (e-beam) coating and FIB milling technologies [33, 34]. Emphatically, this arrangement will offer substantially high *overall optical-to-SP coupling efficiency* in comparison with other nano-slit based coupling schemes. Note that for the case of applications related with propagating SP, the thickness should be thicker than 30 nm to prevent the decoupling loss.

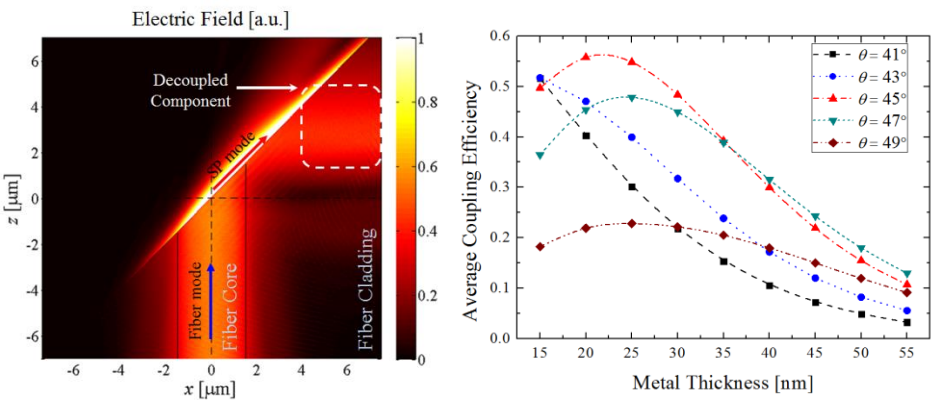

Fig. 3.1.3. (a) Electric field pattern of specific MCAFF configuration. (b) *Overall optical-to-SP coupling efficiency* in term of thickness for the MCAFF scheme.

With the thickness of the metal layer fixed to 20 nm, the spectrum of the optical-to-SP coupling efficiency for various fiber-facet angles around 45° are shown in Fig. 3.1.4. It should be noted that the estimated efficiency is the *individual* optical-to-SP coupling efficiency, not the *overall* optical-to-SP coupling efficiency. The estimated efficiency reaches up close to 70% in some conditions. In

addition, the given IMI structure offers a sufficiently broad spectral bandwidth (SB), being able to cover the targeted visible range (400 to 700 nm). This is due to the fact that the use of the thin metal layer allows for exciting LSPs as well normal metal–air SPs across it. In fact, these enhanced characteristics fully support the proposed scheme to be suitable for an SP–generating platform for WODB functionality. Detailed discussions on the WODB functionality will be discussed in next section.

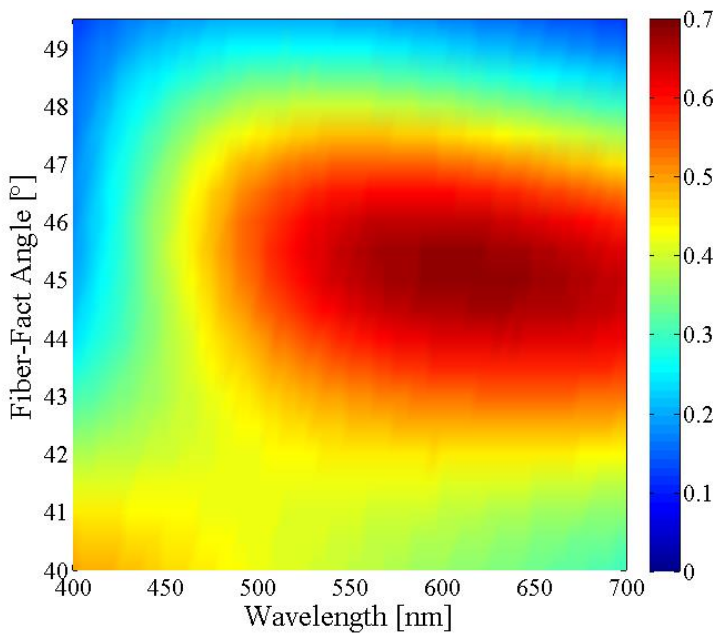

Fig. 3.1.4. Spectrum of individual coupling efficiency in terms of the fiber–facet angle.

3.1.2 Experimental results

The experimental setup is shown in Fig. 3.1.5(a). To conveniently view the coupled SP, the surface was randomly textured before coating. After the metal coating process was applied to the rough

surface, a polarization-tunable source was launched at the other end of the optical fiber. As SP mode is only generated when the electric field is parallel to the paper plane (hereinafter, TM mode), the scattered light caused by the generated SP mode will only appear if the TM component exists. For the experiment, HI-1060 fiber was employed, the fiber-facet angle was $\theta = 46^{\circ}$, and the incident wavelength light was 650 nm. Two different thickness of 20 nm and 30 nm of silver were coated to each samples. The picture of the fiber-facet surface observed with a CMOS camera is shown in Fig. 3.1.3(b) for each polarization mode (left figures for TM, and right figures for TE) and different metal thickness (top figures for 20 nm coating, and bottom figures for 30 nm coating). One can clearly see that more light is scattered when the TM polarized light is launched into the fiber. It is notable that the diffracted light from the 30 nm thickness metal coating seems brighter than that of the 20 nm case. This is due to the fact that the thin metal excites more light at the core. However, it rapidly decays while propagating, as mentioned beforehand.

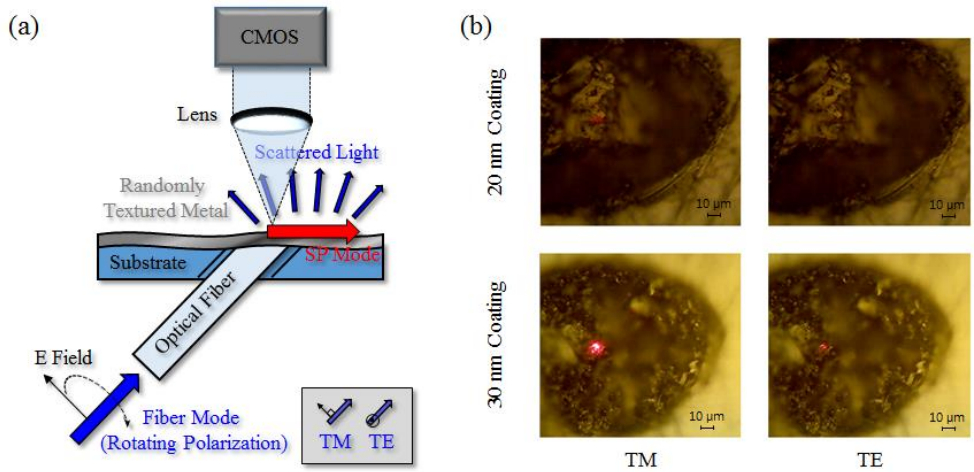

Fig. 3.1.5. (a) The experimental setup for the MCAFF. (b) CMOS images of the experiment.

3.2 Grating-assisted metal coated angled fiber-facet for wavelength-dependent off-axis beaming

3.2.1. Design principle

The first application is for WODB, which an improved version compare to the structure shown in Chapter 2.2. In this section, a grating assisted structure is discussed, which integrates the whole conventional WODB arrangements into an all-fiberized device. The proposed device is schematically depicted in Fig. 3.2.1(a). As described in the previous section, the incident radiation from the optical fiber core can excite SPs at the metal-air interface, which are now supposed to be converted into an optical radiation out of the MCAFF, incorporating WODB functionality. For the sake of introducing WODB functionality, a periodically corrugated one-dimensional grating structure on the top of the metal layer is implemented as shown in Fig. 3.2.1(b). This, namely, grating-

assisted MCAFF (GA-MCAFF) can readily be fabricated by the e-beam and FIB processes [33, 34].

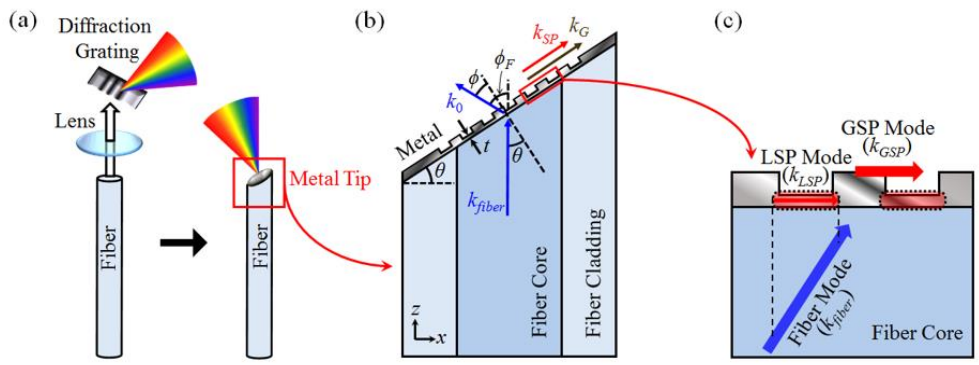

Fig. 3.2.1. (a) Operation schematic of conventional wavelength-dependent directional beaming and of WODB from the proposed structure. (b) The schematic of the proposed fiber-facet. (c) The two generated SP modes at the grated surface.

Before discussing the WODB functionality of the proposed scheme, it is better to first clarify the characteristics of plasmonic oscillations that can be induced in the periodically corrugated metal grating structure. A magnified view of the structure is shown in Fig. 3.2.1(c). One may suppose that there is an incident optical radiation from the bottom of the metal grating structure. In this case, the corrugated metal surface can support three types of SP modes: The first SP mode is LSP oscillation at the valley of the grating where the metal layer is thinnest, as discussed in the previous section [100]. It is depicted as a round-rectangle in a dashed-line in Fig. 3.2.1(c) and is called hereafter the LSP mode. The second is the non-localized, normal SP mode spread out along the whole metal-air interface of the periodical corrugation. It is depicted as a red arrow in Fig. 3.2.1(c)

and is called hereafter the grating-SP (GSP) mode. The last is the SP mode bounded at the fiber-metal interface, which is normally forbidden because of the wavenumber mismatch. However, for certain phase matching conditions, the SP mode bounded at the fiber-metal interface can be coupled by means of the assisted grating. The excitation of this component reduces the diffraction efficiency. This phenomenon will be discussed in the next section.

The local phase variation of the LSP mode primarily relies on the initial phase distribution of the incident optical radiation projected onto the fiber-metal interface. This implies the wavenumber of the LSP is mainly determined by the projected wavenumber of the fiber mode onto the fiber-metal interface,

$$k_{LSP} \approx k_{fiber} \sin \theta. \qquad (3.2.1)$$

The modes are also depicted in Fig. 3.2.1(c). The induced LSP mode is then forced to oscillate with the phase distribution determined by the incident optical radiation. Note that this LSP mode tends to be bounded only in the valley of the grating because the attenuation due to the ohmic loss of the metal is already substantial if the mode travels around the peak of the grating. In other words, the peak segment of the metal grating functions as if it heavily blocks the propagation of the LSP mode, thereby leading to the "localization of plasmonic oscillation" in the valley segment of the metal grating, i.e., the LSP mode. These localized and separated oscillation characteristics are similar to those of the well-known LSP resonance discussed in [100].

On the other hand, a fraction of the incident optical radiation can also generate GSP which propagates through the corrugated surface in a form of propagating eigen-mode of the whole corrugated structure. The wavenumber of the GSP can be obtained once the effective permittivity of the grating structure, ε_G, is found by utilizing the Maxwell-Garnet theory, which is shown below [102].

$$\varepsilon_G = \frac{\varepsilon_m[2\varepsilon_m(1-X)+\varepsilon_d(1+2X)]}{[\varepsilon_m(2+X)+\varepsilon_d(1-X)]}, \quad k_{GSP} = k_0\sqrt{\varepsilon_d\varepsilon_G/(\varepsilon_d+\varepsilon_G)} \qquad (3.2.2)$$

where X is the volume fraction of the dielectric with respect to the whole structure.

The LSP and GSP modes interact at the metal-air interface and lead to a maximized, combined SP oscillation when they overlap in phase. Note that the LSP mode is a dominant mode compared to the GSP mode because the LSP mode undergoes significantly less ohmic loss than the GSP mode. This is because the LSP mode is localized and bounded only in the valley of the grating structure. Now, it is able to discuss the diffraction from the SP modes to the outward radiation mode, as depicted in Fig. 3.2.1(b). The wavelength-dependent diffraction is determined by the phase-matching condition among the wavenumbers of the SP modes and the reciprocal lattice vector, which is given by the following equation [78]:

$$k_{SP} \pm mk_G + k_0 \sin\phi = 0 \quad (m=0, 1, 2, \ldots) \qquad (3.2.3)$$

where k_0 denotes the wavenumber of the outward radiation mode in free space, k_G, the reciprocal lattice vector (i.e. $k_G = 2\pi/\Lambda$) of the grating structure having a period of Λ, and ϕ, the angle of the

diffraction in free space. k_{SP} can be given by either k_{LSP} or k_{GSP}. In addition, it is expected that the diffraction angle ϕ will vary with the wavelength of the incident optical radiation once the grating period Λ is fixed, which results in the desired WODB characteristics,

There are 7 adjustable design parameters in the proposed structure: Fiber type, base metal thickness at the valley of the grating, grating period, grating height, total grating length, fiber–facet angle, and grating filling factor, which is the ratio of thin region to the grating period. In terms of the fiber type, the same optical fiber as specified in Section 2 is used. The metal thickness at the valley of the grating is selected to be 20 nm, as determined in the previous section. Grating period is decided to be 380 nm in order to set the range of operation in the target visible range. In terms of the total grating length, 17 periods of the gratings are processed, resulting in the total length of 6.46 μm. This length is long enough to cover the core region even for the case of high fiber–facet angle, e.g., 60° . Other parameters – the grating height, grating filling factor, and the fiber–facet angle – will be optimized in the next section.

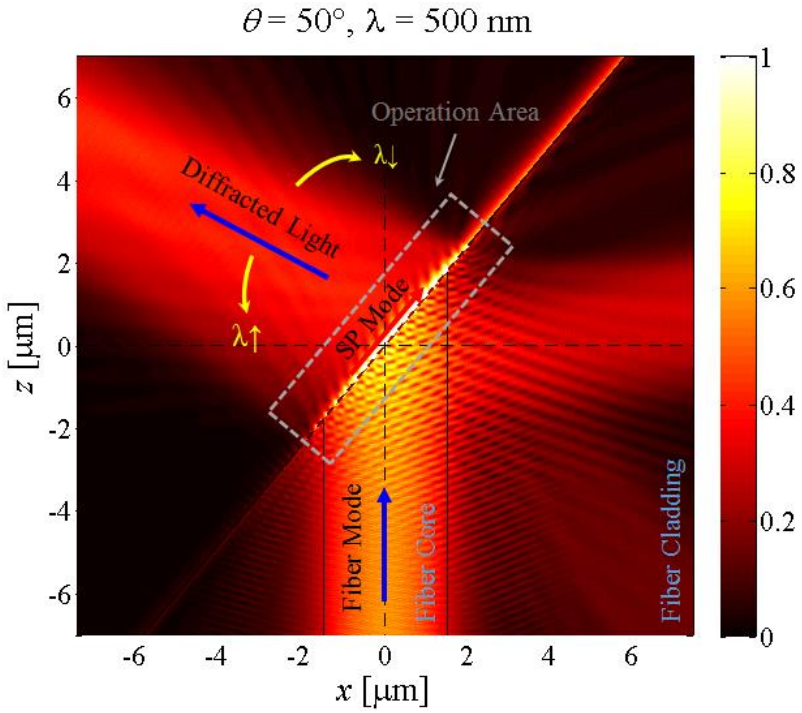

Fig. 3.2.2. Electric-field magnitude pattern of a specific GA-MCAFF scheme.

Fig. 3.2.2 shows how the optical radiation mode is decoupled from the SP modes and evolves in the proposed GA-MCAFF. In order to present a typical case, the grating height, filling factor, fiber-facet angle and the wavelength of the input radiation are set to be 40 nm, 50%, 49° , and 660 nm, respectively. Schematically, the grating structure is stacked upon the 20-nm-thick metal layer that was discussed in Chapter 3.1. In practice, this structure can be realized in a reverse order by coating an angled fiber-facet with 60-nm thickness silver, followed by a 40-nm depth milling process. The fiber mode is incident onto the grating-assisted metal layer from the bottom. Across the grating-assisted metal layer, two steps of mode conversions occur: Firstly, the fiber mode is converted into SP modes

within the metal layer as discussed in Chapter 3.1. Secondly, a fraction of the coupled SP modes is converted into outward-going optical radiation mode from the metal surface via the periodically corrugated grating structure, based on the phase-matching condition given by Eq. (3.2.1). Note that the diffracted light pointing to the top-left corner of Fig. 5 is of interest for the WODB functionality and that the origin of the diffracted light is slightly shifted to the right-top corner of the fiber-facet rather than being at the center of the core. This is because the excited SP modes intrinsically tend to propagate along the metal layer in that direction. According to Eq. (3.2.3), the angle of diffraction, ϕ, will increase in the counterclockwise direction with respect to the wavelength of the incident optical radiation

3.2.2. Numerical Results

In this section, the detailed characteristics of the proposed GA-MCAFF in terms of WODB functionality are discussed. The relationship between the GA-MCAFF and the grating height, grating filling factor, and fiber-facet angle is studied.

Without loss of generality, to justify the WODB functionality, one can consider the figure of merit of this fine-tuning of the fiber-facet angle to be determined either by the diffraction efficacy or the spectral coverage of the proposed GA-MCAFF. For the former, one may define the *overall diffraction efficiency* (ODE), such that the *individual diffraction efficiency* (IDE) is averaged out over the entire spectral range of interest for a given fiber-facet angle, in a similar

way to the definition of the *overall optical-to-SP coupling efficiency* in Chapter 3.1. For the latter, the SB can be defined as the full width at half maximum (FWHM; 3 dB) of the IDE.

First, the grating height is considered. The grating height affects the diffraction efficiency. Low gratings will be indistinguishable in terms of light, and diffraction will barely occur. In the other hand, when the grating is too high, ohmic losses from the long surface will degrade the diffraction efficiency [36]. To optimize the grating height, the same parameters in the previous section are used. The filling factor and the fiber-facet angle are assumed as 50% and 49.5° , respectively.

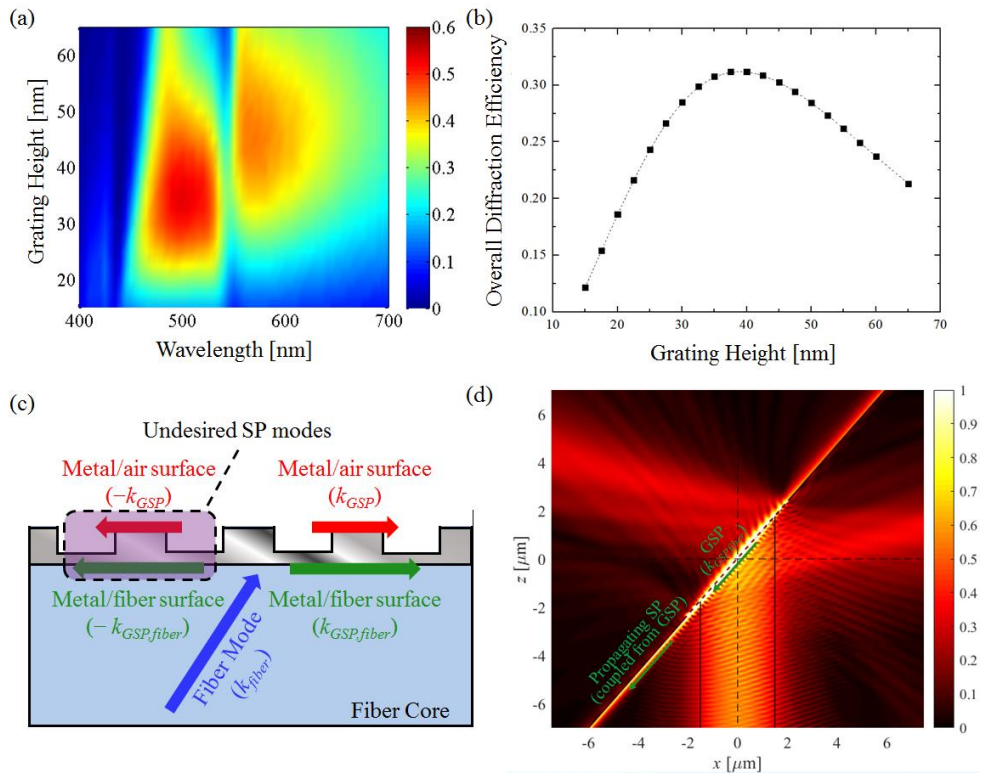

Fig. 3.2.3. (a) IDE spectrum for the various grating heights. (b) ODE and SB in terms of the grating height. (c) Excitation schematic of

undesired SP modes. (d) Electric-field magnitude pattern of singular point.

Fig. 3.2.3(a) shows the IDE spectrum of the different grating heights ranging from 15 nm to 65 nm. The ODE and SB, in terms of the grating height calculated from the previous results, are shown in Fig. 3.2.3(b). 40 nm grating height are selected, which shows highest ODE.

In Fig. 3.2.3(a), one can observe the significant zeros at the wavelengths around 440 nm and 550 nm. Those singular points are caused by the excitation of the different SP modes, such as backward propagating SPs or the SP modes at the metal-fiber interface shown in Fig. 3.2.3(c). Diffraction efficiency decreases when one of these undesired SP mode is excited. The undesired SP modes are generated when the following phase matching conditions are satisfied:

$$k_{fiber}\sin\theta + nk_G = \begin{cases} -k_{GSP} \\ -k_{GSP,\,fiber} \end{cases} \quad (n = \ldots -2, -1, 0, 1, 2, \ldots) \quad (3.2.4)$$

where $k_{\mathrm{GSP,fiber}}$ can be obtained by Eq. (3.2.4). Here, the dielectric is the fiber core. The major zeros appeared at ~550 nm are caused by the generation of SP bounded at the metal/fiber interface, which propagates to the left [denoted by $-k_{GSP,fiber}$ in Fig. 3.2.3(c)]. This phase-matching condition is satisfied when $n = -2$ and the right term is $-k_{GSP,fiber}$. The minor zeros around 440 nm are caused by the backward GSP [denoted by $-k_{GSP}$ in Fig. 3.2.3(c)]. Their phase-matching condition is satisfied when $n = -2$ and the right term is -

k_{GSP}. Note that forward propagating SP bounded in the corrugated metal/fiber surface [denoted by $k_{GSP,fiber}$ in Fig. 3.2.3(c)] does not result in losses. This is because the metal is thin enough for the mode beneath the metal to interact with the SP mode above the metal (i.e. the SP bounded in the corrugated metal/air surface).

The specific field pattern, when the wavelength is 545 nm and the grating height is 40 nm, is shown in Fig. 3.2.3(c), in order to observe the behavior of the singular point.

The grating is the GSP mode at the metal/fiber surface is shown in the figure, which is the electric field tightly focused beneath the grating. Because this GSP mode has similar wavenumber to the SP mode bounded in the plain metal/fiber surface, one can see a portion of the field is coupled onto the SP modes beneath the metal and propagates toward the bottom left side in the figure.

The figure shows that a portion of the field is coupled onto the SP modes beneath the metal and propagates toward the bottom left side in the graph.

Due to the fact that significant zeros are caused by the second order diffraction, the second order effect can be eliminated by adjusting the filling factor. Since the propagation constant at the thick and thin regions are different, 50 % of the filling factor could not remove the second order effect. Now, the filling factor is optimized via numerical simulations by adjusting the filling factor. The grating height and the fiber-facet angle are set as 40 nm and 49.5° , respectively.

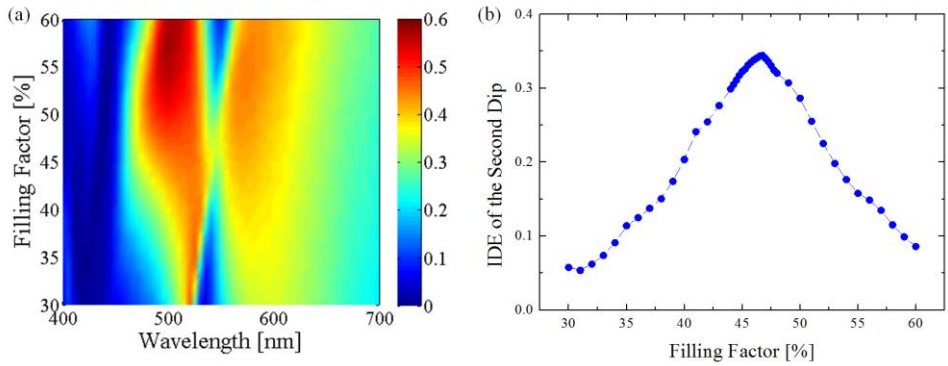

Fig. 3.2.4. (a) IDE spectrum for various filling factors. (b) IDE of the second order dip in terms of filling factor.

Figure 3.2.4(a) shows the IDE spectrum. It can be inferred from the figure that the second order dip has a strong dependency on the filling factor. Fig. 3.2.4(b) shows the IDE at the second order dip in terms of the filling factor. The maximum IDE is obtained when the filling factor is 46.75%. Based on these results, the optimal filling factor is determined to be 46.75 % when the thin region is 177.65 nm and the thick region is 202.35 nm in a period.

Finally the fiber-facet angle is considered. Note that although the previous section presumed that the fiber-facet angle θ is given by ~ 44° , considering the plain surface configuration case, it should be determined more precisely, because the periodically corrugated one-dimensional grating structure is now incorporated in the metal layer so that the corresponding wavenumbers of the excited plasmonic oscillations will significantly be altered from that of the SP modes in the plain surface configuration. In this respect, additional numerical simulations are carried out, tuning the fiber-facet angle and analyzing its consequences. It should be noted that all the other

parameters remain identical to the previous case, except for the fiber–facet angle.

The calculated IDE versus the wavelength of the incident optical radiation, as well as the fiber–facet angle, is presented in Fig. 3.2.5(a). The three curves of the phase–matching angles for θ are presented: A black solid line denotes the trace of θ when $k_{fiber}\sin\theta = k_{GSP}$, a white dashed line denotes the trace of θ when $k_{LSP} = 2\,k_G - k_{GSP\_fiber}$, and a red dash–dot line denotes the trace of $k_{LSP} = 2\,k_G - k_{GSP}$. In fact, k_{LSP} is nearly identical to $k_{fiber}\sin\theta$ [see Eq. (3.2.1)], so the phase–matching condition can be turned into $k_{GSP} = k_{fiber}\sin\theta$. The first curve in a black solid line represents where the IDE is maximized, while the others show the singular zeros. As the design was to eliminate the second order dip at ~ 550 nm, second order dips apart from 550 nm show more significant decrease of IDE.

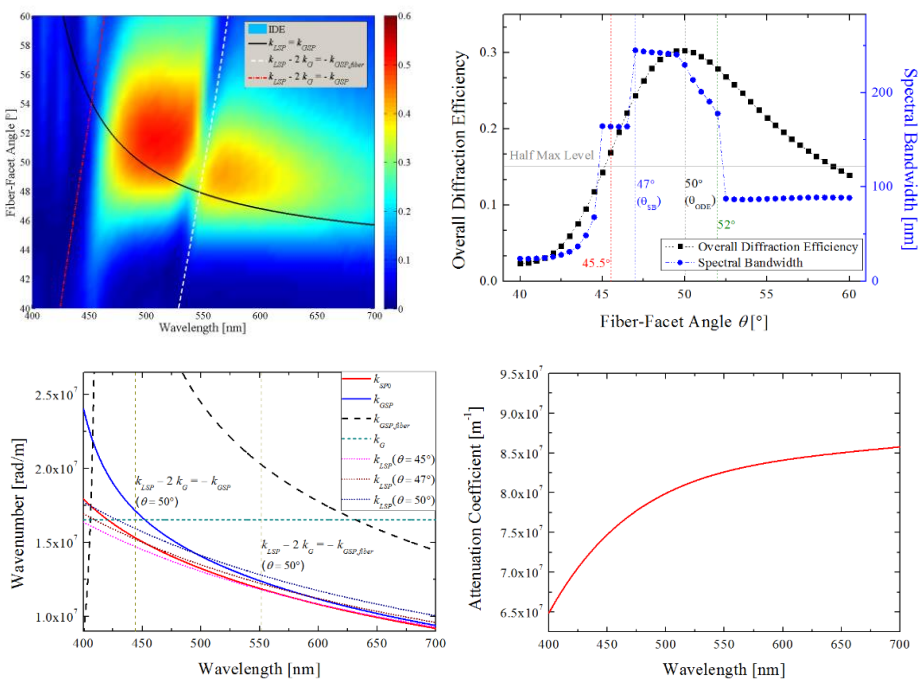

Fig. 3.2.5. (a) Individual diffraction efficiency as a function of wavelength and fiber–facet angle. (b) ODE and SB vs the angle of the fiber–facet. (c) Wavenumber of SP modes and the grating in terms of wavelength. The subplot represents the attenuation coefficient of the metal in terms of wavelength.

From Fig. 3.2.5(a), the ODE and the SB are quantified as shown in Fig. 3.2.5(b). In particular, from Fig. 3.2.5(b) one can see that the ODE peaks at $\theta \approx 50^\circ$ whereas the SB peaks at $\theta \approx 47^\circ$. Steep rise and fall of the SB at ~46.5° and ~ 52° can be observed in Fig. 3.2.5(b). Between these angles, the IDE of the second order dip exceeds the half maximum IDE. The region between these angles can be regarded as a single SB. However in the rest of the region, the second order dip splits the spectrum into two regions, causing significant decrease of SB.

In the grating–incorporated configuration, the ODE peaks at $\theta \approx 50^\circ$ whilst, in the plain–surface configuration, the overall optical–to–SP coupling efficiency peaks at $\theta \approx 45^\circ$. Note that this 5° angle shift is mainly due to the fact that the plasmonic excitation across the grating structure is maximized when both LSP (k_{LSP}) and GSP (k_{GSP}) modes are in phase. In the plain surface configuration, it happens when the optical excitation is in phase only with k_{SP0} [see Eq. 3.1.1].

The significance of such phase–matching conditions for increasing the diffraction or SP coupling efficiency can be well explained in Fig. 3.2.5(c), where the wavenumbers of each SP modes are presented. The blue curve denotes the wavenumber of the GSP mode, and the red curve shows that of the SP mode. Black curve

denotes the wavenumber of the GSP mode bounded in the fiber–metal surface. Three dashed curves represent k_{LSP} mode when the fiber–facet angle is 45°, 47°, and 50°, respectively. The horizontal gray dash line shows the effective wavenumber of the grating. In other words, the incorporation of the periodically corrugated structure in the metal layer leads to a non–negligible change in the phase–matching angle of θ via Eq. (3.2.2). Consequently, the wavenumber of the GA–MCAFF (in the blue line) is significantly shifted towards higher wavenumbers, compared to that of the plain surface MCAFF (in the red line). In fact, the ODE is maximized at $\theta \approx 50^\circ$ with which the exact phase–matching condition (i.e., the intersection of the blue line curve and the dotted line for $\theta \approx 50^\circ$) occurs at the slightly shorter wavelength side rather than at the middle of the whole spectral range of interest. This is due to the fact that the attenuation coefficient of the metal layer is significantly lower at shorter wavelengths as depicted in Fig. 6(c), thereby tending to boost up the ODE significantly if the perfect phase–matching condition occurs there.

In addition, Fig. 3.2.5(c) can also provide an intuitive explanation on how the SB will change with the fiber–facet angle. With the aid of the LSP and GSP phase–matching curves shown in Fig. 3.2.5(c), one can discuss the WODB characteristics of the GA–MCAFF in more detail. For example: (i) for the fiber–facet angle of 47°, the GSP and LSP curves tend to be apart at the most wavelengths, and significantly more apart at the low wavelength region. In fact, they intersect at the high wavelength region, approximately around 600

nm where the ohmic loss of the metal layer is relatively in a moderate level. The given conditions will allow the highest SB. (ii) For the fiber-facet angle of 50° , the two curves cross at the center wavelength region, approximately around 500 nm, where the ohmic loss of the metal layer is relatively low. The distance of them is small at the low wavelength, but gradually increasing in the high wavelength region. Consequently, the given conditions allow the highest ODE, but with a significantly reduced SB, compared to the case (i). In fact, these intuitive explanations via the interplay between the LSP and GSP phase-matching curves are qualitatively in accord with the results discussed in Fig. 3.2.5.

One can also find the phase-matching conditions where the undesired SPs are excited in Fig. 3.2.5(c). Eq. (3.2.4) is satisfied when the k_G line exactly divides in half the k_{LSP} and either the k_{GSP} or k_{GSP_fiber} (i.e. $k_{LSP} + k_{GSP} = 2\ k_G$). For example, for the case of θ = 50° , the distance between k_{GSP} and k_G is the same with that of the k_{LSP} and k_G at ~440 nm, also shown in yellow vertical dashed line.

It is found that the fiber-facet angles of 50° and 47° are the optimal values for the ODE and SB, respectively. For the future reference, they will be defined as θ_{ODE} and θ_{SB}, respectively. In addition, the fiber-facet angles of 45.5 and 52° are taken as a reference group for the further comparison, which are the left and right ends containing half of the ODE and SB.

The far-field intensity distributions of the diffracted beam out of the GA-MCAFF are plotted in Fig. 3.2.6 as a function of the wavelength of the input optical radiation as well as the azimuthal

angle ϕ [see Fig. 3.2.1(b)]. Note that for each figure a virtual line joining the highest field intensity points at the given wavelengths running from the left-mid position to the right-top corner can be regarded as the primary beaming angle of the diffracted light from the end of the GA-MCAFF. This virtual line has a good linearity within the spectral range of interest. In addition, the black-dashed line denotes the diffraction-angle trace calculated by the phase-matching condition between the LSP mode (k_{LSP}), and the free-space mode (k_0) through Eq. (3.2.3). In comparison, the blue dash-dotted line denotes the diffraction-angle trace based on the GSP mode (k_{GSP}) instead of the LSP mode (k_{LSP}). As it has been already explained in the previous section that the LSP mode is the dominant SP mode in the given GA-MCAFF structure, one can see that the virtual line joining the highest field intensity points is, in general, fitted better with the diffraction-angle trace by the LSP mode (i.e., the LSP phase-matching curve) than with the curve by the GSP mode (i.e., the GSP phase-matching curve). In particular, one can see that the IDE tends to increase when the LSP phase-matching curve is close to the GSP phase-matching curve, thereby leading to a low wavenumber difference (i.e., $|k_{LSP} - k_{GSP}|$) between the two SP oscillations. In fact, the distance between the two curves and its change rate are inverse-proportional to the IDE and the SB, respectively.

While the discussion has presumably focused on the impact by the most dominant diffraction when $m = 1$, i.e., the 1st-order diffraction [see Eq. (3.2.3)], one can also observe the effects by the

0^{th}− and 2^{nd}−order diffractions as indicated in Fig. 3.2.6. In principle, their appearances can be significant if the following condition is satisfied:

$$\frac{|\mathrm{Re}(k_{SP}) - mk_G|}{k_0} < 1, \qquad (3.2.5)$$

where m is the order of diffraction, and k_{sp} is given by either k_{LSP} or k_{GSP}. Considering the fact that the plasmonic oscillation in the given configuration is dominated by the LSP mode, one can deduce a couple of significant consequences from Fig. 32.26 and Eq. (3.2.5): The second order diffraction can occur regardless of the fiber−facet angle, but occurs only for short wavelengths. Given the fact that $\mathrm{Re}(k_{SP})$ is close to k_0, second order diffraction cannot occur significantly unless $k_G < k_0$, i.e., the wavelength of the incident optical radiation (λ) is shorter than the period of the grating (Λ) that is 380 nm in the given condition. In contrast, the zeroth order diffraction can occur in the even wider wavelength range, but occurs significantly only when the fiber−facet angle is no greater than ~ 45° . Combining Eqs. (3.2.1) and (3.2.5) for $m = 0$ leads to the fact that the zeroth order diffraction occurs only when $n_{eff} \sin\theta < 1$, which is approximately equivalent to an angular condition of $\theta < 45°$ for $n_{eff} \sim 1.414$ (for LP_{01} mode). Since any diffraction component other than the first order one is undesirable, one should consider increasing the fiber−facet angle well over 45° , thereby sufficiently diminishing the zeroth order diffraction component.

The second order dips can be observed in Fig. 3.2.6. The black curve and the white curve represent the generating condition of the

backward GSP [denoted by $-k_{GSP,fiber}$ in Fig. 3.2.3(c)] and backward GSP beneath the metal [denoted by $-k_{GSP,fiber}$ in Fig. 3.2.3(c)], respectively. A significant decrease in the beaming intensity, when the beaming curves meet the white or black curve, is shown for each figure.

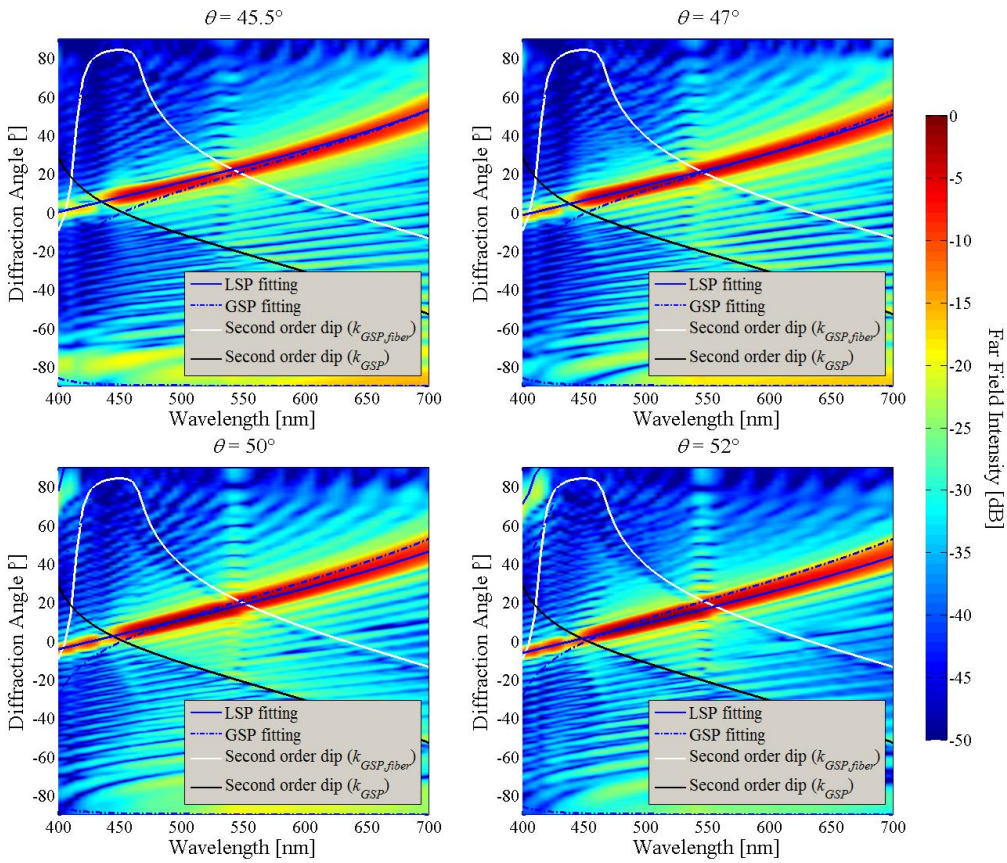

Fig. 3.2.6. Numerical (colormap) and analytical (lines) results of the overall WODB of θ = (a) 45.5° , (b) 47° , (c) 50° and (d) 52° .

To justify the spatial evolution of the diffracted light out of the GA-MCAFF, the field-magnitude patterns are presented in Fig. 3.2.7 for a few typical incident wavelengths (e.g., 450, 550, and 650 nm) and fiber-facet angles (e.g., 45.5° , 47° , 50° and 52°). Note

that the oblique black line in the figure indicates the location of the metal layer of the GA-MCAFF, and the horizontal and vertical dashed lines denote the x and z axes as defined in Fig. 4. All the field-intensity patterns explain by themselves on how the GA-MCAFF functions, depending on the given incident wavelength and the fiber-facet angle, in the ways that has been discussed with Fig. 3.2.6.

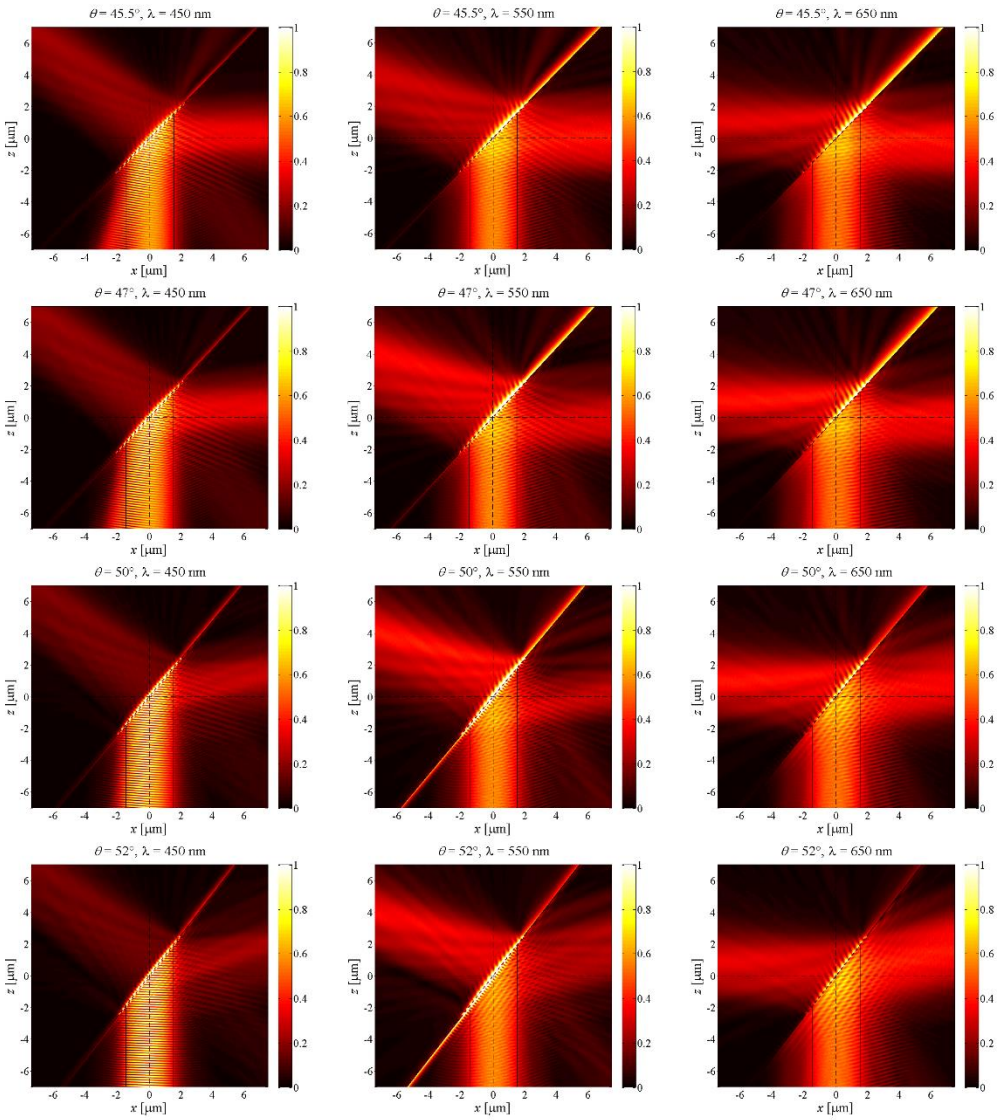

Fig. 3.2.7. Field magnitude patterns when the free space wavelength of the incident light is given by 450 nm, 550 nm and 650 nm for each

fiber–facet angle of θ = (a) 45.5°, (b) 47°, (c) 50° and (d) 52°, respectively.

In particular, comparing the field–intensity patterns in the same horizontal row, i.e., for a fixed fiber–facet angle but with different wavelengths, one can clearly see that the primary beaming angle is substantially varied depending on wavelength, well demonstrating the inherent WODB characteristics. In addition, comparing the field–intensity patterns in the same vertical column, i.e., for a fixed wavelength but with different fiber–facet angles, one can find that the angle of diffraction against the fiber axis (i.e., the z axis), which is given by $\phi_F = \theta + \phi$ [see Fig. 3.2.1(b)] is well maintained, regardless of the value of the fiber–facet angle θ. For further clarification, varying the fiber–facet angle, ϕ_F's for typical wavelengths from 400 nm to 700 nm are calculated by means of the analytical [via Eq. (3.2.1) and Eq. (3.2.3)] and FEM–based numerical methods, and present them in Fig. 3.2.8. Whilst there exist some discrepancies to a small extent, one can verify that the angle of diffraction against the fiber axis, i.e., ϕ_F, is well maintained, nearly independent of the value of the fiber–facet angle θ. Note that the large mismatch of 45° for 400 nm is caused by the back reflection modes. This is a unique feature of the GA–MCAFF enabled by the LSP excitation.

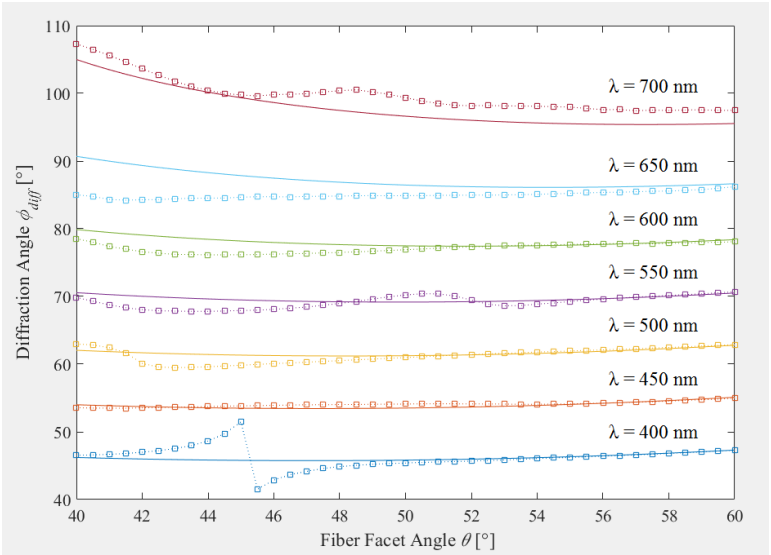

Fig. 3.2.8. Diffracted angle against the fiber axis (ϕ_F) versus fiber-facet angle θ.

Based on the FEM simulations, the ODE, SB, angular width, WODB sensitivity, and primary beaming angle for the four specifically defined fiber-facet angles of 45.5° , 47° , 50° and 52° for three typical wavelengths from 400 nm to 700 nm are calculated. These are summarized in Table 1 together with those for a typical nano-slit-based device having a similar WODB functionality, which is shown in Chapter 2.2, for comparison. Note that the angular width and the WODB sensitivity are defined by the angular spread of the first order diffraction component within a 3-dB intensity range and the rate of the first order diffraction angle change per unit wavelength change, respectively. The summarized characteristics of the GA-MCAFFs of the four different fiber-facet angles represent themselves well why those angles are chosen specifically. In particular, θ = 45° for wide SB operation and θ = 49° for high

ODE operation. The case when θ = 45.5° and θ = 52° exhibits narrowed SB operations and substantially diminished ODE properties.

Table. 3.2.1. Summarized characteristics of GA-MCAFF structures

Fiber-facet Angle θ	*45.5°*	*47°* (θ_{SB})	*50°* (θ_{ODE})	*52°*	*Nano-slit*
ODE [%]	16.93	24.38	30.31	27.91	2.37
SB [nm]	164.2	245	229.2	178	25.03
Angular width [°]	38.69	48.24	45.45	34.59	9.89
WODB sensitivity [° /nm]	0.2356	0.1969	0.1983	0.1943	0.3951
Diffracted angle ϕ_F [°]					
@ λ = 450 nm	53.88	53.99	54.11	54.12	
@ λ = 550 nm	67.97	68.44	70.23	69.46	-
@ λ = 650 nm	84.73	84.78	84.89	84.96	

As pointed out previously, the linearity of the WODB with respect to wavelength is well preserved even when the fiber-facet angle is significantly detuned from the optimal angles, such as θ_{SB} and θ_{ODE}. It is also worth to note that the angle of diffraction against the fiber-facet angle ϕ_F, is well maintained, nearly independent of the choice of the fiber-facet angle. Emphatically, this feature is really encouraging, considering that it will provide a high tolerance from the viewpoint of fabrication of the angled fiber-facet. In addition, the ODE of the proposed GA-MCAFFs are substantially enhanced by an

order of magnitude in comparison with that of a nano-slit-based device having a similar type of WODB functionality whose ODE is limited to ~ 1.8 % at the maximum. This dramatic enhancement is mainly due to the novel implementation of the Kretschmann's configuration into the fiber-facet. Also in terms of SB, the proposed GA-MCAFFs exhibit substantial enhancement in comparison with that of a nano-slit-based device, by more than 2 to 5 times. Note that the characteristic of the proposed GA-MCAFF is comparable to conventional diffraction grating mirrors which shows 70 ~ 80 % of efficiency, and similar spectral bandwidth.

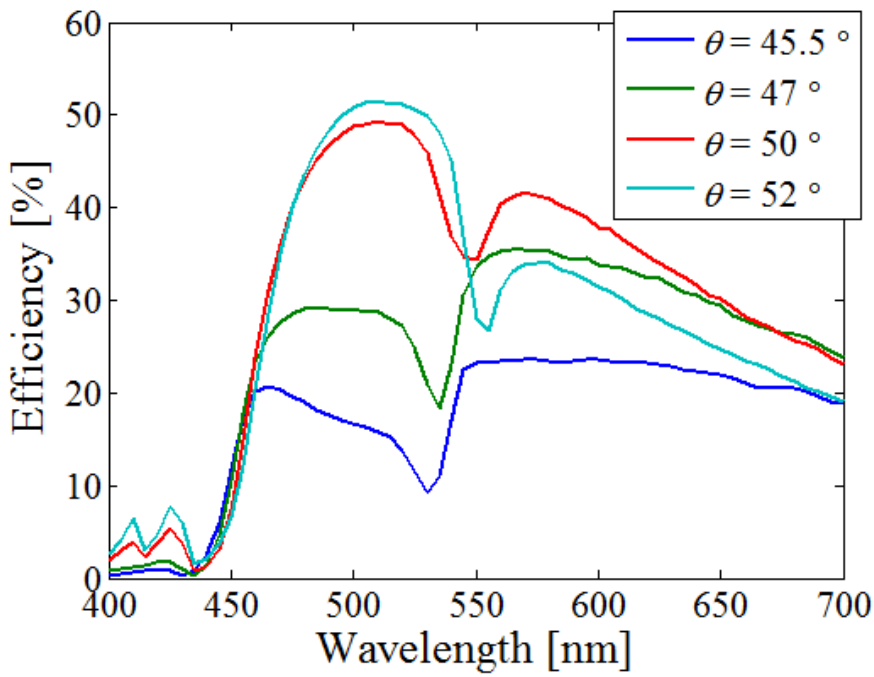

Fig. 3.2.9. Individual diffraction efficiency spectrum for sample facet angles.

3.3 V-shaped surface plasmon transmitter-receiver

Especially, the SP-based sensing technique, such as surface enhanced Raman spectroscopy (SERS), has attracted a lot of research interests for their outstanding capability in terms of sensing [24-27]. However, due to the wavenumber mismatch between the SP mode and the optical mode, generation and reception of SP mode require an additional phase matching process. For example, prisms [26] and corrugated metal tips [25, 27] are widely utilized for conventional SERS sensing. However, prism-based regimes often require elaborate alignment, and it is cumbersome to discriminate the effects by the SP mode from those by the optical mode directly reflected at the prism-metal interface. In the case of corrugated metal tip regimes, the detection is limited to the effects only by localized SP modes, unable to access those by propagating SP modes.

In this chapter, an all-fiberized SP transmitter-receiver is proposed. Whilst the device is based on a similar coupling mechanism to a standard prism-coupling configuration, it requires no alignment procedure because of the all-fiberized configuration. Also, the device is capable of sensing various SP effects induced on the metal layer, so that it can be utilized as a convenient platform for SP-based sensing. The capability of the proposed device are proved via numerical modeling and simulations.

3.3.1 Modeling

The schematic of the proposed device is shown in Fig. 3.3.1. The device is composed on two angle-cleaved fibers, bridged by a thin

metal coating layer. Notwithstanding, the fiber-based scheme allows for alignment-free operation. In terms of the metal thickness, a thinner metal layer exhibits higher coupling efficiency. As a result, on the top of the fiber core, the metal is designed to be sufficiently thin whilst the middle section that bridges the two fibers must be thick enough to prevent the leakage of the SP mode. The transition from the thin layer to the thick layer and vice versa should be done adiabatically to diminish scattering loss. The space above the metal can be filled with any gas or liquid. It is worth noting that this device can now act as a material detector because the SP mode excited on the metal layer can sense the change of the refractive index of the medium above it.

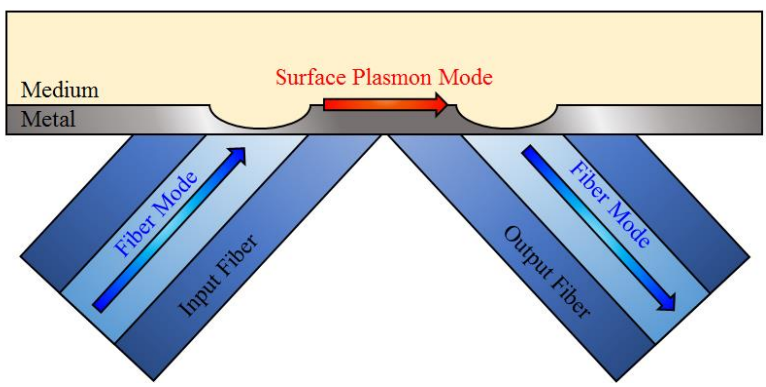

Fig. 3.3.1. Schematic of the SP transmitter-receiver.

3.3.2 Numerical Results

Numerical simulations are performed to verify the performance of the device. The coated metal is set as silver and the thickness of the silver is 50 nm for the thick region and 20 nm for the thin region. The fiber has a 3.5-μm core diameter with a numerical aperture of 0.12,

which follows the characteristics of conventional single-mode fiber [PM 630 HP]. The distance between two fiber centers is set to ~15 μm. The angle between the fiber axis and the metal surface is set by 45 ㅇ.

Figure 3.3.2 shows a typical field pattern when the fiber mode is excited at 740 nm (free-space wavelength) and the upper medium is vacuum. The fiber on the left functions as an input. The incident fiber mode encounters the metal surface and couples into an SP mode. It is worth noting that a fraction of the fiber mode reflects downwards. The coupled SP propagates along the metal surface, and enters the receiver fiber on the right. In fact, the SP mode couples into a fiber mode, propagating towards the right-bottom side of the figure.

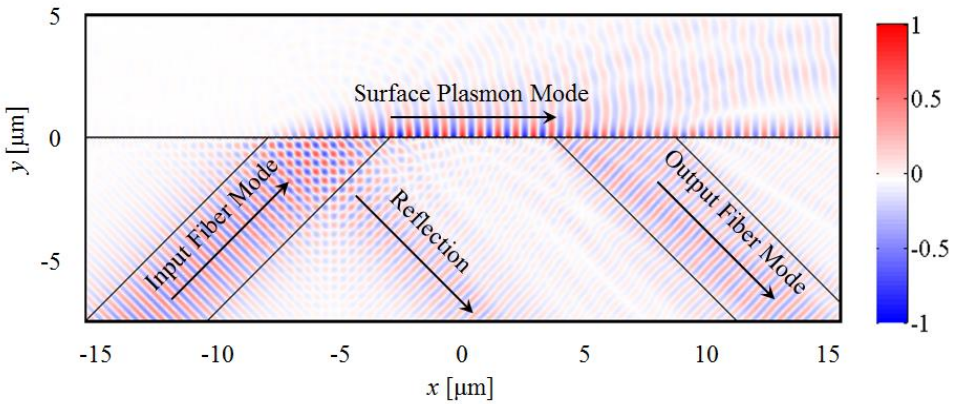

Fig. 3.3.2. Field pattern of the device.

Fig. 3.3.3 shows the coupling efficiency in terms of wavelength for different refractive indices of the top medium, which vary from 1.0 to 1.1. One can observe that coupling efficiency up to ~70 % is available if the medium is set as vacuum. The device also shows >100 nm of 3-dB spectral bandwidth. In fact, the bandwidth becomes

broader if the thickness of the metal layer is thinner [99], which can also be discussed in more detail. Even in the given condition, one can somehow see that the device's coupling efficiency is quite sensitive to the change of the refractive index of the ambient medium in the top layer.

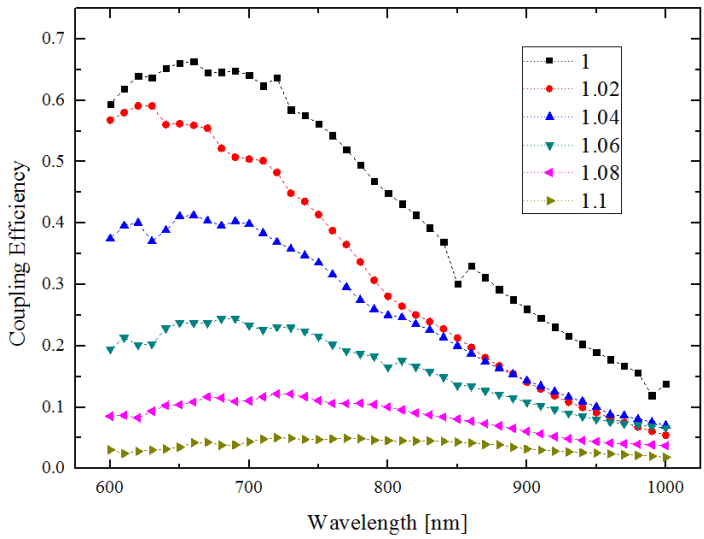

Fig. 3.3.3. Coupling efficiency of the device in terms of wavelength with various media index.

Chapter 4

Conclusion

Throughout this dissertation, the focus is on proposing and demonstrating the metal coated fiber-facet structures. These fiber-optic-plasmonic hybridized schemes achieved various novel effects caused by SP in a reliable and compact fiber-optics-based platform. In Chapter 2, metallic nano-slit based structures were discussed, and a novel angled fiber-facet coupling method was introduced in Chapter 3.

In the first part of Chapter 2, trench-assisted CMNS schemes that can efficiently generate a low-noise CSP hotspot on a fiber end were proposed. The nearby trenches are designed based on the multi-pole cancellation method so that a converging CSP signal is well separated from co-propagating NCDL at the hotspot location. In fact, the secondary radiation by the quasi-pole oscillation from the edge of the trench cancels the primary NCDL, thereby drastically enhancing the SNR of the CSP hotspot. Two types of trench-assisted CMNSs were proposed and investigated: an RT-CMNS for the sake of its simplicity in fabrication and an APT-CMNS for the sake of further promoting the multi-pole cancellation effect. The plasmonic and optical characteristics of these CMNSs are verified through full-

vectorial numerical analyses. The optimized RT-CMNS and APT-CMNS could generate low-noise plasmonic hotspots with substantially high performance characteristics. This chapter stresses that in the case of the APT-CMNS, the multi-pole cancellation effect was maximized to yield an order of magnitude enhancement both in the peak and mean SNRs of the generated plasmonic hotspot in comparison with the conventional CMNS, which lack trenches. Furthermore, the enhancement levels would still be maintained even for a depth tolerance range up to 5 nm, which is the typical depth resolution of the FIB process.

The second and the third parts discuss wavelength-dependent characteristics via nano-slit structures. In Chapter 2.2, a fiber-optical-plasmonic hybrid MCF-GANS structure for WODB in a simple and a compact format is proposed and demonstrated. The model was designed with numerical simulations. After showing the properties of the MCF-GANS, the proposed scheme was demonstrated. Due to the high-accuracy FIB process, the fabricated fiber-facet exhibited a good WODB characteristic, as expected from the numerical modeling. From the results, it was proven that the light is diffracted by periodic grating and shows WODB behavior, and one can properly design a MCF-GANS with desired performance. Moreover, unlike other SP devices, the fiber-facet structure provides various readily prepared sources without any collimations.

In addition, Chapter 2.3 introduces FPFZP schemes on a fiber end that can efficiently generate an RPFL on the free space, where the focal length is tunable by controlling the wavelength. The circular

nano-slits confirm radial polarization and provide a relatively large focal length range. The fiber platform has the advantage of readily launching radially polarized light, and also of controlling the wavelength. The focal length shift due to the wavelength of the FPFZP model is analyzed in both the analytic and numerical models. In this FPFZP, the focal point has changed. In addition, the trapping characteristics of the FPFZP were numerically analyzed. From these results, the trapped particle is expected to move. The FPFZP structure is also fabricated and its characteristics are demonstrated.

In Chapter 3, a novel fiber mode to SP mode coupling configuration - angled fiber-facet coupling method - is presented and some applications are also introduced. In the first section of Chapter 3, a novel SP generation method using an angled fiber-facet, which is a modified Kretschmannm' s configuration, is proposed and implemented on a fiber-optic platform. By coating metal over an angled fiber-facet and launching optical fiber modes at the other end of the fiber, the fiber mode is coupled to SP mode at the metal-air surface on the top of the angled facet. The novel coupling configuration enables alignment-free, high efficiency, unidirectional propagation, and small spot SP generation. The structure is verified by means of numerical simulations and experiments. For applications targeting specific spots and broadband ranges, one can choose thin films and use the LSP bounded at the core region; for propagating SP applications, one may select the proper angle and thickness. The scheme is expected to be a new SP generation configuration which can provide higher efficiency and unidirectionality, and is compatible

with fiber-based optical sources.

In the second section of Chapter 3, the idea from Chapter 2.2 is improved using an angled fiber-facet base. The change from a nano-slit to an angled fiber-facet will increase the coupling efficiency by eliminating the anti-propagating SP. The structure incorporates a periodically corrugated metal layer coated on an angled fiber-facet. The proposed structure provides two primary functions: 1) The metal layer coated on the angled fiber-facet couples the optical fiber mode to an SP mode in an all-fiberized format; and 2) the periodically corrugated grating structure on the upper part of the metal layer decouples the SP mode into a free-space optical radiation mode in different directions, depending on the wavelength of the input optical radiation. Therefore, a novel SP-based WODB functionality is realized in a simple, compact, and all-fiberized format.

The last part of Chapter 3 introduces a versatile fiber-based SP transmitter-receiver, which can be utilized for SERS measurement. Numerical simulations have verified that the proposed device is capable of sensing various plasmonic effects induced at the metal-dielectric interface.

To conclude, a structured metal coated fiber-facet scheme will be very useful for various plasmonic and optical applications, thanks to its compactness, flexibility, and cost-effectiveness. In particular, the proposed MCAFF scheme (fiber-to-SP coupling scheme) has great potential to be an excellent, alternative SP generation method that can provide high efficiency, unidirectionality, and full compatibility with fiber-based optical sources. I believe that this

study will broaden the fiber-optic and plasmonic research fields, which are invariably seeking novel opportunities for combining the extraordinary characteristics of plasmonics and the outstanding flexibility of fiber-optics.

Bibliography

1. R. J. Bates, "Optical switching and networking handbook," (2001).
2. V. Alwayn, "Fiber-optic technologies," Optical Network Design and Implementation (Cisco Press, Indianapolis, IN, 2004) (2004).
3. W. Spillman, D. Patriquin, and D. Crowne, "Fiber optic linear displacement sensor based on a variable period diffraction grating," Applied optics **28**, 3550-3553 (1989).
4. G. Agrawal, "Nonlinear Fiber Optics (Academic, San Diego, Calif., 1995); A. Hasegawa and Y. Kodama," Solitons in Optical Communications (1995).
5. R. G. Gould, "The LASER, light amplification by stimulated emission of radiation," in *The Ann Arbor conference on optical pumping, the University of Michigan*, 1959), 128.
6. R. J. Mears, L. Reekie, I. Jauncey, and D. N. Payne, "Low-noise erbium-doped fibre amplifier operating at 1.54 μm," Electronics Letters **23**, 1026-1028 (1987).
7. D. M. Mullsteff, "Fiber optic communication system," (Google Patents, 2011).
8. Y. e. Jeong, J. Sahu, D. Payne, and J. Nilsson, "Ytterbium-doped large-core fiber laser with 1.36 kW continuous-wave output power," Optics Express **12**, 6088-6092 (2004).
9. G. B. Altshuler, A. V. Erofeev, and I. Yaroslavsky, "Fiber laser device for medical/cosmetic procedures," (Google Patents, 2004).
10. A. Ancona, K. Rademaker, J. Limpert, S. Nolte, and A. TŘnnermann, "High speed laser drilling of metals using a high repetition rate, high average power ultrafast fiber CPA system," Optics express **16**, 8958-8968 (2008).
11. S. A. Maier, *Plasmonics: fundamentals and applications* (Springer Science & Business Media, 2007).
12. R. Ritchie, "Plasma losses by fast electrons in thin films," Physical Review **106**, 874 (1957).
13. T. W. Ebbesen, H. J. Lezec, H. Ghaemi, T. Thio, and P. Wolff, "Extraordinary optical transmission through sub-wavelength hole arrays," Nature **391**, 667-669 (1998).
14. B. Lee, I.-M. Lee, S. Kim, D.-H. Oh, and L. Hesselink, "Review on subwavelength confinement of light with plasmonics," Journal of Modern Optics **57**, 1479-1497 (2010).
15. R. F. Oulton, V. J. Sorger, D. Genov, D. Pile, and X. Zhang, "A hybrid plasmonic waveguide for subwavelength confinement and long-range propagation," Nature Photonics **2**, 496-500 (2008).
16. K.-L. Lee, C.-W. Lee, W.-S. Wang, and P.-K. Wei, "Sensitive biosensor array using surface plasmon resonance on metallic nanoslits," Journal of biomedical optics **12**, 044023-044023-044025 (2007).

17. J. Homola, "Present and future of surface plasmon resonance biosensors," Analytical and bioanalytical chemistry **377**, 528-539 (2003).
18. M. Mansuripur, A. Zakharian, A. Lesuffleur, S.-H. Oh, R. Jones, N. Lindquist, H. Im, A. Kobyakov, and J. Moloney, "Plasmonic nano-structures for optical data storage," Optics express **17**, 14001-14014 (2009).
19. K. Catchpole and A. Polman, "Plasmonic solar cells," Optics express **16**, 21793-21800 (2008).
20. M. L. Juan, M. Righini, and R. Quidant, "Plasmon nano-optical tweezers," Nature Photonics **5**, 349-356 (2011).
21. E. Kretschmann, "Die bestimmung optischer konstanten von metallen durch anregung von oberflächenplasmaschwingungen," Zeitschrift für Physik **241**, 313-324 (1971).
22. A. Otto, "Excitation of nonradiative surface plasma waves in silver by the method of frustrated total reflection," Zeitschrift für Physik **216**, 398-410 (1968).
23. G. Kostovski, P. R. Stoddart, and A. Mitchell, "The Optical Fiber Tip: An Inherently Light-Coupled Microscopic Platform for Micro-and Nanotechnologies," Advanced Materials **26**, 3798-3820 (2014).
24. K. I. Mullen and K. T. Carron, "Surface-enhanced Raman spectroscopy with abrasively modified fiber optic probes," Analytical Chemistry **63**, 2196-2199 (1991).
25. C. Viets and W. Hill, "Comparison of fibre-optic SERS sensors with differently prepared tips," Sensors and Actuators B: Chemical **51**, 92-99 (1998).
26. S. A. Meyer, E. C. Le Ru, and P. G. Etchegoin, "Combining surface plasmon resonance (SPR) spectroscopy with surface-enhanced Raman scattering (SERS)," Analytical chemistry **83**, 2337-2344 (2011).
27. G. Kostovski, D. White, A. Mitchell, M. Austin, and P. Stoddart, "Nanoimprinted optical fibres: Biotemplated nanostructures for SERS sensing," Biosensors and Bioelectronics **24**, 1531-1535 (2009).
28. B. Kim, J. Flamma, E. Ten Have, M. Garcia-Parajo, N. Van Hulst, and J. Brugger, "Moulded photoplastic probes for near-field optical applications," Journal of microscopy **202**, 16-21 (2001).
29. G. Genolet, M. Despont, P. Vettiger, U. Staufer, W. Noell, N. de Rooij, T. Cueni, M.-P. Bernal, and F. Marquis-Weible, "Micromachined photoplastic probe for scanning near-field optical microscopy," Review of Scientific Instruments **72**, 3877-3879 (2001).
30. C. Guan, M. Ding, J. Shi, P. Wang, P. Hua, L. Yuan, and G. Brambilla, "Compact all-fiber plasmonic Airy-like beam generator," Optics letters **39**, 1113-1116 (2014).
31. W. Chen, W. Han, D. C. Abeysinghe, R. L. Nelson, and Q. Zhan, "Generating cylindrical vector beams with subwavelength concentric

metallic gratings fabricated on optical fibers," Journal of Optics **13**, 015003 (2010).
32. H. Kim, S.-Y. Lee, S. Lee, B. Lee, and Y. Jeong, "Plasmonic grating-assisted nano-slit implemented in an all-fiberized format for wavelength-dependent beaming," in *Advanced Solid State Lasers*, (Optical Society of America, 2014), AM5A. 7.
33. E. J. R. Vesseur, R. De Waele, H. Lezec, H. Atwater, F. G. De Abajo, and A. Polman, "Surface plasmon polariton modes in a single-crystal Au nanoresonator fabricated using focused-ion-beam milling," Applied Physics Letters **92**, 083110 (2008).
34. B. Tomiyasu, I. Fukuju, H. Komatsubara, M. Owari, and Y. Nihei, "High spatial resolution 3D analysis of materials using gallium focused ion beam secondary ion mass spectrometry (FIB SIMS)," Nuclear Instruments and Methods in Physics Research Section B: Beam Interactions with Materials and Atoms **136**, 1028-1033 (1998).
35. A. G. Notcovich, V. Zhuk, and S. Lipson, "Surface plasmon resonance phase imaging," Applied Physics Letters **76**, 1665 (2000).
36. H. Kim, S. Koo, N. Park, H.-w. Kihm, and D. Kim, "Application of multi-pole cancellation theory for the enhancement of signal to noise ratio of nano-slit-excited Surface Plasmon waves," SPP5 2011 (2011).
37. W. Srituravanich, L. Pan, Y. Wang, C. Sun, D. B. Bogy, and X. Zhang, "Flying plasmonic lens in the near field for high-speed nanolithography," Nature nanotechnology **3**, 733-737 (2008).
38. W. Chen and Q. Zhan, "Direct imaging of surface plasmon excitation with radially polarized beam," in *SPIE BiOS: Biomedical Optics*, (International Society for Optics and Photonics, 2009), 71920A-71920A-71910.
39. S. Kim, J. Jin, Y.-J. Kim, I.-Y. Park, Y. Kim, and S.-W. Kim, "High-harmonic generation by resonant plasmon field enhancement," Nature **453**, 757-760 (2008).
40. K. Moh, X.-C. Yuan, J. Bu, S. Zhu, and B. Z. Gao, "Radial polarization induced surface plasmon virtual probe for two-photon fluorescence microscopy," Optics letters **34**, 971-973 (2009).
41. I. P. Radko, S. I. Bozhevolnyi, A. B. Evlyukhin, and A. Boltasseva, "Surface plasmon polariton beam focusing with parabolic nanoparticle chains," Optics express **15**, 6576-6582 (2007).
42. Z. Liu, J. M. Steele, W. Srituravanich, Y. Pikus, C. Sun, and X. Zhang, "Focusing surface plasmons with a plasmonic lens," Nano letters **5**, 1726-1729 (2005).
43. H. Kim and B. Lee, "Diffractive slit patterns for focusing surface plasmon polaritons," Optics express **16**, 8969-8980 (2008).
44. J. M. Steele, Z. Liu, Y. Wang, and X. Zhang, "Resonant and non-resonant generation and focusing of surface plasmons with circular gratings," Optics Express **14**, 5664-5670 (2006).

45. W. Chen, D. C. Abeysinghe, R. L. Nelson, and Q. Zhan, "Plasmonic lens made of multiple concentric metallic rings under radially polarized illumination," Nano letters **9**, 4320-4325 (2009).
46. G. M. Lerman, A. Yanai, and U. Levy, "Demonstration of nanofocusing by the use of plasmonic lens illuminated with radially polarized light," Nano letters **9**, 2139-2143 (2009).
47. A. Kinkhabwala, Z. Yu, S. Fan, Y. Avlasevich, K. Müllen, and W. Moerner, "Large single-molecule fluorescence enhancements produced by a bowtie nanoantenna," Nature Photonics **3**, 654-657 (2009).
48. C. Ropers, C. Neacsu, T. Elsaesser, M. Albrecht, M. Raschke, and C. Lienau, "Grating-coupling of surface plasmons onto metallic tips: a nanoconfined light source," Nano letters **7**, 2784-2788 (2007).
49. J. S. Lee, S. Han, J. Shirdel, S. Koo, D. Sadiq, C. Lienau, and N. Park, "Superfocusing of electric or magnetic fields using conical metal tips: effect of mode symmetry on the plasmon excitation method," Optics express **19**, 12342-12347 (2011).
50. H. Kihm, J. Kang, J. Kyoung, K. Lee, M. Seo, and K. Ahn, "Separation of surface plasmon polariton from nonconfined cylindrical wave launched from single slits," Applied Physics Letters **94**, 141102 (2009).
51. Y. Xi, Y. S. Jung, and H. K. Kim, "Interaction of light with a metal wedge: the role of diffraction in shaping energy flow," Optics express **18**, 2588-2600 (2010).
52. G. Gay, O. Alloschery, B. V. De Lesegno, C. O' dwyer, J. Weiner, and H. Lezec, "The optical response of nanostructured surfaces and the composite diffracted evanescent wave model," Nature Physics **2**, 262-267 (2006).
53. X. Yang, H. Liu, and P. Lalanne, "Cross conversion between surface plasmon polaritons and quasicylindrical waves," Physical review letters **102**, 153903 (2009).
54. J. R. Lakowicz, J. Malicka, I. Gryczynski, and Z. Gryczynski, "Directional surface plasmon-coupled emission: a new method for high sensitivity detection," Biochemical and biophysical research communications **307**, 435-439 (2003).
55. S. G. Johnson, S. Fan, A. Mekis, and J. Joannopoulos, "Multipole-cancellation mechanism for high-Q cavities in the absence of a complete photonic band gap," Applied Physics Letters **78**, 3388-3390 (2001).
56. J. S. Liu, J. S. White, S. Fan, and M. L. Brongersma, "Side-coupled cavity model for surface plasmon-polariton transmission across a groove," Optics express **17**, 17837-17848 (2009).
57. M. Kuttge, F. J. G. de Abajo, and A. Polman, "How grooves reflect and confine surface plasmon polaritons," Optics express **17**, 10385-10392 (2009).
58. H. Kim, Y. Kwon, L. A. Vazquez-Zuniga, and Y. Jeong, "Rigorous analysis on a U-shaped index fiber for generating cylindrical vector

beams in an all-fiber format," in *Opto-Electronics and Communications Conference (OECC), 2012 17th*, (IEEE, 2012), 393-394.

59. A. D. Rakić, A. B. Djurišić, J. M. Elazar, and M. L. Majewski, "Optical properties of metallic films for vertical-cavity optoelectronic devices," Applied optics **37**, 5271-5283 (1998).
60. H. Lan and Y. Ding, "Nanoimprint lithography," Lithography, Michael Wang (ED.) (2010).
61. D. P. Ceperley, *Simulation framework for electromagnetic effects in plasmonics, filter apertures, wafer scattering, grating mirrors, and nano-crystals* (University of California, Berkeley, 2008).
62. B. Ung and Y. Sheng, "Interference of surface waves in a metallic nanoslit," Optics Express **15**, 1182-1190 (2007).
63. B. Ung and Y. Sheng, "Optical surface waves over metallo-dielectric nanostructures: Sommerfeld integrals revisited," Optics express **16**, 9073-9086 (2008).
64. L. Cai, G. Li, Z. Wang, and A. Xu, "Interference and horizontal Fabry-Perot resonance on extraordinary transmission through a metallic nanoslit surrounded by grooves," Optics letters **35**, 127-129 (2010).
65. B. Bai, X. Meng, J. Laukkanen, T. Sfez, L. Yu, W. Nakagawa, H. P. Herzig, L. Li, and J. Turunen, "Asymmetrical excitation of surface plasmon polaritons on blazed gratings at normal incidence," Physical Review B **80**, 035407 (2009).
66. F. Kneubühl, "Diffraction grating spectroscopy," Applied optics **8**, 505-519 (1969).
67. A. M. Weiner, "Femtosecond pulse shaping using spatial light modulators," Review of scientific instruments **71**, 1929-1960 (2000).
68. E. Kelleher, J. Travers, E. Ippen, Z. Sun, A. Ferrari, S. Popov, and J. Taylor, "Generation and direct measurement of giant chirp in a passively mode-locked laser," Optics letters **34**, 3526-3528 (2009).
69. K. Goda, A. Mahjoubfar, C. Wang, A. Fard, J. Adam, D. R. Gossett, A. Ayazi, E. Sollier, O. Malik, and E. Chen, "Hybrid dispersion laser scanner," Scientific reports **2**(2012).
70. W.-H. Yeh, J. Kleingartner, and A. C. Hillier, "Wavelength tunable surface plasmon resonance-enhanced optical transmission through a chirped diffraction grating," Analytical chemistry **82**, 4988-4993 (2010).
71. J. He, E. S. Koteles, B. Lamontagne, L. Erickson, A. Delage, and M. Davies, "Integrated polarization compensator for WDM waveguide demultiplexers," Photonics Technology Letters, IEEE **11**, 224-226 (1999).
72. Y. Lee, K. Hoshino, A. Alù, and X. Zhang, "Tunable directive radiation of surface-plasmon diffraction gratings," Optics express **21**, 2748-2756 (2013).

73. O. E. Martinez, "3000 times grating compressor with positive group velocity dispersion: Application to fiber compensation in 1.3−1.6 μm region," Quantum Electronics, IEEE Journal of **23**, 59−64 (1987).
74. F. Röser, J. Rothhard, B. Ortac, A. Liem, O. Schmidt, T. Schreiber, J. Limpert, and A. Tünnermann, "131? W220? fs fiber laser system," Optics letters **30**, 2754−2756 (2005).
75. S.−H. Yun, C. Boudoux, G. J. Tearney, and B. E. Bouma, "High−speed wavelength−swept semiconductor laser with a polygon−scanner−based wavelength filter," Optics letters **28**, 1981−1983 (2003).
76. J. Chow, G. Town, B. Eggleton, M. Ibsen, K. Sugden, and I. Bennion, "Multiwavelength generation in an erbium−doped fiber laser using in−fiber comb filters," Photonics Technology Letters, IEEE **8**, 60−62 (1996).
77. A. Ghatak and K. Thyagarajan, *An introduction to fiber optics* (Cambridge university press, 1998).
78. L.−B. Yu, D.−Z. Lin, Y.−C. Chen, Y.−C. Chang, K.−T. Huang, J.−W. Liaw, J.−T. Yeh, J.−M. Liu, C.−S. Yeh, and C.−K. Lee, "Physical origin of directional beaming emitted from a subwavelength slit," Physical Review B **71**, 041405 (2005).
79. S. Kim, H. Kim, Y. Lim, and B. Lee, "Off−axis directional beaming of optical field diffracted by a single subwavelength metal slit with asymmetric dielectric surface gratings," Applied physics letters **90**, 051113 (2007).
80. S. Feng, X. Zhang, H. Wang, M. Xin, and Z. Lu, "Fiber coupled waveguide grating structures," Applied Physics Letters **96**, 133101 (2010).
81. H. J. Lezec, A. Degiron, E. Devaux, R. Linke, L. Martin−Moreno, F. Garcia−Vidal, and T. Ebbesen, "Beaming light from a subwavelength aperture," Science **297**, 820−822 (2002).
82. P. B. Johnson and R.−W. Christy, "Optical constants of the noble metals," Physical review B **6**, 4370 (1972).
83. S. Quabis, R. Dorn, M. Eberler, O. Glöckl, and G. Leuchs, "Focusing light to a tighter spot," Optics Communications **179**, 1−7 (2000).
84. R. Dorn, S. Quabis, and G. Leuchs, "Sharper focus for a radially polarized light beam," Physical review letters **91**, 233901 (2003).
85. K. S. Youngworth and T. G. Brown, "Focusing of high numerical aperture cylindrical−vector beams," Optics Express **7**, 77−87 (2000).
86. K. Venkatakrishnan and B. Tan, "Interconnect microvia drilling with a radially polarized laser beam," Journal of Micromechanics and Microengineering **16**, 2603 (2006).
87. Q. Zhan, "Trapping metallic Rayleigh particles with radial polarization: reply to comment," Optics express **20**, 6058−6059 (2012).
88. K. C. Neuman and S. M. Block, "Optical trapping," Review of scientific instruments **75**, 2787−2809 (2004).

89. H. Kim, Y. Kwon, L. A. Vazquez-Zuniga, S. J. Lee, W. Park, Y. Ham, S. Song, J.-H. Yang, and Y. Jeong, "Rigorous Analysis on Ring-Doped-Core Fibers for Generating Cylindrical Vector Beams," Journal of the Optical Society of Korea **18**, 650-656 (2014).
90. P. Wróbel, J. Pniewski, T. J. Antosiewicz, and T. Szoplik, "Focusing radially polarized light by a concentrically corrugated silver film without a hole," Physical review letters **102**, 183902 (2009).
91. Y. Fu, W. Zhou, L. Lim, C. Du, and X. Luo, "Plasmonic microzone plate: Superfocusing at visible regime," Applied Physics Letters **91**, 061124 (2007).
92. E.-W. Wang, L.-L. Li, W.-X. Yu, T.-S. Wang, J.-S. Gao, Y.-Q. Fu, and Y.-L. Liu, "The focusing property of immersed plasmonic nanolenses under radially polarized illumination," Photonics Journal, IEEE **5**, 4500207-4500207 (2013).
93. P. Venugopalan, Q. Zhang, X. Li, L. Kuipers, and M. Gu, "Focusing dual-wavelength surface plasmons to the same focal plane by a far-field plasmonic lens," Optics letters **39**, 5744-5747 (2014).
94. W. Wan, C. Ma, and Z. Liu, "Control the dispersive properties of compound plasmonic lenses," Optics Communications **291**, 390-394 (2013).
95. T. Wulle and S. Herminghaus, "Nonlinear optics of Bessel beams," Physical review letters **70**, 1401 (1993).
96. I. Malitson, "Interspecimen Comparison of the Refractive Index of Fused Silica*,†," JOSA **55**, 1205-1209 (1965).
97. A. Rohrbach and E. H. Stelzer, "Trapping forces, force constants, and potential depths for dielectric spheres in the presence of spherical aberrations," Applied optics **41**, 2494-2507 (2002).
98. B. Wang and G. P. Wang, "Plasmon Bragg reflectors and nanocavities on flat metallic surfaces," Applied Physics Letters **87**, 013107 (2005).
99. J. J. Foley IV, H. Harutyunyan, D. Rosenmann, R. Divan, G. P. Wiederrecht, and S. K. Gray, "When are surface plasmon polaritons excited in the Kretschmann-Raether configuration?," Scientific reports **5**(2015).
100. E. Hutter and J. H. Fendler, "Exploitation of localized surface plasmon resonance," Advanced Materials **16**, 1685-1706 (2004).
101. P. Worthing and W. L. Barnes, "Efficient coupling of surface plasmon polaritons to radiation using a bi-grating," Applied Physics Letters **79**, 3035-3037 (2001).
102. T. C. Choy, *Effective medium theory: principles and applications* (Oxford University Press, 2015).

한글 초록

본 논문은 표면 플라즈몬 (surface plasmon, SP) 기반의 금속 코팅된 독창적인 광섬유 단면 구조들을 다룬다. 이 광섬유-플라즈모닉이 결합된 구조는 신뢰성이 높으며 소형화된 광섬유 기반 플랫폼에서 SP의 독특한 효과들을 보였다.

논문의 첫 부분에서는 금속 나노슬릿에 기반한 광섬유 단면 구조들을 제안하였다. 이를 위하여 먼저 저잡음 원통형 SP (cylindrical SP, CSP) 핫스팟을 발생시키는 광섬유 플랫폼 위에 제작 가능한 독창적 참호가 첨가된 원형 금속 나노슬릿 (trench-assisted circular metal nano-slit, TA-CMNS)을 소개하였다. 원형 슬릿 안팎의 참호들은 다중극자 상쇄이론에 입각하여 설계되어 CSP 신호가 집속되는 지점에서 함께 전파되는 NCDL을 최소화시킨다. 해당 구조의 플라즈모닉, 광학 특성은 수치해석으로 계산하였다. 최적화된 TA-CMNS는 상대적으로 높은 신호 대 잡음비를 보이며 저잡음 플라즈모닉 핫스팟을 생성하였다.

다음으로 나노슬릿에 기반한 파장-의존 특성 구조를 소개하였다. 본 논문에서는 단순하고 소형화된 구조에서 파장 대비 축외 방향 비밍 (wavelength dependent off-axis directional beaming, WODB)이 가능한 광섬유-플라즈모닉이 결합된 금속 코팅된 격자 첨가 나노슬릿 광섬유 (metal coated fiber with grating-assisted nano-slit, MCF-GANS) 구조를 제안하였다. 소자는 수치해석적으로 설계되었으며, 실제로 제작되어 그 특성이 입증되었다. 추가로, 파장을 변화시킴으로써 초점 거리가 조절 가능한 자유 공간에서 집속된 원편광 빛 (radially polarized focused light, RPFL)을 생성할 수 있는 광섬유화된

플라즈모닉 프레넬 띠판 (fiberized plasmonic Fresnel zone-plate, FPFZP)을 제안하였다. FPFZP의 파장 변환에 따른 초점거리 변화는 수치해석적으로 입증되었으며, 예상한 결과를 보여주었다. 또한, 덫치기 (trapping) 특성 역시 수치해석적으로 계산되었다. 이 FPFZP 구조를 실제로 제작, 그 특성을 측정하였고, 실험적 결과들은 수치해석 결과들과 일치하였다.

논문의 두 번째 부분에서는 광섬유 모드에서 SP 모드로의 커플링이 가능한 독창적인 구조 - 경사진 광섬유 단면 커플링 방식 - 를 제안하고 그 구조의 적용들도 함께 보였다. 이 특별한 커플링 구조는 조정이 필요 없으며, 효율이 높고, 단방향으로 SP를 진행시키며 작은 점에서 SP를 야기시킬 수 있다. 금속 코팅된 경사진 광섬유 단면 커플링 (metal coated angled fiber-facet, MCAFF) 구조는 수치해석과 실험으로 입증되었다.

마지막으로 MCAFF를 기반으로 한 두 가지 응용방법을 소개하였다. 하나는 MCF-GANS의 향상된 형태로, 기존의 나노슬릿 기반을 MCAFF 기반으로 변경한 구조이다. 이 SP 생성 기반 변경으로 반대 방향으로 진행하는 SP를 제거하여 커플링 효율을 높일 수 있다. MCAFF 상부에 격자를 위치함으로써 SP를 자유 공간 빛으로 파장에 따라 다른 방향으로 전파하게 만든다. 이를 통해 전광섬유화된 구조에서 간략하고 소형화된 WODB를 이룩하였다. 두 번째 응용 구조는 다용도의 광섬유 기반 SP 송수신기이다. 이 구조는 한 쌍의 MCAFF로 이루어져 있다. 수치해석으로 이 구조의 금속-유전체 사이의 플라즈모닉 센싱 능력을 입증하였다.

금속 코팅된 광섬유 단면 구조는 다양한 플라즈모닉 응용분야에 유용할 것이며, 광섬유의 특성에 의해 소형화, 유연성, 경제성 등의 장점을 지닐 것이다. 특히 MCAFF 구조는 고효율성, 단방향성, 그리고

광섬유 광원간의 호응 등의 장점으로 인해 뛰어난 SP 생성의 대안책이 될 잠재력이 있다. 본 논문은 광섬유의 탁월한 유연성과 플라즈모닉스의 독특한 물리 현상을 융합하여, 광섬유 광학과 플라즈모닉스의 연구 지평을 넓힐 것으로 기대된다.